Strain-related phenomena in (In,Ga)N/GaN nanowires and rods investigated by nanofocus x-ray diffraction and the finite element method

Dissertation
zur Erlangung des akademischen Grades

doctor rerum naturalium

(Dr. rer. nat.)

im Fach: Physik

Spezialisierung: Experimentalphysik

eingereicht an der

Mathematisch-Naturwissenschaftlichen Fakultät

der Humboldt-Universität zu Berlin

von

M.Sc. Thilo Johannes Henkel geb. Krause

Präsidentin der Humboldt-Universität zu Berlin

Prof. Dr.-Ing. Dr. Sabine Kunst

Dekan der Mathematisch-Naturwissenschaftlichen Fakultät

Prof. Dr. Elmar Kulke

Gutachter/innen:
1. Prof. Dr. Henning Riechert
2. PD Dr. Martin Schmidbauer
3. Prof. Dr. Thomas Schröder

Tag der mündlichen Prüfung: 06.11.2017

Zusammenfassung

Aufgrund der Fortschritte in der Herstellung von Fokussieroptiken im harten Röntgenbereich, sind an modernen Synchrotronanlagen heutzutage Strahldurchmesser von 100 nm verfügbar. Diese Entwicklung fällt mit dem Bedarf an geeigneten experimentellen Techniken zur Charakterisierung von zunehmend kleineren Halbleiter-Heterostrukturen zusammen. In dieser Arbeit wird das lokal aufgelöste Deformationsfeld einzelner (In,Ga)N/GaN Drähte mit Hilfe nanofokussierter Röntgenbeugung und der Methode der Finiten Elemente untersucht. Hiermit soll ein Beitrag zum grundlegenden Verständis der optischen Eigenschaften geleistet werden, die durch das Deformationsfeld maßgeblich beeinflusst werden.

Zunächst wird die Abhängigkeit der vertikalen Normalkomponente, ε_{zz}, des elastischen Dehnungstensors von der Geometrie eines axialen (In,Ga)N/GaN Nanodrahtes diskutiert. Dabei wird ein signifikant negativer ε_{zz}-Wert beobachtet, sobald das Verhältnis von Nanodrahtradius und (In,Ga)N-Segmentlänge gegen eins strebt. Dieses Phänomen widerspricht dem Deformationsverhalten einer äquivalenten planaren Materialsequenz und zeigt, dass dieses in Nanodrähten weitaus komplexer ist. Auffallend große Scherkomponenten und eine konvexe Verformung der äußeren Oberfläche begleiten das Auftreten des negativen ε_{zz}-Wertes und sind die Ursache dieses Effekts.

Bei (In,Ga)N/GaN-Halbleitern wird ein makroskopisches elektrisches Potential gemessen, welches auch durch den Deformationszustand beeinflusst wird. Basierend auf den neu gewonnenen Erkenntnissen über das Deformationsverhalten wird deshalb untersucht, ob es durch das Design des Deformationsfeldes möglich ist, das elektrische Potential zu minimieren. Dabei wird in der Tat eine Minimierung und somit eine Abweichung von der zu erwartenden linearen Zunahme des elektrischen Potentials mit der Schichtdicke beobachtet. Diese Abweichung führt zu der wichtigen Konsequenz, dass das Spektrum der potentiell emittierten Wellenlängen in einem Nanodraht deutlich eingeschränkt ist.

Durch eine Ummantelung von GaN-Nanodrähten mit einer (In,Ga)N-Schale lässt sich die aktive Fläche und somit die potentielle Lichtausbeute pro Fläche im Vergleich zu planaren Strukturen deutlich erhöhen. Es wurde jedoch festgestellt, dass das entlang der Drahthöhe emittierte Licht rotverschoben ist. Um den Ursprung dieses Phänomens zu beleuchten, wird das lokale Deformationsfeld mit Hilfe nanofokussierter Röntgenbeugung vermessen. Durch die gute räumliche Auflösung ist es möglich, das Deformationsfeld innerhalb einzelner Seitenfacetten zu untersuchen, wobei ein deutlicher Gradient festgestellt wird. Basierend auf dem mit der Methode der Finiten Elemente simulierten Deformationsfeld und kinematischen Streusimulationen, ist es möglich, den Deformationszustand in einen In-Gehalt zu übersetzen. Wenn neben dem Deformationsfeld auch der strukturelle Aufbau in der Simulation berücksichtigt wird, kann der In-Gehalt mit noch größerer Genauigkeit bestimmt werden.

Abstract

Due to recent improvements in the development of focusing optics for hard x-rays, nowadays, spot sizes in the 100 nm regime are available at state-of-the-art synchrotrons. This development coincides with the need of experimental techniques suitable for characterizing the properties of increasingly smaller semiconductor heterostructures such as nanowires. In this thesis, nanofocus x-ray diffraction and the finite element method are applied to analyze the local strain field in (In,Ga)N/GaN nanowires and micro-rods which are discussed as candidates for a plethora of future optoelectronic applications. However, to improve and tailor their properties, a fundamental understanding on the level of individual objects is essential.

In this spirit, the dependence of the vertical normal component, ε_{zz}, of the elastic strain tensor on the geometry of an axial (In,Ga)N/GaN nanowire is systematically analyzed using the finite element method. Hereby, it is found that if the ratio of nanowire radius and (In,Ga)N segment length approaches unity, a significantly negative ε_{zz} value is observed. This stands in stark contrast to naive expectations and shows that the common knowledge about planar systems where ε_{zz} would always be greater or equal zero cannot easily be translated to nanowires with an equivalent material sequence. As the origin of this effect significant shear strains are discussed which go along with a convex deformation of the outer surface resulting in a highly complex strain distribution. Furthermore, it is investigated whether the possibility to tune the ε_{zz} component from tensile to compressive can be used to minimize the inherently strong built-in potentials and, thus, the quantum-confined Stark effect which leads to a poor optical performance of these structures. While for thin segments the electric potential increases linearly, comparable to planar systems, a maximum and a subsequent decrease is observed for larger segments. This gives rise to the important consequence that the range of accessible wavelengths in a nanowire is limited in comparison to an equivalent planar system.

The increased active area of core-shell (In,Ga)N/GaN micro-rods makes them promising candidates for next-generation light emitting diodes. However, it is found that the emission wavelength is significantly red-shifted along the rod height. To shed light on the origin of this phenomenon, nanofocus x-ray diffraction is applied to analyze the local strain field. Due to the high spatial resolution it is possible to investigate the strain field within individual side-facets and to detect a significant gradient along the rod height. Based on the deformation field simulated using the finite element method and subsequent kinematic scattering simulations it is possible to translate the strain state into an In content. This method could be further improved by taking into account the complete structure of the illuminated volume. Apparently, if the thickness of the sub-shells increases significantly the strain state is additionally modified which has to be considered for an accurate determination of the In content.

Scientific contributions

Peer-reviewed publications

A. Davtyan, **T. Krause**, D. Kriegner, A. Al-Hassan, D. Bahrami, S. M. M. Kashani, R. B. Lewis, H. Küpers, A. Tahraoui, L. Geelhaar, M. Hanke, S. J. Leake, O. Loffeld, U. Pietsch
Three-fold rotational symmetry in hexagonally shaped core-shell (In,Ga)As/GaAs nanowires revealed by coherent x-ray diffraction imaging
Journal of Applied Crystallography **50** (2017), to be published

O. Marquardt, **T. Krause**, V. Kaganer, J. Martín-Sánchez, M. Hanke, O. Brandt
Influence of strain relaxation in axial $In_xGa_{1-x}N$/GaN nanowire heterostructures on their electronic properties
Nanotechnology **28** (2017), 215204

T. Krause, M. Hanke, L. Nicolai, Z. Cheng, M. Niehle, A. Trampert, M. Kahnt, G. Falkenberg, C. G. Schroer, J. Hartmann, H. Zhou, H.-H. Wehmann, A. Waag
Structure and Composition of Isolated Core-Shell (In,Ga)N/GaN Rods Based on Nanofocus X-Ray Diffraction and Scanning Transmission Electron Microscopy
Physical Review Applied **7** (2017), 024033

J. M. Wofford, S. Nakhaie, **T. Krause**, X. Liu, M. Ramsteiner, M. Hanke, H. Riechert, J. M. J. Lopes
A hybrid MBE-based growth method for large-area synthesis of stacked hexagonal boron nitride/graphene heterostructures
Scientific Reports **7** (2017), 43644

T. Krause, M. Hanke, Z. Cheng, M. Niehle, A. Trampert, M. Rosenthal, M. Burghammer, J. Ledig, J. Hartmann, H. Zhou, H.-H. Wehmann, A. Waag
Nanofocus x-ray diffraction and cathodoluminescence investigations into individual core-shell (In,Ga)N/GaN rod light emitting diodes
Nanotechnology **27** (2016), 325707

T. Krause, M. Hanke, O. Brandt, A. Trampert
Counterintuitive strain distribution in axial (In,Ga)N/GaN nanowires
Applied Physics Letters **108** (2016), 032103

T. Krause, T. Brandes, M. Esposito, G. Schaller
Thermodynamics of the polaron master equation at finite bias
The Journal of Chemical Physics **142** (2015), 134106

G. Schaller, **T. Krause**, T. Brandes, M. Esposito
Single electron transistor strongly coupled to vibrations: Counting Statistics and Fluctuation Theorem
New Journal of Physics **15** (2013), 033032

T. Krause, G. Schaller, T. Brandes
Incomplete current fluctuation theorems for a four–terminal model
Physical Review B **84** (2011), 195113

Granted beamtime proposals

M. Kahnt, **T. Krause**, M. Hanke, C. Schroer
Complex characterization of individual (In,Ga)N/GaN core-shell rod from light-emitting diodes using 5 methods simultaneously
Beamtime ID: I-20160790, Beamline P06 (PETRAIII), (2017)

T. Krause, M. Hanke
Nanofocus x-ray diffraction on individual axial (In,Ga)N/GaN nanowires
Beamtime ID: HC-2838, Beamline ID13 (ESRF), (2016)

M. Kahnt, **T. Krause**, M. Hanke, C. Schroer
Ptychographic Tomography and X-ray Fluorescence Analysis of Individual (In,Ga)N/GaN Core-Shell Micro-Rod LED Structures
Beamtime ID: I-20160215, Beamline P06 (PETRAIII), (2016)

T. Krause, M. Hanke
Strain and shape analysis on single (In,Ga)N/GaN micro-rods by nanofocused x-ray reflectivity and diffraction
Beamtime ID: I-20150179, Beamline P06 (PETRAIII), (2016)

T. Krause, M. Hanke
Strain and shape analysis on single (In,Ga)N/GaN micro-rods by nanofocused x-ray reflectivity and diffraction
Beamtime ID: HC-2523, Beamline ID13 (ESRF), (2015)

M. Hanke, T. Schumann, **T. Krause**, J. M. Lopes
Van der Waals-bound graphene/h-BN heterostructures as studied by grazing incidence x-ray diffraction
Beamtime ID: HC-2225, Beamline BM25 (ESRF), (2015)

T. Krause, M. Hanke
Local determination of elastic strain tensor components in one-dimensional heteroepitaxial (In,Ga)N/GaN nanowires
Beamtime ID: I-20140305, Beamline P06 (PETRAIII), (2015)

M. Hanke, **T. Krause**, J. M. Lopes
Graphene on Al_2O_3: a surface x-ray diffraction study
Beamtime ID: HC-1966, Beamline ID10B (ESRF), (2015)

T. Krause, M. Hanke
Spatially resolved strain and composition analysis in radial (In,Ga)N/GaN core shell rods by nano x-ray diffraction and fluorescence
Beamtime ID: HC-1949, Beamline ID13 (ESRF), (2014)

T. Krause, M. Hanke
High-resolution x-ray diffraction on single nanowires
Beamtime ID: I-20130284, Beamline P06 (PETRAIII), (2013)

Conference contributions

T. Krause, M. Hanke, H. Küpers, F. Bastiman, L. Geelhaar, A. Trampert
Investigation of core-shell (In,Ga)As/GaAs nanowires by nanofocus x-ray diffraction
The 12th Biennial Conference on High-Resolution X-Ray Diffraction and Imaging (XTOP 2014), Grenoble and Villard-de-Lans, France, (2014)

T. Krause, M. Hanke, H. Küpers, F. Bastiman, L. Geelhaar, A. Trampert
Studies of core-shell nanowires by x-ray diffraction and kinematic scattering simulations
1st European Crystallography School, Pavia, Italy, (2014)

T. Krause, M. Hanke, H. Küpers, F. Bastiman, L. Geelhaar
Studies of core-shell nanowires by kinematic scattering simulations
Spring Meeting of the German Physical Society (DPG-Frühjahrstagung), Dresden, Germany, (2014)

Berlin,

Table of Contents

List of Figures

Abbreviations

2D	two-dimensional
3D	three-dimensional
a. u.	arbitrary units
CL	cathodoluminescence
CRL	compound refractive lens
CTR	crystal truncation rod
DQW	double quantum well
DWBA	distorted wave Born approximation
ESRF	European Synchrotron Radiation Facility
FEM	finite element method
FIB	focused ion beam
FWHM	full width at half maximum
FZP	Fresnel zone plate
GID	grazing incidence diffraction
GISAXS	grazing incidence small angle scattering
HAADF	high-angle annular dark-field
hcp	hexagonal-closed-pack
ID	insertion device
KB	Kirkpatrick-Baez
LED	light emitting diode
MOVPE	metalorganic vapor phase epitaxy
MQW	multi quantum well
NFL	nanofocusing lens
NW	nanowire
PDE	partial differential equation
QD	quantum disk
QW	quantum well
ROI	region of interest
RSM	reciprocal space map
SEM	scanning electron microscopy
STEM	scanning transmission electron microscopy

1 Introduction

Owing to a plethora of potential new applications, low-dimensional semiconductor structures such as quantum dots, nanowires (NWs) or micro-rods gained an increased interest in research over the last years [1–3]. For example, they can function as artificial atoms enabling single photon emission [4–6] which is of interest for quantum computing, cryptography and communication. Their unique properties related to strain relaxation can be exploited for solid state lightening applications [7–13], lasing [14–16] and solar water splitting [17–19]. As a consequence of missing lateral constraints, strain resulting, e. g., from combining lattice-mismatched materials can be relieved elastically such that high crystal quality can be maintained. This triggers to investigate the integration of different material compounds into the well established Si technology [20–24]. Moreover, the fabrication of high performance field-effect transistors [25–29] and solar cells [30–32] has been pursued.

For understanding and improving the functionality of these structures, their fundamental properties related to structure and chemical composition have to be investigated. Amongst others, x-ray diffraction with spot sizes in the sub-mm range is a well established technique capable of providing such information. Its attractiveness arises from a variety of beneficial properties such as a high penetration depth and a non-destructive interaction with the crystal. Additionally, in many cases experiments can be conducted without destructive sample preparation. In the hard x-ray regime, the wavelength of x-rays is in the order of 1 Å or smaller which is the length scale of inter-atomic distances. Thus, hard x-rays are highly suitable to probe lattice deformations from which conclusions about the optoelectronic performance can be drawn.

The real space shape function of an ensemble of low-dimensional objects is given by the convolution of the shape function of an individual object and a sum of δ-functions defining the position of the objects. In reciprocal space which is measured in an x-ray diffraction experiment this relation simplifies to a product and the retrieved information about an ensemble corresponds to the one of a single object times a correlation function. However, this is only true if all constituents within the ensemble are identical in structure and chemical composition. Yet, recent investigations showed this prerequisite often is not the case such that conventional x-ray diffraction becomes inapplicable. Consequently, the necessity for characterization techniques enabling the investigation of individual µm- or even nm-sized objects with high spatial resolution becomes evident.

Due to recent advances in the young research field of high quality focusing optics for hard x-rays, nanofocus x-ray diffraction has proven to be able to fill this gap. At synchrotrons which exceed the brilliance of laboratory x-ray sources by about 12 orders of magnitude [33], nowadays, intense x-ray beams with spot

sizes in the sub-100 nm regime are available at hard x-ray energies and high photon fluxes. This adds the requirement for a high resolution in real space to the inherently high resolution in reciprocal space such that the characterization of individual objects becomes feasible. For example, shape and strain distribution of individual SiGe islands [34, 35], the distribution of crystal phases in GaAs NW ensembles [36] as well as the local strain field, e. g., in individual GaAs [37], core-shell (In,Ga)N/GaN [38, 39] and Ge [40] NWs has been investigated. Moreover, fluctuations in the composition such as elemental segregation within low-dimensional heterostructures have been studied using the example of single (In,Ga)N NWs [41, 42]. The spatial resolution of the highly collimated x-ray beams enables to investigate selected individual objects, e. g., marked by a focused ion beam [43], and to perform complementary measurements on the very same structure. Such experiments have been reported for the correlation of electrical and structural properties within individual GaAs NWs which have been measured in their as-grown environment [44]. Moreover, the mechanical deformation of single SiGe islands has been monitored by in-situ reciprocal space mapping using a focused x-ray beam with a spot size of about 200 nm [45]. The availability of collimated and coherent x-ray beams has also enabled new research fields to develop such as coherent x-ray diffraction imaging [46–54]. This experimental technique offers a route to tackle the phase problem inherent to x-ray diffraction experiments. Based on an oversampling of the recorded diffraction patterns, iterative algorithms are used to obtain the real space image of an object via Fourier transformation.

In order to interpret the experimentally measured strain field, often numerical finite element method (FEM) simulations are employed. The FEM enables a realistic modeling of the shape of the investigated object and a simulation of the inherent three-dimensional deformation field based on linear elasticity theory. From that, related quantities such as the strain distribution and the piezoelectric potential can be deduced. Hereby, the full anisotropy is taken into account. Using the deformation field obtained by the FEM as input, simulations of the diffusely scattered intensity in the vicinity of Bragg reflections can be computed and compared to experimentally measured x-ray diffraction intensity patterns. Thereby, shape and chemical composition of the investigated real space object can be deduced. In fact, the FEM in conjunction with scattering simulations has been successfully applied for the interpretation of x-ray diffraction data recorded at low-dimensional objects. These comprise, e. g., SiGe whiskers [55], single axial In(As,P)/InAs [56, 57] and core-shell (In,Ga)N/GaN NWs [38], (In,Ga)As/GaAs quantum dot molecules [58], SiGe islands [59] and strained Ge micro bridges [60].

The scope of this thesis

The studies presented in this thesis are dedicated to the investigation of (In,Ga)N/GaN NW and micro-rod heterostructures via nanofocus x-ray diffraction and the FEM. In particular, the deformation field and related quantities such as strain and piezoelectric potential in axial and core-shell NW geometries are discussed. In addition to contributing to the understanding of low-dimensional (In,Ga)N/GaN heterostructures, this thesis also addresses more methodological questions related to the applicability and the limits of nanofocus x-ray diffraction in materials science.

Planar GaN-based semiconductor structures are well established in state-of-the-art technologies, especially, in solid state lighting and electronics. For example, they have been used to fabricate the first commercially available blue light emitting diode (LED) by Nichia Corporation [61]. Moreover, in 2014 the Nobel Prize for Physics has been awarded for the success of fabricating efficient blue LEDs. Next to others, the attractiveness of this compound semiconductor arises from the fact that when In is incorporated into a GaN matrix the band gap of the ternary alloy $In_xGa_{1-x}N$ can be tuned through the complete visible spectrum by changing the In content x from 0 to 1. This important property makes the compound highly interesting for red-green-blue LEDs for display technology. However, due to the large lattice mismatch of about 10 % between InN and GaN it has proven to be difficult to produce planar (In,Ga)N/GaN heterostructures with In contents required for emitting red light while retaining a sufficiently high crystal quality. Additionally, strong polarization potentials inherent to (In,Ga)N/GaN heterostructures lead to weak optical performance.

Promising candidates to overcome the discussed obstacles is the fabrication of (In,Ga)N/GaN NWs or micro-rods. Their increased surface-to-volume ratio offers an efficient way of elastic strain relaxation and, thus, the prospect to incorporate a high amount of In into a GaN matrix while maintaining high crystal quality [62]. Actually, it has been shown that in (In,Ga)N NWs the emitted wavelength can be tuned from the near-ultraviolet to the near-infrared region [63, 64]. Another decisive advantage is that due to the 3D geometry, the optically active area per wafer unit can be significantly increased compared to planar structures [12]. However, the fabrication of large ensembles with high homogeneity has shown to be challenging and the performance of planar (In,Ga)N/GaN systems could not yet be reached.

To improve the fabrication process and to actually profit from the discussed beneficial properties of NWs and micro-rods, a characterization on the level of single objects is necessary. This thesis intends to contribute to this developing process by investigating the fundamental properties related to strain-induced deformations of axial NWs and core-shell micro-rods by employing nanofocus x-ray diffraction and the FEM. After having introduced the fundamentals in chapter 2 which are intended to provide enough background information to follow the presented studies, a counterintuitive strain distribution inherent to axial (In,Ga)N/GaN NWs is discussed in chapter 3. The successive chapter 4

builds upon this introduced strain-related phenomenon and deals with the question whether strain engineering can be used to minimize the inherent electric potential and, thereby, to improve the optical performance. While chapters 3 and 4 present purely theoretical studies the following two chapters 5 and 6 are devoted to nanofocus x-ray diffraction experiments performed on core-shell (In,Ga)N/GaN micro-rods. The micro-rods are optimized with respect to their optical performance and show a significant red-shift in the emitted wavelength from bottom to top. To shed light on the origin of this observation, individual micro-rods are extracted using a focused ion beam. This enables to investigate the local strain field as well as the structure of individual micro-rods. The experiments are complemented with cathodoluminescence and scanning transmission electron microscopy measurements performed on micro-rods from the same sample. By employing the FEM and subsequent kinematic scattering simulations the detailed knowledge about the structure of the micro-rods can be used to translate the measured strain field into an In content. Finally, the results are summarized in chapter 7 and an outlook to future research projects is given.

2 Fundamentals

This chapter intends to provide an overview about the fundamentals necessary to follow the scientific results presented in chapters 3 to 6. However, the introduced content is not a complete elaboration of the respective topic and a deeper insight can be found in the cited textbooks on which this chapter is based.

In section 2.1, the investigated material system, (In,Ga)N/GaN compound semiconductors, is introduced. Section 2.2 provides a brief introduction to linear elasticity theory which is based on Refs. [65–69]. GaN comprises a singular polar axis giving rise to the occurrence of an internal electric field. Due to elastic deformation of the unit cell an additional piezoelectric field is induced and an introduction to the mathematical description of this phenomenon is given in section 2.3. A deeper insight about piezoelectricity can be found in Refs. [67, 70] and specifically for GaN in Ref. [71]. Both, the elastic properties as well as the piezoelectric potential can be computed using the finite element method (FEM) and due to the variety of applications, there exist different approaches. The FEM simulations shown in this thesis are based on the displacement method which is introduced in a compact manner in section 2.4. The presented theory can be found in more detail in Ref. [72] and specifically for the used commercial software package MSC.Marc2008r1 in Ref. [73].

The elastic properties of rods are investigated using synchrotron radiation in the hard x-ray regime. The generation of x-rays using a synchrotron as a source and their properties are subject to section 2.5. An important peculiarity of the presented experimental data is that they have been recorded using highly focused x-ray beams providing a spatial resolution of about 100×100 nm^2. Due to the fact that focusing of x-rays is a young and vividly developing research field, the most commonly used focusing optics are introduced in section 2.6. Using a highly collimated x-ray beam, diffraction experiments have been performed on several individual (In,Ga)N/GaN rods. Therefore, an introduction to scattering geometries and x-ray diffraction theory is given in sections 2.7 and 2.8, respectively. Finally, section 2.9 provides insight about scattering simulations performed in the kinematic approximation which are used to interpret the recorded experimental data. Sections 2.5 to 2.9 are based on a variety of textbooks, Refs. [33, 74–76], all covering the wide field of x-ray physics.

2.1 Properties of (In,Ga)N/GaN compound semiconductors

The compounds GaN and InN belong to the group of III-V semiconductors. GaN is a wide band gap semiconductor and is commonly used in a variety of technological applications such as high-performance white and blue light emitting diodes (LEDs) [61], laser diodes and transistors. InN is a small band gap semiconductor emitting in the infrared. It is of particular technological interest as a constituent in ternary and quaternary III-nitride compounds such as (In,Ga)N and (Al,Ga,In)N which are used for blue and ultraviolet LEDs [77–79].

GaN and InN can be grown epitaxially by means of, e. g., molecular beam epitaxy (MBE) or metal-organic vapor phase epitaxy (MOCVD) on a variety of substrates [80–83]. Commonly used are transparent substrates such as $\langle 0001 \rangle$-oriented sapphire (Al_2O_3) and SiC. Here, a challenge is the large lattice mismatch which is about 16 % for GaN and sapphire. To minimize plastic relaxation in the active area, GaN or AlN buffer layers are often grown on top of the substrate. The growth of GaN on [111]-oriented Si substrates is of particular interest as it offers a route to its integration into the highly developed Si technology. GaN can be n-type doped commonly by using Si or O and p-type doped, e. g., with Mg.

In the densest packing of spheres, after the first two layers there exist two possibilities to proceed with the third layer. In the first case the third layer is placed on top of the first layer resulting in an "ABAB" layer sequence. This order of stacking is inherent to the hexagonal-closed-pack (hcp) crystal structure, also called wurtzite. If the third layer is placed in between the spheres of the first layer a sequence "ABCABC" is obtained which is inherent to the $\langle 111 \rangle$-oriented zincblende crystal structure.

III-nitride compounds usually crystallize in the wurtzite lattice structure with a strictly alternating "ABAB" stacking of atomic layers as sketched in Fig. 2.1(a) and belong to the space group $P6_3mc$ (No. 186) which, importantly, has no inversion center. However, under certain growth conditions, GaN and InN can also be grown in zincblende phase [84–86]. Figure 2.1(a) shows a projection of the III-nitride crystal onto the $[\bar{1}\bar{1}20]$-direction with the vertical axis pointing along the polar [0001]-direction. Here, the group-V atom, N, is shown in blue and the group-III atoms Ga and In in orange. The atomic arrangement corresponds to the densest packing of spheres. However, a slight deviation in the bonding length in comparison to an ideal wurtzite crystal exists yielding the important consequence that atomic dipoles are formed. The unit cell of the hcp Bravais lattice is spanned by the vectors a, b and c shown in Fig. 2.1(b). The angle between vectors a and b is 120° and c is directed along the [0001]-direction, normal to the basal plane spanned by a and b. It holds that $|\mathrm{a}| = |\mathrm{b}| = a$ where a is the in-plane lattice constant and $|\mathrm{c}| = c$ is the out-of-plane lattice constant. Thus, the unit cell vectors are given by

$$\mathrm{a} = a\,\hat{\mathrm{e}}_\mathrm{x}\,, \qquad \mathrm{b} = \frac{a}{2}\,\hat{\mathrm{e}}_\mathrm{x} + \frac{\sqrt{3}a}{2}\,\hat{\mathrm{e}}_\mathrm{y} \quad \text{and} \quad \mathrm{c} = c\,\hat{\mathrm{e}}_\mathrm{z}\,, \tag{2.1.1}$$

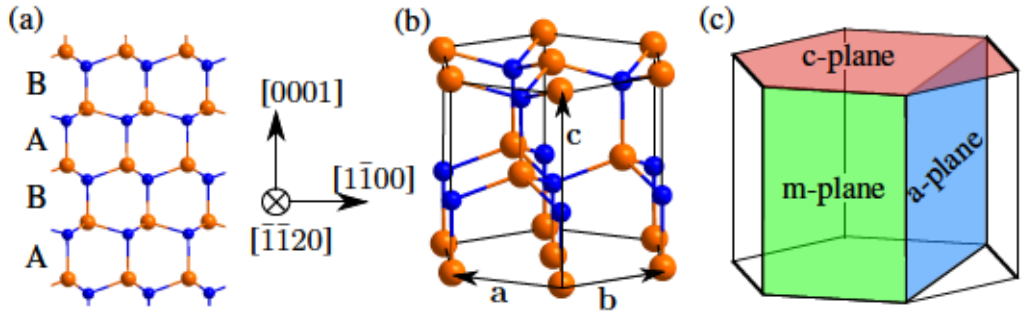

Figure 2.1 The hexagonal III-V crystal structure is shown whereas the group-III atoms are shown in orange and the group-V atoms in blue. In (a) the crystal is projected onto the [$\bar{1}\bar{1}$20]-direction and the vertical axis is the polar [0001]-direction. A characteristic feature of the wurtzite structure is the alternating sequence of layers A and B. The unit cell is spanned by the vectors **a**, **b** and **c** as drawn in (b). The {0001} lattice planes are also called c-planes and the two non-polar directions, [1$\bar{1}$00] and [$\bar{1}\bar{1}$20], point perpendicular from the m- and a-planes, respectively, as sketched in (c).

where $\hat{\mathbf{e}}_x$, $\hat{\mathbf{e}}_y$ and $\hat{\mathbf{e}}_z$ are the orthonormal unit vectors. The crystal lattice is then specified by a set of vectors $\mathbf{r_n}$ with

$$\mathbf{r_n} = n_1\mathbf{a} + n_2\mathbf{b} + n_3\mathbf{c}\,, \quad n_{1,2,3} \in \mathbb{Z}\,. \tag{2.1.2}$$

The basis contains four atoms located at positions (0, 0, 0), (1/3, 2/3, 1/2), (0, 0, 0.37308) and (1/3, 2/3, 0.89231) [87]. The binding character is ionic yielding high thermal and chemical stability. III-nitrides are also hard materials expressed by a low Poisson ratio. Using the Bravais-Miller indexes for the hexagonal crystal, $(hkil)$ with $i = -(h+k)$, the distance d_{hkil} between hexagonal lattice planes can be computed via

$$d_{hkil} = \sqrt{\frac{1}{(h^2 + k^2 + hk)\frac{4}{3a^2} + \frac{l^2}{c^2}}}\,. \tag{2.1.3}$$

The crystallographic directions along $\langle 1\bar{1}00\rangle$ and $\langle \bar{1}\bar{1}20\rangle$ are non-polar and called m-plane and a-plane direction, respectively, as sketched in Fig. 2.1(c). However, the c-direction, which points vertically with respect to the c-plane colored in red in Fig. 2.1(c), is the only polar direction. Crystal directions which are inclined between the two cases are referred to as semi-polar. Along the c-direction, stacked pairs of group-III and group-V atoms induce atomic dipoles. This is a consequence of the higher electronegativity of N atoms compared to Ga and In atoms such that binding electrons are located closer to N atoms. The atomic dipoles add up to a permanent macroscopic polarization called spontaneous or intrinsic polarization.

When In atoms are incorporated into a GaN matrix during epitaxial growth, the ternary alloy (In,Ga)N is formed. The resulting lattice parameter of this alloy lies in between the ones of InN and GaN and is usually interpolated assuming a

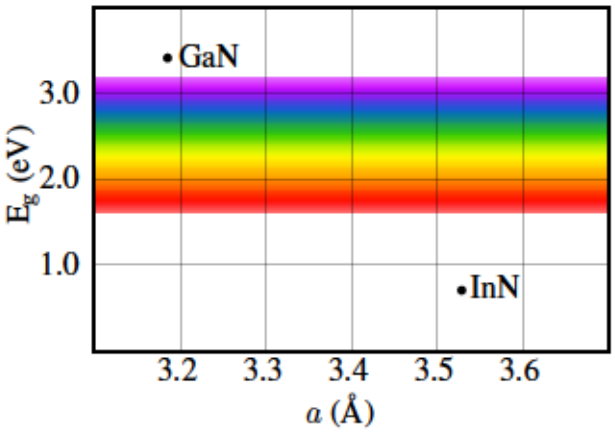

	GaN	InN
a (Å)	3.189	3.533
c (Å)	5.185	5.693
E_g (eV)	3.43	0.64

Figure 2.2 The energy of the direct band gap, E_g, as a function of the in-plane lattice parameter, a, for GaN and InN. The visible spectrum is indicated by the colored background. By changing the In content x in the ternary alloy $In_xGa_{1-x}N$ the emitted wavelength can be tuned through the full optical spectrum. The used values are taken from Ref. [88] and are displayed in the table.

linear relationship known as Vegard's law

$$a(\mathrm{In_xGa_{1-x}N}) = \mathrm{x} \cdot a(\mathrm{InN}) + (1-\mathrm{x}) \cdot a(\mathrm{GaN})\,, \tag{2.1.4}$$

whereas x is the In content. Importantly, the resulting lattice parameter induces an internal strain which modifies the band gap of the alloy. For interpolating the band gap energy E_g the quadratic term is also considered

$$E_g(\mathrm{In_xGa_{1-x}N}) = \mathrm{x} \cdot E_g(\mathrm{InN}) + (1-\mathrm{x})E_g(\mathrm{GaN}) - b \cdot \mathrm{x}(1-\mathrm{x})\,, \tag{2.1.5}$$

where b is called the bowing parameter which is a material specific constant. This is of great technological relevance as the direct band gap of $In_xGa_{1-x}N$ can in principle be tuned from 0.64 to 3.43 eV by varying the In content x from 1 to 0 [63, 64] or by increasing the (In,Ga)N layer thickness [89]. As shown in Fig. 2.2, thereby wavelengths from near-infrared to the ultraviolet are accessible covering the full visible spectrum as sketched by the colored background. Hence, by varying the In content it is possible to tailor the optoelectronic properties very effectively.

An (In,Ga)N layer can be embedded into a GaN matrix to form a heterostructure. If the bottom and top GaN layers are p- and n-doped, respectively, a p-n-junction can be designed around an (In,Ga)N quantum well (QW). The optoelectronic properties of this heterostructure can be controlled by changing the QW thickness and its chemical composition. This enables band gap engineering via strain [90–92]. However, the large lattice mismatch of about $[a(\mathrm{InN}) - a(\mathrm{GaN})]/a(\mathrm{GaN}) \approx 10\,\%$ between GaN and InN makes the growth of In-rich (In,Ga)N layers very challenging. In fact, the quantum efficiency decreases drastically beyond an In content of approximately 30 % resulting in a weak light exploitation. In that regime green light is emitted. As a band gap design for

emitting green light is difficult to achieve also with other compound semiconductors, this valley in the internal quantum efficiency curve is known as the green gap [88, 93–95]. Explanations for the drop in internal quantum efficiency are on the one hand the electrostatic potential which increases with increasing In content and on the other hand non-radiative recombination associated with defects due to the large lattice mismatch.

Furthermore, in III-nitride heterostructures, the internal polarization potential is additionally modified by the quantum-confined Stark effect [80, 96] which describes the spatial separation of electrons and holes yielding a decreased overlap of their wavefunctions and, thus, poor radiative recombination rates [97]. Apparently, this effect is crucial for the optoelectronic performance of potential devices and has been subject to investigation [98–101]. As a consequence, the growth and device design along non-polar and semi-polar directions becomes interesting [102–104]. Without an internal electric field, the optoelectronic properties are mainly dominated by the quantum confinement of electron and hole wavefunctions and the In content.

A possible way to overcome these obstacles is the growth of low-dimensional objects such as nanowires (NWs) or micro-rods. Due to their three-dimensional (3D) geometry, higher amounts of In can be facilitated without resulting in plastic relaxation. The critical layer thickness in heterostructure NWs has been investigated for axial and radial geometries [62, 105–111] and has been found to be significantly improved compared to planar structures [112–116]. In fact, the high surface-to-volume ratio of these structures allows an efficient strain release via elastic deformation of the outer surface. This presents a crucial difference compared to planar structures.

2.2 A brief introduction to linear elasticity theory

Linear elasticity theory is a branch of continuum mechanics and deals with the elastic behavior of solids subject to deformation. It is a non-atomistic description and valid if the investigated effects occur on much larger length scales compared to the atomic distances [70]. Linear elasticity theory considers elastic, reversible deformations of volume elements, only. Hence, plastic deformations which are irreversible, e. g., the formation of dislocations in crystals are usually not covered. However, also the far-field around dislocations has been studied using the extended finite element method [117, 118].

The continuous deformation of a solid can be described by a vector field $\mathbf{u}(\mathbf{r})$ defined as

$$\mathbf{u}(\mathbf{r}) = \mathbf{r}' - \mathbf{r}\,, \tag{2.2.1}$$

where $\mathbf{r}$ is the position in the ideal, unstrained system and $\mathbf{r}'$ is the position in the deformed system. In the limit of small, homogenous deformations where

$$\frac{\partial u_\mathrm{i}}{\partial x_\mathrm{j}} \ll 1\,, \tag{2.2.2}$$

ij	=	11	22	33	23,32	13,31	12,21
⇓		⇓	⇓	⇓	⇓	⇓	⇓
α	=	1	2	3	4	5	6

Table 2.1 Voigt notation for mapping a tensor to a lower-rank object.

which is the fundamental requirement of linear elasticity theory, the deformation u_i along the direction x_j defines the dimensionless local strain tensor component e_{ij} at a certain position in three dimensions

$$e_{ij} = \frac{\partial u_i}{\partial x_j}, \quad i,j \in \{1,2,3\}. \tag{2.2.3}$$

Any second-rank tensor can be written as the sum of a symmetric, ε_{ij}, and an antisymmetric, ω_{ij}, tensor given by

$$\varepsilon_{ij} = \frac{1}{2}\left(\frac{\partial u_i}{\partial x_j} + \frac{\partial u_j}{\partial x_i}\right), \quad \omega_{ij} = \frac{1}{2}\left(\frac{\partial u_i}{\partial x_j} - \frac{\partial u_j}{\partial x_i}\right). \tag{2.2.4}$$

The antisymmetric part describes a rigid-body rotation which, due to the absence of internal torques will not be considered. Consequently, the strain state of a system will be described by the components ε_{ij} of the symmetric tensor which from now on will be referred to as strain tensor. The diagonal elements of the strain tensor, with $i = j$, are called normal components whereas the off-diagonal elements, with $i \neq j$, are called shear components. In three dimensions there are 9 strain components. However, with the requirement that there exists no net torque on a volume element, $\sigma_{ij} = \sigma_{ji}$, the number of independent components reduces to 6.

Under the assumptions mentioned above a linear relation between stress and strain called Hooke's law

$$\sigma_{ij} = c_{ijkl}\varepsilon_{kl}, \tag{2.2.5}$$

is valid, where the fourth-rank tensor is called elasticity tensor and its components c_{ijkl} elastic constants. In Voigt notation the order of a symmetric tensor is reduced by combining two indexes two one according to Tab. 2.1 which applied to Eq. 2.2.5 yields

$$\begin{bmatrix}\sigma_1\\ \sigma_2\\ \sigma_3\\ \sigma_4\\ \sigma_5\\ \sigma_6\end{bmatrix} = \begin{bmatrix} c_{11} & c_{12} & c_{13} & c_{14} & c_{15} & c_{16}\\ c_{12} & c_{22} & c_{23} & c_{24} & c_{25} & c_{26}\\ c_{13} & c_{23} & c_{33} & c_{34} & c_{35} & c_{36}\\ c_{14} & c_{24} & c_{34} & c_{44} & c_{45} & c_{46}\\ c_{15} & c_{25} & c_{35} & c_{45} & c_{55} & c_{56}\\ c_{16} & c_{26} & c_{36} & c_{46} & c_{56} & c_{66}\end{bmatrix} \begin{bmatrix}\varepsilon_1\\ \varepsilon_2\\ \varepsilon_3\\ \gamma_4\\ \gamma_5\\ \gamma_6\end{bmatrix}, \tag{2.2.6}$$

with $\gamma_\alpha = 2\varepsilon_\alpha$. From the symmetry properties of σ_{ij} and ε_{ij} it follows that $c_{ij} = c_{ji}$. Consequently, there are at most 21 independent elastic coefficients. Depending on the crystal system, the number of independent elastic constants can be further reduced. The triclinic crystal system, which has no symmetry axis, has the full number of 21 independent elastic constants whereas the cubic system has the minimum number of only three independent components. The polar anisotropic hexagonal crystal system which is inherent to the wurtzite III-nitride compound semiconductors discussed in this thesis has five independent elastic constants and the corresponding elasticity tensor reads

$$\begin{bmatrix} c_{11} & c_{12} & c_{13} & 0 & 0 & 0 \\ c_{12} & c_{11} & c_{13} & 0 & 0 & 0 \\ c_{13} & c_{13} & c_{33} & 0 & 0 & 0 \\ 0 & 0 & 0 & c_{44} & 0 & 0 \\ 0 & 0 & 0 & 0 & c_{44} & 0 \\ 0 & 0 & 0 & 0 & 0 & \frac{c_{11}-c_{12}}{2} \end{bmatrix} . \tag{2.2.7}$$

2.3 Piezoelectric polarization

In response to an applied stress along a polar axis, certain crystalline materials without inversion symmetry exhibit a macroscopically measurable electric voltage. This phenomenon is known as the direct piezoelectric effect. Vice versa, these solids deform under an applied external voltage called the converse piezoelectric effect. In the elastic regime, both piezoelectric phenomena are reversible.

Under an applied stress, e. g., by an external force [27, 119–121] or by internal strain caused by epitaxially combining several lattice mismatched materials [122–127], atoms are displaced and the unit cell deforms such that dipoles are induced. The sum of microscopic dipoles defines the macroscopic piezoelectric polarization $\mathbf{P}_{\mathrm{pz}}$ which is a vector field. Some piezoelectric materials with a single polar axis and no inversion symmetry also exhibit an intrinsic, spontaneous polarization $\mathbf{P}_{\mathrm{sp}}$ resulting in a permanent electric field. In this case, the total electric polarization in a material is given by the sum of both contributions

$$\mathbf{P}_{\mathrm{tot}} = \mathbf{P}_{\mathrm{pz}} + \mathbf{P}_{\mathrm{sp}} . \tag{2.3.1}$$

Polarization fields in heterostructures are of crucial importance for their optical properties as they directly manipulate the band gap.

In the linear regime the piezoelectric polarization is related to the strain tensor via the third-rank piezoelectric tensor e_{ijk},

$$P_{\mathrm{pz},i} = \sum_{jk} e_{ijk}\varepsilon_{jk} , \quad i,j,k \in \{1,2,3\} . \tag{2.3.2}$$

Interestingly, when changing the strain state from tensile to compressive the direction of the piezoelectric polarization can be reversed. As a consequence of

the converse piezoelectric effect which relates the symmetrical strain tensor and the electric field intensity there exists a symmetry in j and k leading to 18 independent piezoelectric tensor components. Plugging Eq. 2.3.2 into Eq. 2.3.1 and using the matrix notation with $jk \rightarrow \alpha$ according to Tab. 2.1 the total electric polarization reads

$$\begin{bmatrix} P_{\mathrm{tot},x} \\ P_{\mathrm{tot},y} \\ P_{\mathrm{tot},z} \end{bmatrix} = \begin{bmatrix} e_{11} & e_{12} & e_{13} & e_{14} & e_{15} & e_{16} \\ e_{21} & e_{22} & e_{23} & e_{24} & e_{25} & e_{26} \\ e_{31} & e_{32} & e_{33} & e_{34} & e_{35} & e_{36} \end{bmatrix} \begin{bmatrix} \varepsilon_1 \\ \varepsilon_2 \\ \varepsilon_3 \\ \gamma_4 \\ \gamma_5 \\ \gamma_6 \end{bmatrix} + \begin{bmatrix} P_{\mathrm{sp},x} \\ P_{\mathrm{sp},y} \\ P_{\mathrm{sp},z} \end{bmatrix} . \tag{2.3.3}$$

For materials with a [0001]-oriented wurtzite crystal structure there exists a singular polar axis to which $\mathbf{P}_{\mathrm{sp}}$ aligns. Furthermore, based on symmetry considerations it can be shown that there are three independent piezoelectric constants, e_{15}, e_{31} and e_{33} and the piezoelectric tensor simplifies to

$$\begin{bmatrix} 0 & 0 & 0 & 0 & e_{15} & 0 \\ 0 & 0 & 0 & e_{15} & 0 & 0 \\ e_{31} & e_{31} & e_{33} & 0 & 0 & 0 \end{bmatrix} , \tag{2.3.4}$$

such that the total polarization can be computed as

$$\mathbf{P}_{\mathrm{tot}} = \begin{bmatrix} e_{15}\gamma_5 \\ e_{15}\gamma_4 \\ e_{31}(\varepsilon_1 + \varepsilon_2) + e_{33}\varepsilon_3 + P_{\mathrm{sp},z} \end{bmatrix} . \tag{2.3.5}$$

The variation of the polarization results in a change of the charge density $\rho(\mathbf{r})$ upon the crystal faces

$$\rho(\mathbf{r}) = -\nabla \cdot \mathbf{P}_{\mathrm{tot}}(\mathbf{r}) , \tag{2.3.6}$$

and changes the induced electric field. The electric potential $V_{\mathrm{p}}(\mathbf{r})$ is related to the polarization and the electric charge density displacement $\mathbf{D}$ via

$$\mathbf{D} = -\kappa(\mathbf{r})\nabla V_{\mathrm{p}}(\mathbf{r}) + \mathbf{P}_{\mathrm{tot}}(\mathbf{r}) , \tag{2.3.7}$$

where the permittivity $\kappa(\mathbf{r})$ is the product of the relative permittivity $\kappa_{\mathrm{r}}(\mathbf{r})$ of the material and the vacuum permittivity κ_0. By solving Maxwell's equation for the electric charge density displacement in absence of external charges, $\nabla \cdot \mathbf{D} = 0$, Poisson's equation for the electric potential is obtained

$$\nabla \cdot (\kappa(\mathbf{r})\nabla V_{\mathrm{p}}(\mathbf{r})) = \nabla \cdot \mathbf{P}_{\mathrm{tot}}(\mathbf{r}) . \tag{2.3.8}$$

which usually has to be solved to compute $V_{\mathrm{p}}(\mathbf{r})$.

2.4 The finite element method in solid mechanics

Heterostructure NWs and rods in for example axial or core-shell geometry exhibit internal stresses originating from the lattice mismatch between the different materials. Under certain simplifications, the inherent deformation field in NWs can be accessed analytically [128, 129]. These involve a simplification of the shape to a circular cylinder of infinite length as well as spatially constant material parameters of only one compound throughout the full model. However, for many physical problems the actual shape, chemical composition, applied forces and boundary conditions have to be taken into account, and, consequently, an analytic treatment becomes insufficient and other, i. e., numerical techniques have to be applied.

A powerful method to provide a numerical approximation of the exact solution to boundary value problems for partial differential equations is the FEM approach. The basic idea is to subdivide a model of arbitrary complexity into simpler geometrical entities defined by nodal coordinates at its vertexes. For each element an equilibrium equation is established which yield local approximations to the global solution. The element equations are assembled to an equation system and boundary conditions are imposed. The FEM relies strongly on the use of computers and due to the wide range of problems in engineering and fundamental science that can be solved by FEM a few highly sophisticated software packages are available. The simulations presented in this thesis were performed using the commercial software package MSC.Marc2008rl with the graphical interface MSC.Mentat which was developed on the basis of the displacement-based FEM where the nodal displacements are the primary unknowns. In the following, a brief introduction to the underlying mathematical concepts of the displacement method shall be given.

In structural mechanics the displacement method is based on the minimization of the total potential energy with respect to the displacement field $\mathbf{u}$. This means that in its equilibrium state the total potential Π of a body is minimized. The total potential for a linear elastic continuum reads

$$\Pi = E_{\mathrm{elastic}} + E_{\mathrm{pot}} \,, \tag{2.4.1}$$

where E_{elastic} is the elastic strain energy

$$E_{\mathrm{elastic}} = \frac{1}{2} \int_V \boldsymbol{\varepsilon}^{\mathrm{T}} \mathbf{C} \boldsymbol{\varepsilon} \mathrm{d}V \,, \tag{2.4.2}$$

with $\boldsymbol{\varepsilon}$ being the strain tensor in Voigt notation whereas $\boldsymbol{\varepsilon}^{\mathrm{T}}$ is the transpose of the tensor and $\mathbf{C}$ the elasticity tensor which are defined in Eq. 2.2.5. Hereby, isotropic and anisotropic material behavior which exhibits different elastic properties in different directions can be taken into account. The elastic strain energy is also referred to as internal work which is the response to the external work

acting on the body. The external work is included into the potential energy E_{pot} defined as

$$E_{\text{pot}} = -\int_V \mathbf{u}^{\text{T}}\mathbf{f}^{\text{B}}\text{d}V - \int_S \mathbf{u}^{\text{T}}\mathbf{f}^{\text{S}}\text{d}S\,, \tag{2.4.3}$$

whereas the first integral describes the action of body forces $\mathbf{f}^{\text{B}}$ and the integration proceeds over the entire volume V of the body and the second integral includes the surface forces $\mathbf{f}^{\text{S}}$ acting on the body surface S.

To determine the equilibrium strain distribution in the solid, the displacement field $\mathbf{u}$ is varied to minimize the total potential. At equilibrium, a stationary total potential is required, $\delta\Pi = 0$, yielding

$$\delta\Pi = \delta E_{\text{elastic}} + \delta E_{\text{pot}} = 0\,. \tag{2.4.4}$$

This means that at equilibrium the external work acting on the body equals the internal work

$$\int_V \delta\boldsymbol{\varepsilon}^{\text{T}}\mathbf{C}\boldsymbol{\varepsilon}\text{d}V = \int_V \delta\mathbf{u}^{\text{T}}\mathbf{f}^{\text{B}}\text{d}V + \int_S \delta\mathbf{u}^{\text{T}}\mathbf{f}^{\text{S}}\text{d}S\,. \tag{2.4.5}$$

Here, $\delta\boldsymbol{\varepsilon}$ describes a variation of the elastic strain and $\delta\mathbf{u}$ the underlying variation of possible displacements that are continuous and satisfy the displacement boundary conditions. This concept of virtual displacements can be directly related to the principle that the total potential must be stationary and, thus, can be used to find the equilibrium equations for each element.

The equilibrium equation Eq. 2.4.5 can be rewritten as the sum of equilibrium equations for each element

$$\begin{aligned}\sum_m \int_{V_{(m)}} \delta\boldsymbol{\varepsilon}^{\text{T}}_{(m)}\mathbf{C}_{(m)}\boldsymbol{\varepsilon}_{(m)}\text{d}V_{(m)} \;&=\; \sum_m \int_{V_{(m)}} \delta\mathbf{u}^{\text{T}}_{(m)}\mathbf{f}^{\text{B}}_{(m)}\text{d}V_{(m)} \\ &+ \sum_m \int_{S_{(m)}} \delta\mathbf{u}^{\text{T}}_{(m)}\mathbf{f}^{\text{S}}_{(m)}\text{d}S_{(m)}\,.\end{aligned} \tag{2.4.6}$$

Now, the integration area is the m^{th} element and the sum goes over the total number of elements in the body. Eventually, the assemblage element equations provides an equation system which approximates the global solution.

In the FEM, the deformation of the body is evaluated at the nodal coordinates and the continuous deformation at any position is interpolated from the nodal displacement. Therefore, the displacement $\mathbf{u}_{(m)}$ of the m^{th} element must be formulated in terms of the nodal displacement vector $\hat{\mathbf{u}}$ via

$$\mathbf{u}_{(m)} = \mathbf{H}_{(m)}\hat{\mathbf{u}}\,. \tag{2.4.7}$$

by introducing the displacement interpolation matrix $\mathbf{H}_{(m)}$. By inserting the

strain-displacement relation

$$\boldsymbol{\varepsilon}_{(m)} = \mathbf{B}_{(m)}\hat{\mathbf{u}} \tag{2.4.8}$$

where $\mathbf{B}_{(m)}$ is the strain-displacement matrix and Eq. 2.4.7 into Eq. 2.4.6 the equilibrium equations for each element can be assembled to a linear equation system of the form

$$\mathbf{K} \cdot \hat{\mathbf{u}} = \mathbf{f}\,, \tag{2.4.9}$$

where $\mathbf{K}$ is called the global stiffness matrix which is the sum of all element stiffness matrices

$$\mathbf{K} = \sum_m \mathbf{K}_{(m)} = \sum_m \int_{V_{(m)}} \mathbf{B}_{(m)}^{\mathrm{T}} \mathbf{C}_{(m)} \mathbf{B}_{(m)} \mathrm{d}V_{(m)}\,. \tag{2.4.10}$$

Importantly, all element stiffness matrices have the same dimension as the global stiffness matrix which yields sparse element matrices. The multiplication of the stiffness matrix with the nodal displacement vector yields the nodal load vector $\mathbf{f}$ which includes the forces acting on the body. The integrals are evaluated numerically. For solving the equation system direct or iterative methods can be applied whereas iterative solvers were used for all simulations presented in this thesis. The solution of the equation system gives a numerical approximation to the exact solution of the entire problem. The locality of the element equations leads to sparse equation systems which helps to solve problems with very large number of nodal unknowns. For the solution of the set of algebraic equations, initial, boundary and continuity conditions are considered. Apparently, the discretization density is an important issue concerning how well the exact solution is approximated. However, the computational effort scales with the number of finite elements which has to be taken into account.

2.5 Properties of hard x-rays generated in a synchrotron

Hard x-rays are electromagnetic waves with photon energies above 5-10 keV which translate to wavelengths in the range of 1 Ångstrøm (10^{-10} m) or smaller. Due to the fact, that the wavelength is in the order of inter-atomic distances hard x-rays are highly suitable to probe lattice parameters and the deformation of lattice planes in a crystal. Importantly, they have a high penetration depth into crystals and interact non-destructively.

There exist different sources for x-ray beams ranging from laboratory sources such as x-ray tubes up to large research facilities like synchrotrons. The x-ray beam quality is characterized by its brilliance which sets the number of emitted photons per second in relation with its divergence $(\mathrm{mrad})^2$, the source size (mm^2)

and the bandwidth

$$\text{brilliance} = \frac{\text{photons/second}}{(\text{mrad})^2\,(\text{mm}^2)(0.1\%\,\text{bandwidth})}\,. \tag{2.5.1}$$

Here, the denominator is the beam intensity and the product of divergence and source size is called emittance. Modern synchrotrons exceed the brilliance of laboratory sources by more than 12 orders of magnitude. They are circular particle accelerators where electrically charged particles such as electrons or positrons are confined in a closed and approximately circular loop using magnetic fields. They are accelerated nearly to the speed of light and kept at constant energy which in case of PETRAIII at DESY in Hamburg (Germany) is 6 GeV [130]. When these high-energy particles are forced to travel in a curved path they emit synchrotron radiation.

The experiments presented in this thesis were performed at the European Synchrotron Radiation Facility (ESRF) in Grenoble (France) and at PETRAIII which are both 3$^{\text{rd}}$-generation synchrotrons. Both synchrotrons are operated in top-up mode with a periodic refill of electrons (ESRF) or positrons (PETRAIII). For example, at PETRAIII the positron current in the storage ring is 100 mA with a maximum number of bunches of 960 which are separated by 8 ns [130]. Due to the fact, that the particle distribution in the ring is not continuous but bunched, the emitted synchrotron radiation is pulsed. This can be exploited for time-resolved investigations.

There exist different devices used as sources for synchrotron radiation. The magnetic fields forcing the particles into a closed orbit are produced by bending magnets. The radius ρ of the orbit on which the particle with charge e travels is defined by its relativistic energy $E_\text{e} = mc^2/\sqrt{1-(v/c)^2}$ and the applied magnetic field B via $\rho = \gamma mc/Be$, where $\gamma = E_\text{e}/mc^2$ is the electron energy in units of its rest mass energy. The bending magnets produce a continuous radiation spectrum which at the ESRF is also used for experiments. In between two bending magnets there are straight segments where so-called insertion devices (IDs) can be placed. This ID is either a wiggler or an undulator. Both of them are far more efficient x-ray sources compared to bending magnets and the brilliance of an undulator is superior compared to a wiggler. The experimental data presented in chapters 5 and 6 were performed at beamlines ID13 (ESRF) and P06 (PETRAIII), respectively, which both use an undulator x-ray source. For example, at beamline P06 a 2 m long undulator U32 is used with a magnetic period length of 31.4 mm proving a source brilliance of 10^{19} ph/s/0.1% bw/mA [131].

Insertion devices consist of a periodic structure of dipole magnets with alternating poles as sketched in Fig. 2.3 inducing a static magnetic field. This forces the charged particles to execute small-amplitude oscillations with the undulator period λ_u resulting in a radiation cone of emitted photons which is emitted along the average trajectory of the particle bunch in the same plane as the storage ring. The emitted radiation is linearly polarized in the same plane. Note that, if the undulator is constructed such that the particle beam performs a helical oscillation trajectory the emitted radiation will be circularly polarized.

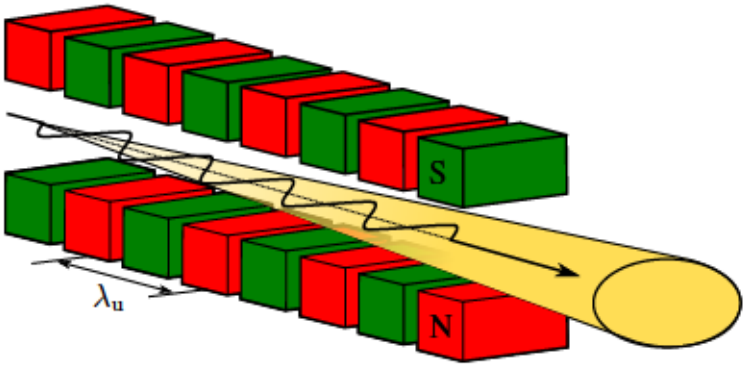

Figure 2.3 Sketch of an undulator which consists of an alternating sequence of dipole magnets. When the electron beam enters the undulator it is forced to oscillate at a characteristic wavelength, λ_u. Thereby, x-ray photons are emitted which add up coherently.

The important difference between wigglers and undulators is that in undulators the amplitude of the performed oscillations is smaller such that the emitted radiation from each oscillation adds up coherently and interferes. In contrast, the emitted photons of a wiggler add up incoherently. As a consequence, the spectrum emitted by a wiggler is continuous whereas undulators emit quasi-monochromatic radiation with a fundamental wavelength and higher harmonics. In comparison to bending magnets and wigglers, undulators provide synchrotron radiation with the lowest divergence. Here, the opening angle scales with $1/\sqrt{N}$ both vertically and horizontally where N is the number of periods. However, the angular divergence of the particle bunch is added such that the total divergence of the source becomes asymmetric with a larger divergence in the horizontal plane. At P06 the source divergence is about $28\times4\,\mu\text{rad}^2\sigma$ at 12 keV [131]. When increasing the undulator gap the magnetic field decreases such that the particles perform oscillations with a smaller amplitude. Consequently, x-ray photons with higher energy are emitted. The transition from a wiggler to an undulator is described by the dimensionless parameter K defined as $K = eB\lambda_u/2\pi mc$. For $K \leq 1$ the ID behaves as an undulator and for $K > 1$ as a wiggler.

When the x-ray beam enters the beamline, it passes several components to shape the beam and to select a specific wavelength. For hard x-rays, the latter is generally done using a crystal monochromator which allows to extract a monochromatic beam of adjustable wavelength from the incoming x-ray beam. The process of selecting an energy band is based on Bragg diffraction which will be subject to section 2.8. In order to preserve the good angular collimation of the x-ray beam, crystals with high crystal perfection are used. Moreover, they must sustain large heat loads which leaves only several materials to choose from. Commonly used materials are Si, C and Ge.

For example, at P06, Si(111) crystals are utilized providing an energy resolution of about 10^{-4} [131]. Interestingly, the energy resolution scales with the atomic number Z in the way that the selected bandwidth increases with higher Z and the energy resolution decreases. At the same time the relative intensity increases with higher Z such that the minimization of the energy resolution and

the maximization of the intensity are competing processes. Moreover, when using a reflection with large Miller indexes which means a larger magnitude of the respective q vector, the energy resolution increases. For example, the energy resolution provided by a Si(220) monochromator is larger compared to a Si(111) monochromator. The energy resolution is a key parameter as it sets a limit to the accuracy of the experiment.

2.6 Focusing of hard x-rays

The possibility to produce highly focused x-ray beams requires special optical equipment differing from common optics available for visible light. On the one hand, in case of hard x-rays the refractive index given by

$$n = 1 - \delta + \mathrm{i}\beta \tag{2.6.1}$$

is slightly smaller than unity. Here, the real part describes refraction and the imaginary part is related to absorption. In the former part δ describes the deviation from vacuum and in case of hard x-rays yields 10^{-5} in solids and 10^{-8} in air. Consequently, the phase velocity is greater than the speed of light. This is due to the fact that in the x-ray regime the frequency of the photons is higher than the resonance frequency of atomic electrons forced to oscillate in the electromagnetic field.

On the other hand, an important issue is the choice of material for fabricating optics with high transmission coefficients in the hard x-rays regime. Photoelectric absorption is described by $\beta = \mu/2k$ in Eq. 2.6.1, where μ is the absorption coefficient and k is the modulus of the wavevector. The photoelectric absorption cross-section for x-rays varies approximately as Z^4 [33]. Hence, light elements such as Be, B or C are suitable as a focusing medium. In fact, for x-ray optics often only about 10 % of the incoming beam are actually used [76].

In recent years, several successful approaches have been presented and since then the focusing capabilities have been continuously improved. Nowadays, there exist a variety of x-ray optics with suitable focal lengths and transmission properties, for example refractive optics such as lenses [132], diffractive optics such as Fresnel zone plates (FZPs) [133–135] and reflective optics such as Kirkpatrick-Baez mirrors (KB mirrors) [136, 137].

The FZPs consist of a cylindrical disk with concentric rings of alternating opaque and transparent regions called Fresnel zones. The impinging wavefront is diffracted around the opaque zones. In general, zone plates are fabricated using electron beam lithography and etching methods and the transparent material can be, e. g., Si and the opaque material Au. However, there also exist other approaches for example based on NWs [138]. There are two physical scenarios for producing a focused beam with FZPs which both are based on constructive interference. First, the incoming wavefront can be absorbed in the opaque zones and the transmitted parts interfere due to different optical path lengths. Second, the opaque zones can induce a phase shift between diffracted wavefronts which

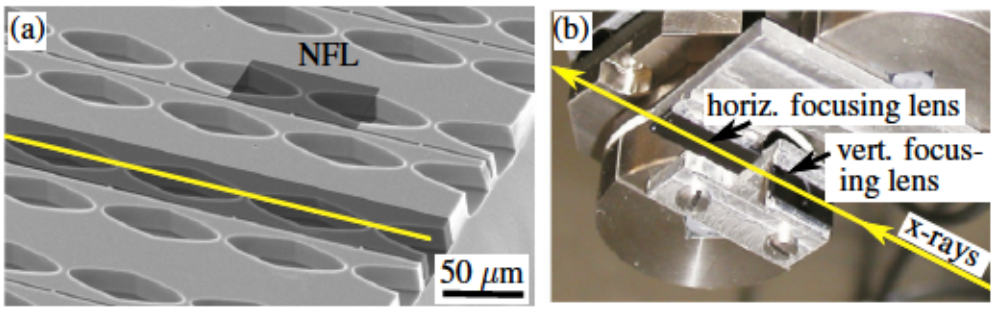

Figure 2.4 Nanofocusing lenses made of Si. In (a), a single nanofocusing lens (NFL) which has a concave shape is highlighted. For different x-ray energies different lens designs have to be used to achieve a certain focus size. One stack of NFLs is shown in dark gray and the path of the x-ray beam is indicated by the yellow straight line. In contrast to compound refractive lenses, nanofocusing lenses focus the x-ray beam in one direction, only, and to achieve focusing also in the perpendicular direction two stacks of lenses in a crossed geometry have to be used as shown in (b). The images are taken from Ref. [139].

in the case of π leads to constructive interference. The focal distance scales with the x-ray energy. The required aspect ratio of zone width and thickness for applications in the hard x-ray regime is challenging to fabricate such that they are more commonly used for focusing x-rays below 10 keV. At the nanoprobe beamline P06 FZPs are used in the energy range of 7-10 keV and spot sizes of about $30\times30\,\mathrm{nm}^2$ can be achieved [131].

The KB geometry consists of two bent mirrors which are placed orthogonal to each other. One mirror focuses the x-ray beam vertically the other horizontally. The mirrors are curved and mainly elliptical or parabolic shapes are used. In order to maintain the intensity of the impinging beam its incident angle on the mirrors has to be below or equal the critical angle

$$\alpha_c \approx \sqrt{2\delta}\,, \tag{2.6.2}$$

which concerning hard x-rays is generally about 0.5° or smaller. Here, δ describes the deviation of the refractive index from unity as defined in Eq. 2.6.1. At an angle equal or below the critical angle, total external reflection of the x-ray beam is observed. Often the critical angle and, thus, the mirror's acceptance is increased by coating the surface with a high atomic number material, e. g., Au or Pt. Obviously, the surface quality regarding a low roughness and small slope errors is essential for the focusing performance. Moreover, the mechanical stability of the mirror setup with respect to the incoming beam is important. A great advantage of KB mirrors is their achromaticity allowing energy-resolved experiments. The microprobe setup at beamline P06 uses KB mirrors as focusing optics with which spot sizes of $250\times250\,\mathrm{nm}^2$ are achieved [131].

A consequence of a refractive index slightly smaller than unity is that the design of refractive optics is challenging. The small δ leads to a weak refraction effect of a single lens with realistic manufacturing parameters and the resulting focal lengths are too large for reasonable applications. Moreover, air is the optically denser medium such that in contrast to visible light optics, focusing of

x-rays is achieved using concave lenses.

Despite the challenges, efficient focusing optics based on refractive lenses have been fabricated. In order to achieve a reasonable focal length, stacks of identical lenses, so-called compound refractive lenses (CRL) [140] have been designed. In general, the lenses are made of Al or Be, have a parabolic shape and are fabricated by drilling or by embossing using mechanical punching. A more precise way of fabricating lenses can be achieved using lithography techniques. Due to its importance in technology, Si is a widely studied material and there exist many well-established processing techniques with the needed high precision. That is why it is the material of choice for designing so-called nanofocusing lenses (NFLs) which are shown in Fig. 2.4(a) [141, 142]. Due to the fact that etching proceeds in one direction, only, two stacks of lenses have to be used which are placed in an orthogonally crossed geometry as shown in Fig. 2.4(b). One stack of lenses focuses vertically and the other horizontally. One drawback of these refractive optics is the need of lens pairs designed for focusing x-rays at a specific energy.

The presented experiments in chapters 5 and 6 were performed using highly collimated x-ray beams which were focused using NFLs. Here, spot sizes of $150\times150\,\mathrm{nm}^2$ (ID13) and $80\times90\,\mathrm{nm}^2$ (P06) have been achieved. At beamline P06, CRLs have been used as pre-focusing optics with which the photon flux could be increased by two orders of magnitude to 10^9 photon/sec. The working distance at both beamlines is about 1 cm and the NFLs are used in an energy range from 10-30 keV. At beamlines ID13 and P06 the optical equipment is mounted in an optics hutch which is located just before the experimental hutch.

The development of highly efficient focusing optics in the hard x-ray regime triggered the development of new imaging and microscopy techniques which, nowadays, are vivid research fields at synchrotrons [47–49, 54, 143, 144]. Moreover, nanofocused synchrotron radiation offers a powerful new technique for characterizing material properties with spatial resolution without destructive sample preparation [36, 44]. With the technological and scientific interest in the properties of low-dimensional semiconductor heterostructures such as quantum dots and NWs, this technique allows to obtain information about local strain fields, chemical composition and structural properties of individual objects [35, 45, 50, 60, 145].

2.7 X-ray scattering geometries

An x-ray photon impinging on a periodic crystal can be scattered elastically or inelastically, transmitted, or absorbed. In the latter process, the energy of an x-ray photon can for example be transferred to an atomic electron which is either excited to a higher energy state or expelled from the atom. The created hole can be filled by an electron from a higher energy level resulting in the emission of an Auger electron or a photon with a characteristic energy whose detection can be used for a chemical analysis of a sample. While the former phenomenon is mainly a surface sensitive method, the fluorescence signal provides information

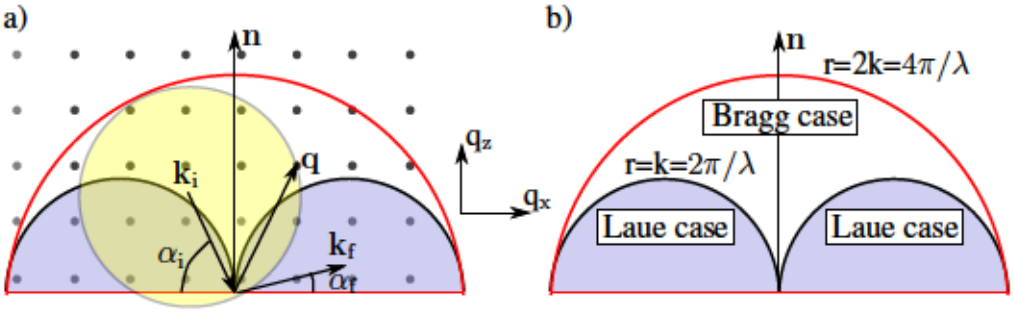

Figure 2.5 The incident x-ray beam, with wavevector $\mathbf{k}_i$, shown in (a) is impinging on the sample in a coplanar scattering geometry with an angle α_i and is elastically scattered under an exit angle α_f with wavevector $\mathbf{k}_f$. If the scattering vector $\mathbf{q}$ coincides with a reciprocal lattice point indicated by the gray spots in the background, which lies on the surface of the Ewald sphere shown in yellow, the Bragg condition is fulfilled. The hemisphere shown in red is the extended Ewald sphere with a radius of $r = 2k$. For a given wavelength this is the area in reciprocal space which can be reached by varying α_i and α_f. If $\alpha_i > 0$ and $\alpha_f > 0$ the incident beam is reflected (Bragg case) as shown in (b). If either α_i or α_f are negative a transmission geometry is established (Laue case). The beam is transmitted through the sample if $\mathbf{q}$ lies within one of the blue hemispheres.

about thicker volumes, too.

An example of an inelastic scattering process is Compton scattering where an x-ray photon is scattered on an electron including an energy transfer from the photon to the electron. This scattering process is incoherent. If the x-ray beam is scattered elastically the wavevectors of the incoming beam, $\mathbf{k}_i$, and of the emitted beam, $\mathbf{k}_f$, have the same magnitude or equivalently, the same frequency ω,

$$|\mathbf{k}_i| = |\mathbf{k}_f| = k = \frac{\omega}{c} = \frac{2\pi}{\lambda}, \tag{2.7.1}$$

and differ in their direction, only. The orientation of the vectors $\mathbf{k}_i$ and $\mathbf{k}_f$ with respect to the sample surface is specified via the incident angle α_i and an azimuthal angle β and an exiting angle α_f and the azimuthal angle γ. Using $\mathbf{k}_i$ and $\mathbf{k}_f$ the scattering vector $\mathbf{q}$ is defined as

$$\mathbf{q} = \mathbf{k}_f - \mathbf{k}_i = \frac{2\pi}{\lambda} \begin{pmatrix} \cos(\alpha_f)\cos(\gamma) - \cos(\alpha_i)\cos(\beta) \\ \cos(\alpha_f)\sin(\gamma) - \cos(\alpha_i)\sin(\beta) \\ \sin(\alpha_f) + \sin(\alpha_i) \end{pmatrix}, \tag{2.7.2}$$

with $|\mathbf{q}| = 2\pi/d$ where d is a distance, e. g., between lattice planes along a certain direction or between crystal interfaces. Importantly, the latter equality defines a relation of Fourier transform between the real-space distance, d, in the direct crystal and the reciprocal space vector $\mathbf{q}$ [76] of the corresponding reciprocal lattice. By changing the orientation of the crystal with respect to the incident x-ray beam or the wavelength λ, regions in reciprocal space can be mapped.

Using the extended Ewald sphere [146] which is sketched in Fig. 2.5, the potentially accessible region in reciprocal space that can be investigated for a given

wavelength λ is visualized. Figure 2.5(a) shows a coplanar scattering geometry where the surface normal $\mathbf{n}$ lies in the plane spanned by $\mathbf{k}_\mathrm{i}$ and $\mathbf{k}_\mathrm{f}$. In this case, the angles γ and β [cf. Eq. 2.7.2] are zero and the scattering plane is perpendicular to the surface. If $\mathbf{n}$ lies not in the scattering plane the scattering geometry is called non-coplanar. Around the incoming wavevector, the Ewald sphere is drawn in yellow. If the resulting vector $\mathbf{q}$ points to a reciprocal lattice point (drawn as gray spots in the background) which lies on the surface of the Ewald sphere the diffraction condition is fulfilled. If the corresponding reflection is not forbidden, an x-ray beam is scattered at an exit angle α_f. More details about the diffraction condition will be provided in section 2.8.

As long as $\mathbf{q}$ lies inside the red hemisphere with $r = 2k$ and outside the two blue hemispheres with $r = k$, the scattering geometry is called Bragg geometry as sketched in Fig. 2.5(b). This is the case if the x-ray beam is reflected under $\alpha_\mathrm{i} > 0$ and $\alpha_\mathrm{f} > 0$. The two blue hemispheres with radius $r = k$ can only be accessed if either $\alpha_\mathrm{i} < 0$ or $\alpha_\mathrm{f} < 0$ which corresponds to the situation where either the incoming beam or the diffracted beam penetrates through the sample. When the x-ray beam is transmitted through the sample, the Laue geometry is established. If the reciprocal space is mapped with small $\mathbf{q}$ values, corresponding to the region between the two blue hemispheres close to the origin [cf. Fig. 2.5(b)], the grazing incidence small angle x-ray scattering (GISAXS) geometry is applied which is a surface sensitive technique with hardly any sensitivity to lattice deformation. Another important experimental setup is the grazing incidence diffraction (GID) geometry which is the most non-coplanar case. Here, the x-ray beam is diffracted at small incident and exiting angles, on the lattice planes perpendicular to the surface and is mainly sensitive to the sample surface and in-plane lattice deformations.

Furthermore, the scattering geometry is distinguished by two cases which are visualized in Fig. 2.6. In case (a) it holds that the incident and exit angle are equal, $\alpha_\mathrm{i} = \alpha_\mathrm{f} = \Theta \equiv \Theta_\mathrm{B} + \delta$ and the scattering geometry is called symmetric. If $\delta = 0$ the incident angle is equal the Bragg angle Θ_B [cf. Eq. 2.8.1]. Here, the atomic distance between basal planes can be probed. Consequently, symmetric reflections are predominantly sensitive to out-of-plane relaxation. The scattering angle 2Θ defines the angle between incident and exiting x-ray beam. In case (b), an asymmetric scattering geometry is sketched which can be used to probe the distance between lattice planes which are inclined by an angle ϕ with respect to the surface. Here, the incident angle is $\omega \equiv \alpha_\mathrm{i} = \Theta + \phi$ whereas $\phi < \Theta$ and the exit angle is $\alpha_\mathrm{f} = 2\Theta - \omega$. Asymmetric reflections are sensitive to both, in-plane and out-of-plane deformation. By changing ω and 2Θ in a ratio of 1:2 the reciprocal space is mapped in radial direction which corresponds to a change of the absolute value of $\mathbf{q}$. The radial direction is sensitive to the strain normal to the lattice planes. By changing only ω the magnitude of $\mathbf{q}$ is kept constant and the reciprocal space is mapped in angular direction. As indicated in Fig. 2.6(b), the intensity of the diffracted beam is recorded by a linear detector. The resolution of the experiment can be improved by, e. g., increasing the distance between detector and sample, by choosing a detector with a smaller pixel size and by

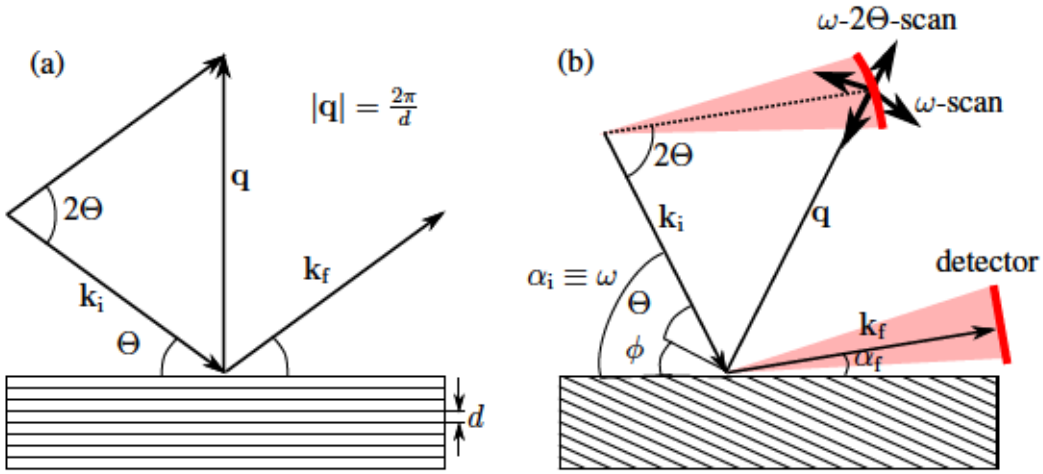

Figure 2.6 In the symmetric diffraction geometry, (a), the incident angle α_i and the exit angle α_f equal the angle $\Theta = \Theta_B + \delta$. If $\delta = 0$, the incident angle is equal the Bragg angle Θ_B. This diffraction geometry can be used to probe deformation of basal lattice planes. The angle 2Θ is called the scattering angle. The asymmetric diffraction geometry, (b), can be used to probe the deformation of inclined lattice planes and provides information about in-plane and out-of plane strain. Here, the angle ϕ describes the inclination between lattice planes and the sample surface. By changing ω and 2Θ simultaneously with a ratio of 1:2 the reciprocal space can be scanned in radial direction and by changing ω in angular direction.

measuring high order Bragg reflections where the peak of interest and the reference peak have a larger separation. However, higher order peaks require larger scattering angles which can sometimes not be accessed. Subsequently, the intensity pattern has to be transformed from detector coordinates into reciprocal space coordinates.

2.8 Kinematic x-ray scattering

An electromagnetic wave can be diffracted elastically from a crystal if the wavelength λ of the impinging beam fulfills the Bragg condition

$$2d\sin(\Theta_B) = \lambda\,, \tag{2.8.1}$$

which implies that $\lambda \leq 2d$, where Θ_B is the Bragg angle. When an x-ray photon is scattered only once and multiple scattering events are neglected the scattering process can be described in the kinematic approximation. The kinematic scattering regime implies weak interaction between photons and the crystal. If the Bragg condition is satisfied the scattered waves interfere constructively resulting in sharp reflection peaks also called Bragg peaks. If the wavelength is larger than $2d$ the x-ray beam can be reflected, only. Due to the fact that atomic distances are generally in the order of several Å, photon energies in the hard x-ray regime are necessary to probe atomic distances.

A consequence of the high frequency of x-rays is that the interaction with matter is mainly mediated by the electron density $\rho(\mathrm{r})$ around the atom nucleus.

This interaction is described by the atomic form factor

$$f(\mathbf{q}, \hbar\omega) = f^0(\mathbf{q}) + f'(\hbar\omega) + \mathrm{i}f''(\hbar\omega)\,, \tag{2.8.2}$$

which is in general complex. However, if the photon energy is not close to an absorption edge of the atom, the dispersion and absorption corrections f' and f'', respectively, can be neglected such that the atomic form factor reads

$$f^0(\mathbf{q}) = \int \rho(\mathbf{r}) e^{\mathrm{i}\mathbf{q}\cdot\mathbf{r}} \mathrm{d}\mathbf{r}\,, \tag{2.8.3}$$

which is the Fourier transform of the electron density $\rho(\mathbf{r})$. The latter is usually approximated with a spherical distribution. The atomic form factor is a measure of the amplitude of a wave scattered by an atom.

Using the definition of the atomic form factor the scattering amplitude of a crystal can be deduced. Here, one can bear in mind that a crystal is built by a periodic repetition of the unit cell which is translated by integer multiples of the lattice vector $\mathbf{r_n}$. Within the unit cell there are j atoms at positions $\mathbf{r}_j$. When looking at the scattering amplitude of a crystal given by

$$F(\mathbf{q}) = \overbrace{\sum_j f_j(\mathbf{q}) e^{\mathrm{i}\mathbf{q}\cdot\mathbf{r}_j}}^{\text{structure factor}} \overbrace{\sum_n e^{\mathrm{i}\mathbf{q}\cdot\mathbf{r_n}}}^{\text{lattice sum}}\,, \tag{2.8.4}$$

the first sum is the Fourier transform of the atomic form factor and is called the unit cell structure factor. The structure factor determines the relative intensity of the emitted x-ray beam which depends on the distribution of atoms in the unit cell and how well the photons are scattered from the individual atoms. In an x-ray diffraction experiment the electron density distribution within the unit cell, thus, the unit cell structure factor (actually its absolute square) is measured. From the knowledge of how electrons are arranged within the unit cell, the crystal structure can be obtained. The unit cell structure factor has to be evaluated at every lattice point governed by the lattice sum. The lattice sum comprises a huge amount of summands corresponding to the number of lattice points in a crystal. Each term of the lattice sum includes a phase factor $\phi_n = \mathbf{q} \cdot \mathbf{r_n}$. If all phases are equal a multiple of 2π the lattice sum yields a large number proportional to the number of summands. This leads to the situation where all scattered waves interfere constructively such that the Bragg condition is fulfilled resulting in an intense reflection spot.

For an infinite 3D crystal the lattice sum in Eq. 2.8.4 would yield a δ-peak. In contrast, for crystals of finite size, the scattering extends over a volume in reciprocal space which is inversely proportional to the size of the crystal. Hereby, flat surfaces result in scattering streaks normal to the surface which are called crystal truncation rods (CTRs). Mathematically, the transition from a crystal surface to the surrounding environment, e. g., along the z-direction, can be expressed by introducing a step function $h(z)$. The scattering amplitude Eq. 2.8.4 is then

proportional to the Fourier transform of the product of the electron density $\rho(z)$ and the step function which is equivalent to the convolution of their individual Fourier transforms. In case of $\rho(z)$, this yields a δ-function and for the step function i/q_z. As a consequence the intensity away from the Bragg peak decreases with $1/q_z^2$ resulting in streaks along this direction. These streaks can be modulated by the shape function of, e. g., a multi-layer sequence such that oscillations are visible referring to their layer thickness.

The scattered intensity $I(\mathbf{q})$ is obtained by multiplying Eq. 2.8.4 by its complex conjugate

$$I(\mathbf{q}) \propto |F(\mathbf{q})|^2 . \tag{2.8.5}$$

Importantly, the fact that the experimentally measured intensity is proportional to the absolute square of the scattering amplitude yields that the phase information is lost in an x-ray diffraction experiment such that the Fourier transform from reciprocal space to real space is not possible anymore. Otherwise one could easily retrieve the real space image of a unit cell by Fourier transform of its diffraction pattern. Nevertheless, using different scattering theory approaches as for example introduced in section 2.9, the diffraction pattern from artificial models can be simulated and by comparing simulation and experiment it is possible to deduce the real model. Additionally, when performing special scanning schemes with a coherent x-ray beam which are based on oversampling, phase retrieval algorithms can be used to reconstruct the lost phase information in an iterative procedure [47, 51, 147–149] and by that the corresponding real-space image can be found.

As becomes clear from the q-dependence of the intensity [cf. Eq. 2.8.5] x-ray diffraction does not provide a real space imaging of a crystal but transforms the real space information into the crystal's reciprocal space. In fact, a periodic distance in real space is translated into a frequency in reciprocal space and a diffraction pattern is a map of the reciprocal lattice of a crystal. As a consequence, the commonly used diffraction condition, the so-called Laue condition, is formulated in reciprocal space. It states that the emitted waves interfere constructively if the momentum transfer vector q coincides with the reciprocal lattice vector g,

$$\mathbf{q} \stackrel{!}{=} \mathbf{g} , \tag{2.8.6}$$

which is defined as

$$\mathbf{g} = h\mathbf{a}^* + k\mathbf{b}^* + \ell\mathbf{c}^* , \quad \{h, k, \ell\} \in \mathbb{Z} \tag{2.8.7}$$

where a*, b* and c* are the basis vectors of the reciprocal lattice. The reciprocal lattice vector is furthermore specified by the scalar product with the direct lattice vector given in Eq. 2.1.2

$$\mathbf{g} \cdot \mathbf{r_n} = 2\pi(hn_1 + kn_2 + \ell n_3) , \tag{2.8.8}$$

which fulfills the necessary requirement of being an integer multiple of 2π. The reciprocal lattice of a crystal consists of reciprocal lattice points each of them related to a set of lattice planes of the direct lattice. For example, in the cubic case a reciprocal lattice vector stands perpendicular to the set of planes having the same Miller indexes $(hk\ell)$ and the magnitude of g is inversely proportional to the distance between lattice planes, $|\mathrm{g}| = 2\pi/d_{hk\ell}$. The relationship in terms of distances and angles between a reciprocal lattice vector and the corresponding set of lattice planes of a hexagonal crystal having the same Bravais-Miller indexes $(hki\ell)$ is discussed in Ref. [150]. Based on the set of $(hk\ell)$ values, selection rules for space groups can be derived and yield for GaN (space group No. 186) the general reflection conditions

$$\begin{aligned} hh\overline{2h}\ell: &\qquad \ell = 2n\,, \\ 000\ell: &\qquad \ell = 2n\,. \end{aligned} \tag{2.8.9}$$

with n being an integer. For other combinations of $(hki\ell)$ there exist no further specific conditions for this space group.

2.9 Kinematic scattering from a deformed crystal

There exist several approaches based on different approximations for calculating the diffusely scattered intensity around Bragg reflections. For example, if multiple scattering events inside the crystal or refraction have to be taken into account, the dynamical scattering theory is required. Possible situations where this could be the case can be, e.g, x-ray scattering from large crystals with high perfection where the x-ray beam is reflected inside the crystal or scattering at small incident angles where x-ray refraction at material surfaces has to be considered. Due to multiple scattering events the intensity of the primary x-ray beam is reduced as a consequence of extinction. The kinematic approach neglects multiple scattering events and is justified for describing scattering from small objects or imperfect crystals. In the limit of weak scattering, the dynamical theory and the kinematic scattering theory are expected to lead to the same results. Intermediate the two theories there exists for example the distorted-wave Born approximation (DWBA) which is a first-order perturbation theory. In the DWBA, the scattering potential is divided into an undisturbed part and a small perturbation. The first part is treated dynamically and can be, e. g., the substrate, and the disturbed part is described in the kinematic approximation, e. g., a thin layer or low-dimensional objects grown on the substrate. The coupling of the waves field emitted from both parts is then treated within the DWBA.

If the investigated structure comprises different, lattice-mismatched materials, the crystal can be strained elastically resulting in a deformation of lattice planes. When simulating the diffraction pattern of such a structure, e. g., a sequence of planar layers or a heterostructure NW, this deformation has to be included. The simulated diffraction patterns presented in this thesis are based on the kinematic approximation and follow a classical approach which will be introduced in the

following.

The wavefront of the x-ray beam impinges on the crystal. As stated by the Huygens-Fresnel principle, the atoms in the crystal act as point scatterers each emitting a spherical wave oscillating with the same frequency as the incident x-ray beam. The spherical waves emitted from each scatterer add up coherently leading to interference. In the far-field limit, also known as Fraunhofer approximation, the evanescent wave which is the superposition of all emitted spherical waves can be considered as plane wave again.

When applying these assumptions, the scattered intensity can be expressed as

$$I(\mathbf{q}) \propto \left| \sum_{i}^{N} f_i(\mathbf{q}) e^{i\mathbf{q}\cdot(\mathbf{r_i}+\mathbf{u}(\mathbf{r_i}))} \right|^2 . \tag{2.9.1}$$

Here, the plane waves emitted from each atom are added up coherently whereas N is the total number of atoms in the illuminated volume. The position of the i-th atom is given by $\mathbf{r}_i$ and its displacement from the ideal position by the displacement vector $\mathbf{u}(\mathbf{r}_i)$. These parameters have to be known initially and serve as input for the coherent summation. Moreover, the scattering power of each individual atom can be weighted by the atomic form factor $f_i(\mathbf{q})$ which is defined in Eq. 2.8.2. The coherent summation is valid, only, if the spatial coherence of the x-ray beam is larger then the scattering object. For example, it is important to note that if scattering from an ensemble of nano-structures shall be simulated, correlation effects have to be taken into account. Then the scattered intensity from each object has to be computed and the scattered intensity from the individual objects has to be summed up to obtain the total intensity. In this case, the summation is incoherent. The intensity I is computed as function of $\mathbf{q}$ and in a simulation a slice or a volume in reciprocal space, generally around a reciprocal lattice point, can be selected.

In the case of (In,Ga)N/GaN NWs the atomic positions can be constructed by translating the unit cell along the lattice vector given in section 2.1. The strain induced deformation can be obtained by computing the deformation field $\mathbf{u}$ using the FEM as introduced in section 2.4. By interpolating the ideal crystal structure with the deformation field of an equivalent structure, e. g., constructed using the FEM, it is possible to retrieve the deformation vector for the i-th atom, $\mathbf{u}(\mathbf{r}_i)$. In this thesis, the interpolation process is performed using a specially developed source code for the commercial software package MATLAB R2012b. Employing the implemented *TriScatteredInterp* class based on the linear interpolation method the data set $\mathbf{u}(\mathbf{r}_i)$ is obtained. Of course one has to bear in mind that the diffusely scattered intensity will be based on purely linear elastic deformations of the crystal and that the influence of plastic relaxation is not included.

The fundamental idea of the interpolation process is visualized in Fig. 2.7. Here, the ideal crystal structure of GaN in form of a hexagonal NW is shown in Figs. 2.7(a) and (b) whereas only one atomic species is displayed and the lattice spacing is increased by a factor of 10 for better visibility. In a typical simulation the number of atoms is in the order of several millions and the lattice parame-

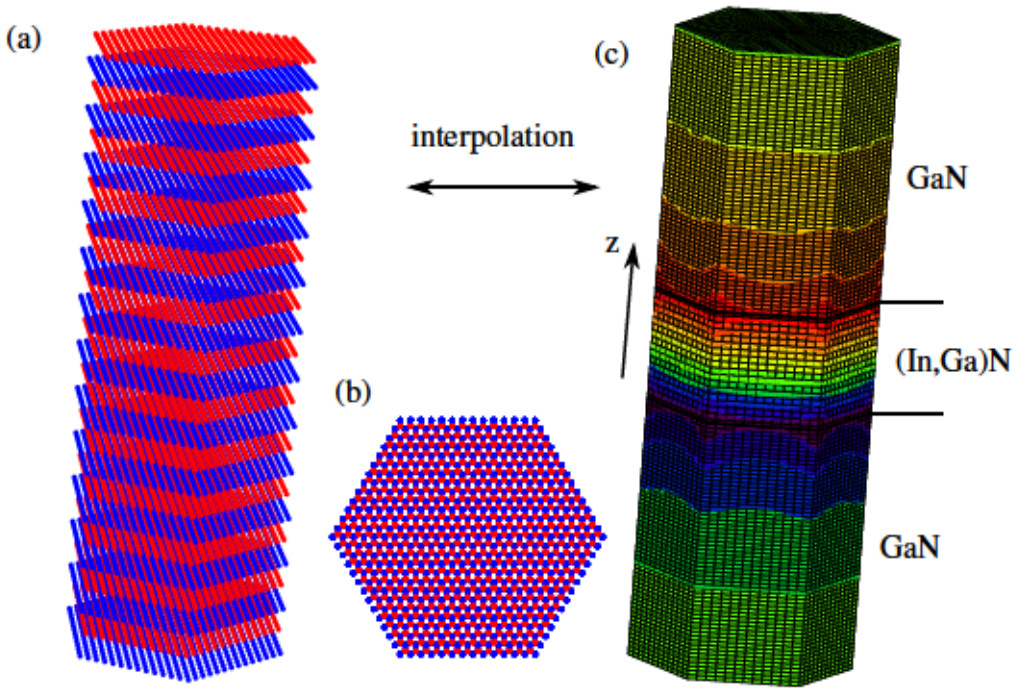

Figure 2.7 In (a) and (b) the ideal GaN crystal in the shape of a hexagonal NW is shown whereas for simplicity only one atomic species is displayed. Moreover the lattice constants are increased by a factor of 10 and only a fraction of the actually atomic layers are visible. The ideal atomic positions in the crystal are interpolated with the artificial grid obtained by the FEM. In (c) the deformation field along the z-axis which corresponds to the [0001]-direction is shown. Here, the FEM nodes in the bottom plane are kept fix to mimic the epitaxial relation to a substrate.

ter is increased by a factor of up to four. This approximation induces additional reflections in between higher order reflections. Hence, the region in reciprocal space has to be chosen in the way that these artificial reflections show no influence on the actual Bragg reflection. The ideal atomic positions are interpolated with a 3D grid of the deformation field. Here, the number of FEM nodes lies typically in the order of several hundred thousands. The distribution of nodes inside the FEM model can be varied such that regions where a complex strain distribution is expected, for example in the vicinity of QWs, comprise a higher density of nodes. Exemplary, in Fig. 2.7(c), the z-displacement simulated using the FEM is shown for an axial (In,Ga)N/GaN NW. Here, the FEM nodes in the bottom plane are kept fixed which corresponds to the boundary condition of an epitaxial relation to a substrate or buffer layer.

3 Geometry dependent strain distribution in axial (In,Ga)N/GaN nanowires

(In,Ga)N/GaN heterostructures are an integral part of light emitting devices used for full-color displays and solid state lighting. For conventional planar heterostructures, the In content in the (In,Ga)N QW is restricted due to the formation of dislocations beyond a certain critical stress as discussed at the end of section 2.1. However, low-dimensional (In,Ga)N/GaN heterostructures such as NWs are discussed as promising alternatives since their high aspect ratio and high surface-to-volume ratio are expected to facilitate the incorporation of higher amounts of In without resulting in plastic deformation. In fact, a NW can effectively release strain elastically close to its free surface, and thereby accommodate a higher lattice mismatch compared to a planar layer [62, 106].

The elastic strain relaxation in axial NW heterostructures depends on both the length of the strained segment and the radius of the NW, which therefore represent additional degrees of freedom to tune the emission wavelength [92, 129]. In contrast to planar structures, however, the strain distribution in a NW heterostructure is inherently 3D and more complex than commonly assumed.

This becomes clear when looking at Fig. 3.1(a). Here, the relaxation behavior of an (In,Ga)N layer embedded into a planar GaN matrix is sketched. The larger bulk lattice parameter of (In,Ga)N is compressed in in-plane direction to adopt the bulk lattice parameter of GaN. Consequently, the out-of-plane lattice parameter of (In,Ga)N is expanded such that the vertical normal component of the elastic strain tensor, ε_{zz}, will be positive at each position in the (In,Ga)N layer. Due to the large in-plane extension, shear strains are negligible. In contrast, Fig. 3.1(b) displays the ε_{zz}-component for a NW with a segment length of 10 nm which is equal the NW radius. The deformation of the NW is enhanced by a factor of 10 showing a convex deformation of the (In,Ga)N segment surface and a concave deformation of the (In,Ga)N segment at the GaN interfaces. Moreover, adjacent to the interfaces, the GaN matrix is deformed, too, by the strain induced by the (In,Ga)N segment. This observation stands in stark contrast to the case for planar systems. However, the most striking feature is the compressed volume in the segment center. This phenomenon is once again displayed in the plot in Fig. 3.1(c) showing the evolution of ε_{zz} along the NW height taken at the NW center along the black dashed line. Here, it can be observed that for an In content of 30 %, a significantly negative ε_{zz}-value of about -0.6 % is reached. The origin of this effect and its dependence on the NW geometry is subject to the following discussion. Parts of this chapter have been published in Ref. [151].

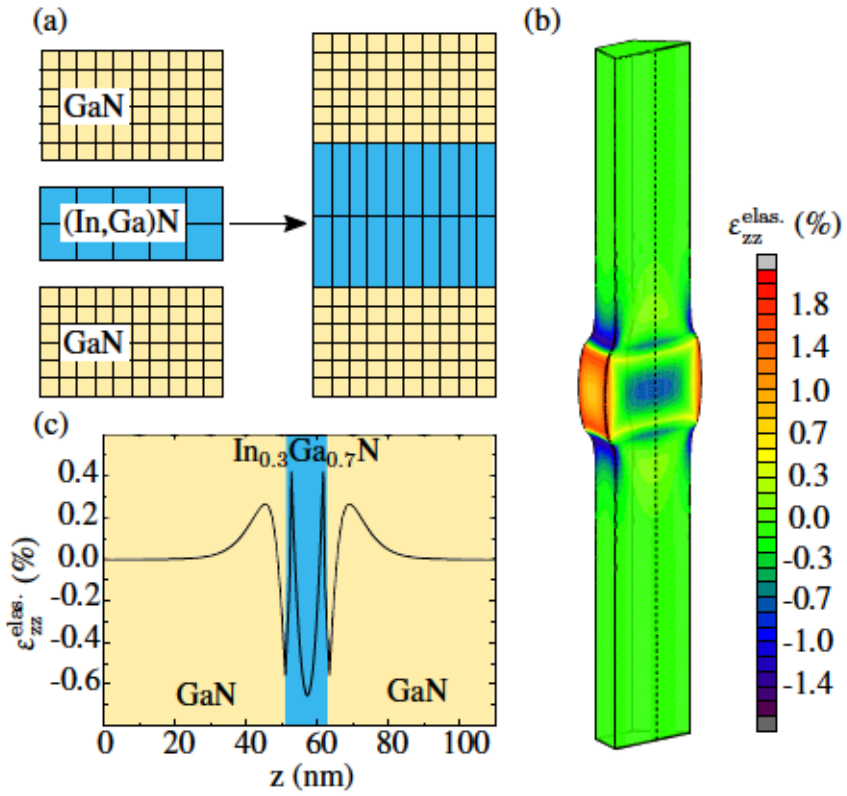

Figure 3.1 In (a), the relaxation of an (In,Ga)N layer embedded into a bulk GaN matrix is sketched. Here, the relaxation is mediated mainly by the normal components of the strain tensor. The larger in-plane lattice parameter of (In,Ga)N is compressed in order to adopt to the smaller lattice parameter of bulk GaN. Consequently, the out-of-plane lattice parameter of the (In,Ga)N layer is stretched. In (b), a finite element model of a 10 nm thick (In,Ga)N disk embedded between two GaN segments and the resulting 3D distribution of the strain tensor component, ε_{zz}, in cross-section is shown. For better visibility, the deformation of the nanowire has been enhanced by a factor of 10. Within the (In,Ga)N segment, negative values for ε_{zz} indicate tensile strain in the center, whereas the lattice in adjacent GaN regions is vertically expanded. This becomes clear when looking at the line plot (c) taken along the dashed vertical line through the nanowire center in (b). In the disk center, a negative ε_{zz}-value of about -0.6 % is observed.

3.1 Nanowire model and FEM simulation

The strain field induced by a lattice-mismatched segment in a NW can be obtained in closed form only when treating the NW as an infinitely long cylinder [129]. However, in order to take into account the actual hexagonal cross-sectional shape of GaN NWs, the FEM (introduced in section 2.4) as implemented in the commercial package MSC.Marc2008r1 is employed. Consequently, the simulations are performed within the framework of linear elasticity theory for which the components of the strain tensor are dimensionless [cf. section 2.2]. An important consequence of this fact is that the presented results can be scaled arbitrarily to smaller or larger dimensions as long as the strain relaxation is purely elastic. In other words, the strain field in the NW will be identical for all axial (In,Ga)N/GaN NW heterostructures with the same ratio of NW diameter and

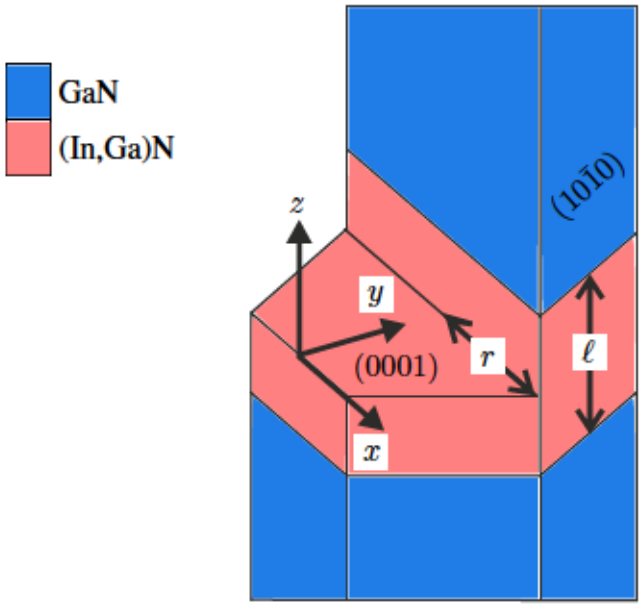

Figure 3.2 Sketch of a hexagonally-shaped GaN NW of radius r with an embedded axial (In,Ga)N segment of length ℓ. The z-axis is defined parallel to the [0001]-direction.

segment length. Furthermore, the simulations take into account the full elastic anisotropy of the hexagonal group-III nitrides. The elastic constants for GaN and InN are taken from Ref. [152], and the elastic constants for the ternary (In,Ga)N alloy are obtained by linear interpolation using Vegard's law [cf. Eq. 2.1.4]. The elastic constants serve as input for the FEM simulation. For $In_xGa_{1-x}N$ there exist 5 independent elastic constants which have to be inserted into the elasticity matrix according to Eq. 2.2.6. It is important to note that in MSC.Marc2008rl the entries for the elastic constants c_{44} and c_{66} have to be exchanged due to the used technical notation. The strain relaxation behavior originating from the lattice mismatch between GaN and $In_{0.3}Ga_{0.7}N$ is technically realized via an artificial thermal expansion of the mesh according to

$$\varepsilon_{ij} = \alpha_{ij}\Delta T\,, \tag{3.1.1}$$

where ε_{ij} is the strain component [cf. Eq 2.2.4], α_{ij} are the coefficients of thermal expansion and ΔT is the temperature difference. The coefficients of thermal expansion correspond to the lattice mismatch between a reference material, here GaN, and the strain inducing material, here $In_{0.3}Ga_{0.7}N$. Hence, the coefficients of thermal expansion are zero for GaN and $\alpha_{xx} = \alpha_{yy} = \alpha_{zz} = 0.03$ for $In_{0.3}Ga_{0.7}N$ corresponding to a lattice mismatch of 3%. The linear elastic analysis is conducted using the *iterative sparse* solver whereas the maximum number of iterations is set to 20000 and the tolerance to 10^{-9}. The result has to be interpreted by keeping in mind that only elastic deformations are considered. Moreover, material interfaces are coherently strained and abrupt with no structural roughening.

In all what follows, a hexagonally shaped, $\langle 0001\rangle$-oriented GaN NW is consid-

ered including an embedded $In_xGa_{1-x}N$ segment with $x = 0.3$ as schematically depicted in Fig. 3.2. For simplicity, the z-axis is defined parallel to the [0001]-direction of GaN. The alloy is treated as a perfectly homogeneous material, i. e., random compositional fluctuations in this material are ignored. For example, for (In,Ga)N compounds, In clustering and phase segregation [41, 42] are subject to research activities. Also one has to bear in mind that complex shapes of embedded (In,Ga)N segments have been observed and discussed [153]. For the sake of explicitness, but without loss of generality, the NW radius as defined in Fig. 3.2 is set to $r = 10$ nm. Energy balance considerations for an elastically isotropic material predict that the $In_{0.3}Ga_{0.7}N$ segment remains coherently strained for this radius regardless its length ℓ [62].

Experimental investigations were often focused on very short (In,Ga)N segments which shall be referred to as quantum disks (QDs) in the following with a thickness of typically not more than 2 to 5 nm [21, 154, 155]. For an $In_{0.3}Ga_{0.7}N$ QD with this thickness, the emission wavelength is expected to be between 600 and 700 nm, making these structures interesting for applications for red LEDs. Thicker QDs would be expected to emit in the infrared spectral range, but for the corresponding planar structures, strain-induced piezoelectric fields within the QDs would inhibit the emission altogether. For NWs, however, the elastic strain relieve at the NW sidewalls may greatly reduce the magnitude of these fields.

3.2 Geometry dependent strain analysis

For a systematic investigation of the evolution of the strain field within the NW, the segment length ℓ is varied from 2 to 40 nm while keeping the In content and NW radius constant. It is important to note, that this is equivalent to keeping the segment height fixed while successively changing the NW radius at constant In content. As mentioned before, the strain distribution in an axial NW with the same ℓ/r-ratio is identical within the framework of linear elasticity theory.

To begin with, the focus lies on the out-of-plane component of the elastic strain tensor, ε_{zz}, as defined by the relative lattice parameter difference with respect to the unstrained bulk material. For a pseudomorphically strained (In,Ga)N/GaN layered system, the (In,Ga)N layer is under biaxial compressive strain characterized by a positive value of ε_{zz} throughout the (In,Ga)N layer. Intuitively, one would expect a positive value for ε_{zz} for an equivalent layer sequence in a NW as well. Since strain can be elastically relieved at the NW surface, ε_{zz} will be decreased particularly close to the surface, and should eventually approach zero in the limit of very thin NWs except for the interfacial boundaries. However, the following study shows that the strain relaxation in axial (In,Ga)N/GaN NWs does not proceed in this simple monotonic fashion as intuitively expected.

In order to follow the evolution of the strain field with increasing ℓ/r-ratio, a map of ε_{zz} is calculated for different lengths of the embedded $In_{0.3}Ga_{0.7}N$ segment as shown in Fig. 3.3. The two-dimensional (2D) slice is taken in the x-z-plane [cf. Fig. 3.2] from corner to corner through the NW center. Moreover, the z-axis corresponds to a NW growth along the [0001]-direction. For the 2 nm

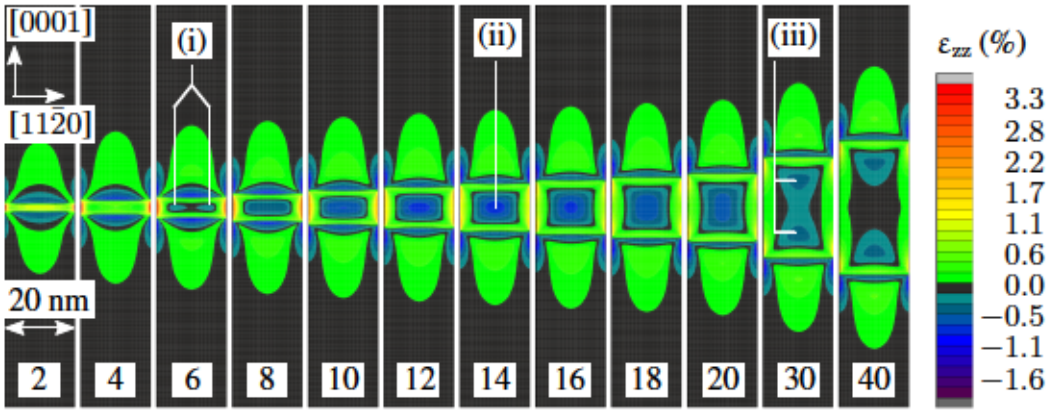

Figure 3.3 Map of the elastic strain component ε_{zz} for a vertical slice across the center of the NW and for different lengths ℓ of the embedded $In_{0.3}Ga_{0.7}N$ segment from 2 to 40 nm. Starting from a compressively strained $In_{0.3}Ga_{0.7}N$ QD with positive ε_{zz} at $\ell = 2$ nm, ε_{zz} gradually decreases and eventually turns negative in a torus-shaped region for the QD with $\ell \approxeq 6$ nm [(i)]. This region expands with increasing ℓ until ε_{zz} assumes a minimum value of about -0.8 % in the center of the $In_{0.3}Ga_{0.7}N$ segment with $\ell = 14$ nm [(ii)]. A further increase of ℓ results in complete elastic relaxation ($\varepsilon_{zz} \to 0$) in the middle part of the segment with $\ell =$ 40 nm [(iii)].

thick QD, a strain state almost similar to an equivalent planar system is established, i. e., the QD is under essentially uniform strain with $\varepsilon_{zz} > 0$ throughout its volume. Strain relaxation mainly occurs in the direct vicinity of the free sidewall surfaces and the $In_{0.3}Ga_{0.7}N$/GaN interfaces, manifesting itself in long-range distortions in the adjacent GaN segments which change their character from tensile ($\varepsilon_{zz} < 0$) to compressive ($\varepsilon_{zz} > 0$) with increasing distance from the QD. The latter feature already states an important difference to an equivalent planar system. Furthermore, ε_{zz} attains values of more than 3 % directly at the edges of the hexagonal $In_{0.3}Ga_{0.7}N$ QD.

For thicker QDs, this behavior changes profoundly, in that the relaxation affects progressively more of the volume of the $In_{0.3}Ga_{0.7}N$ QD itself. For $\ell =$ 6 nm [see panel (i) in Fig. 3.3], a part of the inner core of the QD exhibits the bulk lattice constant of $In_{0.3}Ga_{0.7}N$ with $\varepsilon_{zz} = 0$. Embedded into this region are two radially separated regions with a negative value of ε_{zz}. These regions represent a cut through a torus-shaped strain distribution with maximum compression.

When increasing ℓ, the spatially separated compressed regions extend toward the center of the segment and eventually merge. As a result, the entire inner core of the $In_{0.3}Ga_{0.7}N$ segment is under tensile strain with $\varepsilon_{zz} < 0$. The maximum magnitude of this tensile strain is reached for $\ell/r \approx 3/2$ [see panel (ii) of Fig. 3.3], for which ε_{zz} approaches a negative value as large as -0.8 %. The maximum values for ε_{zz} of about 2 % are again observed at the edges of the $In_{0.3}Ga_{0.7}N$ segment.

A further increase of the ℓ/r-ratio beyond the value of 3/2 reverses the continuous decrease of ε_{zz} in the center of the segment. However, the inner core of the $In_{0.3}Ga_{0.7}N$ segment persists to be under tensile strain until the ℓ/r-ratio attains values larger than 3 [see panel (iii) in Fig. 3.3]. In this case, the minimum in

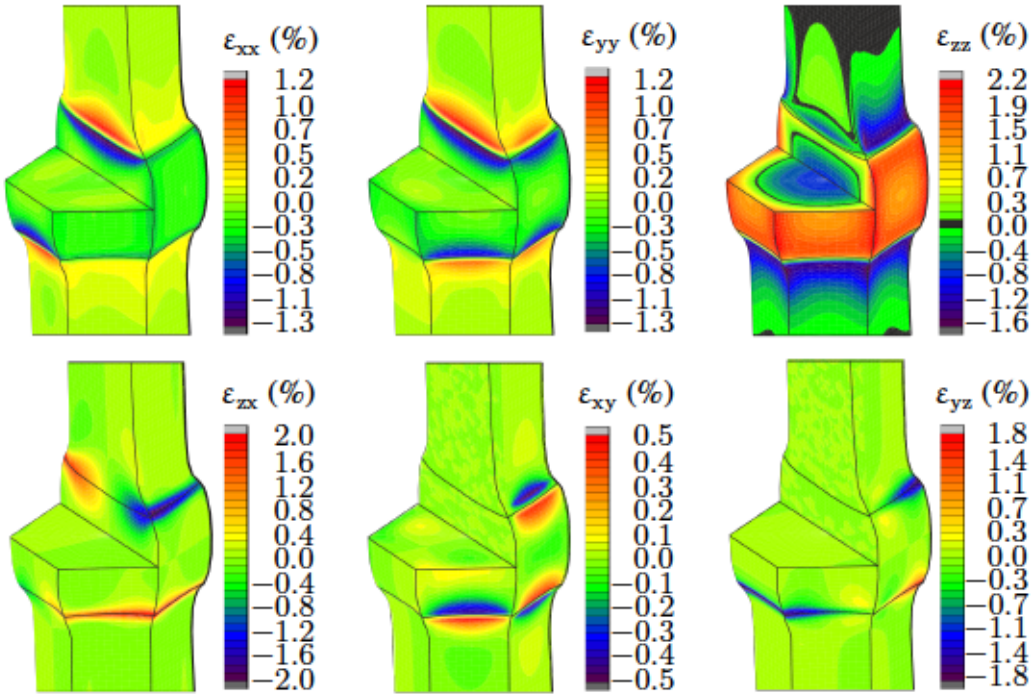

Figure 3.4 On and off-axis strain components for the $In_{0.3}Ga_{0.7}N$/GaN NW with $\ell/r = 1$. The in-plane normal components ε_{xx} and ε_{yy} suggest a nearly complete strain relaxation, but the out-of-plane normal component ε_{zz} is negative in the inner core of the segment. The strain release at the surface induces a deformation of the $In_{0.3}Ga_{0.7}N$ segment, enhanced here by a factor of 10 for better visibility. This deformation is accompanied by significant shear strain components with out-of-plane contribution, concentrated mainly at the $In_{0.3}Ga_{0.7}N$/GaN interfaces.

the center of the segment starts to divide into two separated regions with a negative value of ε_{zz} but now in axial direction. At the same time, the value of ε_{zz} in the center of the segment slowly approaches zero. Finally, a strain state akin to complete elastic relaxation is observed for the middle part of the 40 nm long $In_{0.3}Ga_{0.7}N$ segment. However, the strain field stays complicated at the interface to the adjacent GaN segments.

Note that the complete elastic relaxation observed for long segments is not to be confused with the vanishing ε_{zz}-value for $\ell/r = 3/2$ [cf. panel (i) of Fig. 3.3]. While the former effect is a simple manifestation of St. Venant's principle [156–158] the latter one is as unexpected as it is difficult to understand on an intuitive basis.

To shed light onto this anomaly in the dependence of the out-of-plane strain on the ℓ/r ratio, it is important to consider all components of the strain tensor, and in particular the shear strains. As a representative example, Fig. 3.4 shows these components for the $In_{0.3}Ga_{0.7}N$/GaN NW with $\ell/r = 1$, for which a significant portion of the $In_{0.3}Ga_{0.7}N$ segment exhibits a tensile out-of-plane strain [cf. Fig. 3.3]. Despite this fact, the in-plane normal components ε_{xx} and ε_{yy} are seen to be spatially uniform and small (-0.3 %) essentially within the entire $In_{0.3}Ga_{0.7}N$ segment. Deviations from this quasi-relaxed in-plane strain state are

observed only at the interfaces, where the adjacent materials experience a strong compressive and tensile strain to accommodate the lattice mismatch and to establish a commensurate boundary.

In contrast, the out-of-plane component ε_{zz} is negative in the central part of the segment and continuously increases towards both the free surface and the interfaces to the adjacent GaN segments. On each $\{10\bar{1}0\}$ facet of the segment surface, ε_{zz} is smallest at the center of the facet and increases towards the hexagonal edges as well as towards the interfaces with a maximum value of about 2 %. This variation of ε_{zz} is accompanied by a significant convex deformation of the shape of the segment at the free sidewalls. Moreover, at the interface to the GaN matrix the $In_{0.3}Ga_{0.7}N$ segment is deformed in a concave manner. In Fig. 3.4 the deformation of the NW is enhanced by a factor of 10 for better visibility.

This deformation of the $In_{0.3}Ga_{0.7}N$ segment necessitates non-zero shear strains. In fact, all three shear-strain components are significant, and particularly those with out-of-plane components (ε_{zx} and ε_{yz}), which reach magnitudes as large as 2 %. These shear components allow an almost complete in-plane relaxation of the $In_{0.3}Ga_{0.7}N$ segment via the convex deformation of the NW sidewalls inducing a volume change of 1:0.97 which deviates from that of an equivalent layered structure showing a volume change of 1:1. It is this deformation which results in an axial contraction, and is thus directly responsible for the negative out-of-plane strain observed in this study.

3.3 Accessibility in an x-ray diffraction experiment

To access the local strain state of a single NW experimentally is a challenging task. A particularly powerful technique to investigate the 3D strain distribution within single NWs is nanofocus x-ray diffraction as introduced in sections 2.5 to 2.9. This non-destructive technique combines a high angular resolution in reciprocal space with a sub-µm spatial resolution [35, 37, 47, 57, 58, 76]. To assess the feasibility to experimentally measure the strain distribution for single (In,Ga)N/GaN NWs, the impact of a strained (In,Ga)N segment in a GaN NW on the diffuse x-ray scattering pattern of the discussed NW heterostructure is simulated. Using the kinematic expression, Eq. 2.9.1, as introduced in section 2.9, the 2D intensity pattern around the Bragg reflection in reciprocal space is computed. The atom coordinates are interpolated using the displacement field $\mathbf{u}$ obtained from FEM giving the displacement of the atom positions $\mathbf{u}(\mathbf{r}_i)$. As an example, four simulated reciprocal space maps will be discussed, showing the diffusely scattered intensity around the symmetric GaN(0004) reflection. For the simulations, a spot size of $120 \times 120\,\mathrm{nm}^2$ is assumed and the strain fields are taken from the series of Fig. 3.3.

In Fig. 3.5(a), a bare GaN NW is considered yielding a peak at $q_z = 4.85\,\text{Å}^{-1}$ which is the expected position for bulk GaN. This peak is modulated by finite size oscillations due to the NW geometry. The pattern changes as soon as strain is introduced into the NW due to the presence of an $In_{0.3}Ga_{0.7}N$ segment. The reciprocal space map (RSM) shown in Fig. 3.5(b) for a 4 nm thick QD exhibits no

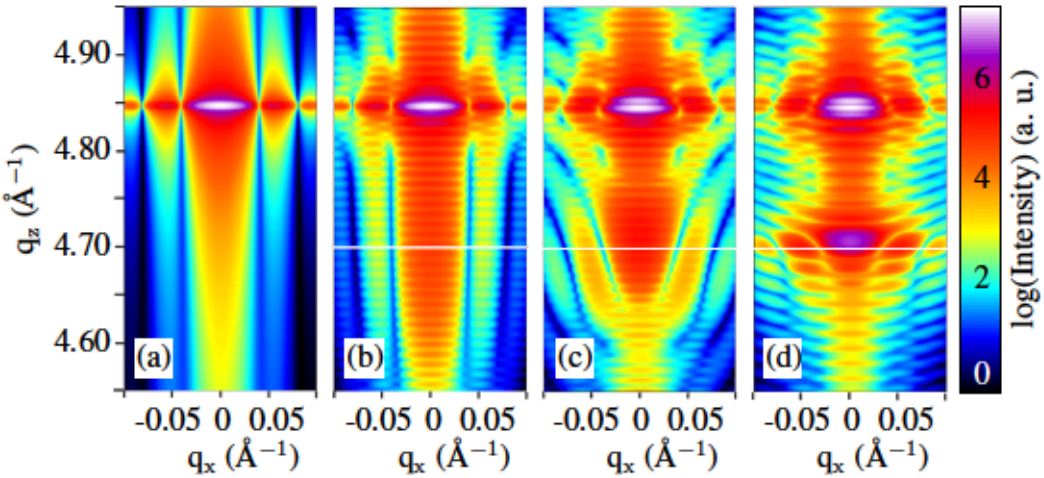

Figure 3.5 Simulation of the diffusely scattered intensity around the symmetric GaN(0004) reflection calculated in the frame of the kinematic scattering theory. Here, x points along the $[10\bar{1}0]$-direction such that along q_x the crystal truncation rod originating from a m-plane facet is visible. (a): Reciprocal space map for a bare GaN NW with radius $r = 10$ nm. (b), (c) and (d): Reciprocal space maps for GaN NWs with embedded (In,Ga)N segments of length $\ell = 4$ (b), 10 (c) and 40 nm (d). The white line indicates the expected peak position for relaxed $In_{0.3}Ga_{0.7}N$.

distinct peak related to $In_{0.3}Ga_{0.7}N$, but the phase shift induced by the QD results in pronounced interference fringes along q_z. As a guide to the eye, in Fig. 3.5(b) to (d) the white line indicates the peak position expected for relaxed $In_{0.3}Ga_{0.7}N$. For $\ell = 10$ nm, the FEM simulation predicts negative elastic strain within the QD volume, which in turn will shift the peak position of relaxed $In_{0.3}Ga_{0.7}N$ toward larger values of q_z as indeed seen in Fig. 3.5(c). Besides the change in the position of the Bragg peak, the diffuse part at $q_x \neq 0$ serves as a sensitive fingerprint of the established strain field within the NW. Due to the comparatively large volume of relaxed $In_{0.3}Ga_{0.7}N$, the RSM of the 40 nm long segment exhibits a clear peak with high intensity close to the position of relaxed $In_{0.3}Ga_{0.7}N$ as visible in Fig. 3.5(d). The complex strain field at the interfaces manifests itself by the strong modulations around this peak. Based on the simulated RSMs, it is obvious that an $In_{0.3}Ga_{0.7}N$ segment embedded in a GaN NW has a significant, experimentally accessible impact on the diffraction pattern, and nanofocus x-ray diffraction experiments are thus suitable to probe the local strain distribution in these NW heterostructures.

3.4 Concluding remarks

The results presented for ⟨0001⟩-oriented (In,Ga)N/GaN NWs are also valid for other axial semiconductor NW heterostructures, including all ⟨0001⟩-oriented wurtzite NWs, but also ⟨111⟩-oriented NWs composed of materials with diamond and zincblende structure such as Ge/Si [55, 159, 160], Si/GaP [22], InAs/InP

[161, 162] and CdTe/ZnTe [163]. Interestingly, if the embedded segment comprises a smaller lattice parameter than the surrounding material, a positive ε_{zz}-value is observed if the ratio of NW radius and segment length approaches unity. For all these materials systems, the strain anomaly investigated in the present work is not only of academic interest, but has potentially far-reaching consequences for their application in electronic and optoelectronic devices. In fact, the presented study shows that the length-to-radius ratio can be used to engineer the strain field and in particular to tune the out-of-plane strain component from compressive to tensile. This new degree of freedom can be used to manipulate the band gap, the effective mass, and the magnitude and direction of the piezoelectric fields in the strained insertion.

4 Investigation of the piezoelectric potential in axial (In,Ga)N/GaN nanowires

Amongst challenges like, e. g., crystal quality and phase segregation, an important issue of III-nitride compound semiconductors are strong internal electric fields. In addition to the inherent spontaneous polarization, the piezoelectric polarization is added when it comes to III-V heterostructures like (In,Ga)N/GaN as described in section 2.3. For example, a planar (Al,Ga)N layer grown on [0001]-oriented GaN is tensile strained such that the vectors $\mathbf{P}_{\mathrm{sp}}$ and $\mathbf{P}_{\mathrm{pz}}$ point in the same direction. In contrast, an (In,Ga)N layer grown on [0001]-oriented GaN is under compressive strain and $\mathbf{P}_{\mathrm{sp}}$ and $\mathbf{P}_{\mathrm{pz}}$ point in opposite directions [71]. However, due to the larger lattice mismatch between GaN and InN [cf. section 2.1], here, $\mathbf{P}_{\mathrm{pz}}$ is significantly larger than in (Al,Ga)N/GaN heterostructures.

Strong internal electric fields cause a modulation of the band structure and, thereby, induce a spatial separation of electrons and holes yielding a decreased overlap of their respective wavefunctions. The consequences are low recombination rates and a weak optoelectronic performance. Hence, it is desirable to manipulate the internal electric field and to either decrease its magnitude or to even achieve its suppression.

As becomes clear from Eq. 2.3.2, the piezoelectric polarization can be influenced by engineering the strain distribution in a heterostructure. For example, considering an (In,Ga)N layer embedded into a planar [0001]-oriented GaN matrix, the polarization points along this polar axis and the piezoelectric polarization is influenced by the normal components of the strain tensor, only. These can be modified by changing either the (In,Ga)N layer thickness or the incorporated In content. If the total polarization is intended to be suppressed, $\mathbf{P}_{\mathrm{tot}} = 0$, the spontaneous polarization has to be balanced by the piezoelectric polarization

$$P_{\mathrm{sp},z} = P_{\mathrm{pz},z} = e_{31}(\varepsilon_1 + \varepsilon_2) + e_{33}\varepsilon_3 \,. \tag{4.0.1}$$

In a planar system the parameter space for changing the In content and the layer thickness is limited with respect to the demand of high crystal quality, because, as mentioned at the end of section 2.1, after a critical layer thickness plastic relaxation occurs.

In the following, the results obtained in chapter 3 are used to investigate the electric potential in axial (In,Ga)N/GaN NWs. A particular interest will be put on the question whether the possibility of tuning the character of ε_{zz} from tensile to compressive can be used to minimize the electric potential in axial (In,Ga)N/GaN NWs. Additionally, the consequences for the optical performance are discussed. Parts of this chapter have been published in Ref. [164].

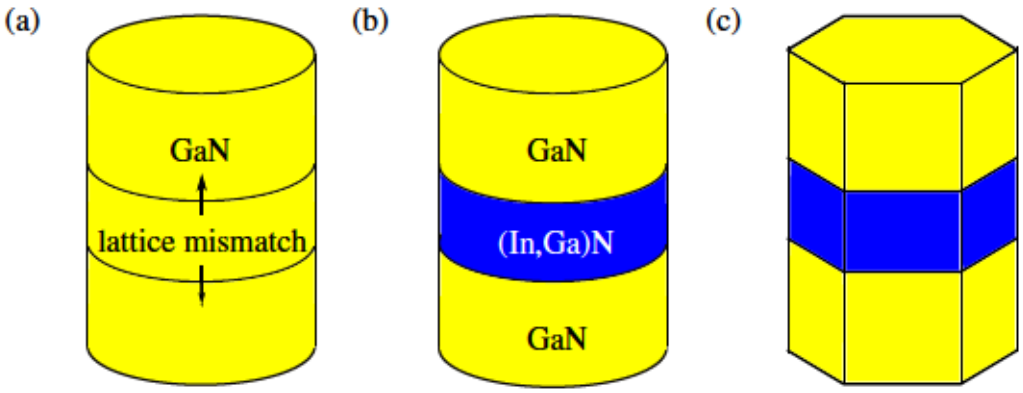

Figure 4.1 Sketch of the three investigated models. In (a) the material constants for GaN are assumed to be valid throughout the nanowire and the presence of the (In,Ga)N segment is solely implemented via lattice mismatch with the surrounding GaN matrix. In (b) the cylindrical shape of the nanowire is maintained, however, the material constants for GaN and (In,Ga)N are applied. The most realistic scenario is described by model (c). Here, next to a spatial variation of the material properties, the actual hexagonal shape of the NW is taken into account.

4.1 The three investigated models

As discussed at the end of section 2.1, NWs are expected to be able to effectively release strain by the deformation of their outer surface and, thereby, can facilitate the incorporation of higher amounts of In without resulting in plastic deformation. Moreover, as presented in chapter 3, by varying either NW radius or the length of the (In,Ga)N segment at constant In content, the strain state of ε_{zz} can be tuned from tensile to compressive which offers a new degree of freedom for strain engineering. However, the shear strains play a crucial role in the process of strain relaxation which complicates the picture as the strain distribution is highly inhomogeneous. Next to the beneficial elastic relaxation properties, a reduction of the built-in piezoelectric potential and, thus, the QCSE [8, 129, 165] is expected. In fact, in literature even evidence for a vanishing QCSE is reported [9, 166–168]. Due to spatial confinement and negligible surface potentials [169] very thin NWs are of particular interest and have recently been fabricated by either direct growth [170] or post-growth thermal decomposition [171].

In the presented study, an axial [0001]-oriented (In,Ga)N/GaN NW model with a diameter of only 15 nm is considered. The thickness of the embedded $In_xGa_{1-x}N$ disk will be denoted by t and x is the In content. In Fig. 4.1, the three models subject to the following discussion are sketched. In Fig. 4.1(a), the simplifications necessary to compute the elastic strain distribution and electric potential analytically are applied to the FEM model. These comprise a cylindrical shape and the assumption of uniform elastic, piezoelectric and dielectric constants throughout the whole axial NW heterostructure. In general, the material properties of GaN are chosen and the (In,Ga)N segment is modeled by implementing a lattice mismatch with respect to GaN. Based on these simplifications, exact solutions of both the elastic problem and the Poisson equation

[cf. Eq. 2.3.8] can be achieved as presented in Refs. [129] and [172] which can be compared to the respective results obtained via the FEM. The impact of the first simplification, namely spatially constant material properties throughout the NW, can be evaluated by comparing model (a) to model (b) in which the cylindrical shape is maintained, however, the elastic, piezoelectric and dielectric constants are chosen according to the materials GaN and (In,Ga)N. The most realistic model is assumed in Fig. 4.1(c). Here, the actual hexagonal shape of the NWs is taken into account additionally to a spatial variation of the material constants.

4.2 Piezoelectric analysis with MSC.Marc2008rl

Due to the fact that the piezoelectric analysis performed with the commercial software package MSC.Marc2008rl is not very well documented and involves some important technical insights, the implementation will be elaborated in the following using the example of an axial (In,Ga)N/GaN NW as introduced in section 4.1. In MSC.Marc2008rl the piezoelectric analysis is implemented such that nodal displacements and electric potential are solved simultaneously in a fully coupled way. The constitutive equations for the stress-based piezoelectric coupling are

$$\boldsymbol{\sigma} = \mathrm{C} \cdot \boldsymbol{\varepsilon} + \mathrm{e} \cdot \mathrm{E}\,, \tag{4.2.1}$$

for the mechanical behavior whereas $\boldsymbol{\sigma} = \mathrm{C} \cdot \boldsymbol{\varepsilon}$ is Hooke's law [cf. Eq. 2.2.5], e is the stress based piezoelectric coupling matrix [cf. Fig. 2.3.2] and E is the electric field vector, and

$$\mathrm{D} = \mathrm{e} \cdot \boldsymbol{\varepsilon} + \boldsymbol{\kappa} \cdot \mathrm{E}\,, \tag{4.2.2}$$

for the electrostatic behavior, where D is the electric displacement vector and $\boldsymbol{\kappa}$ the permittivity. As introduced for a purely mechanical problem in section 2.4, the piezoelectric analysis within MSC.Marc2008rl is formulated based on the displacement method, too. Consequently, Eqs. 4.2.1 and 4.2.2 are formulated in integral form and virtual displacements, strains and electrical potentials are introduced. Then the global equilibrium equation has to be rewritten as the sum of equilibrium equations of each element and for the assemblage to a linear equation system, the displacements, electrical potentials and strains have to be approximated by their nodal counterparts. A deeper insight about the technical background of the implementation of the piezoelectric analysis in MSC.Marc2008rl can be found in Ref. [73]. The reader has to be aware of the fact that the following outline will be specifically designed for implementing a piezoelectric analysis in MSC.Marc2008rl and, consequently, the language used in the software will be applied. Terms which refer to the implementation of the piezoelectric analysis within MSC.Marc2008rl will be highlighted in italic characters.

For a 3D model such as the axial NWs introduced section 4.1, the geomet-

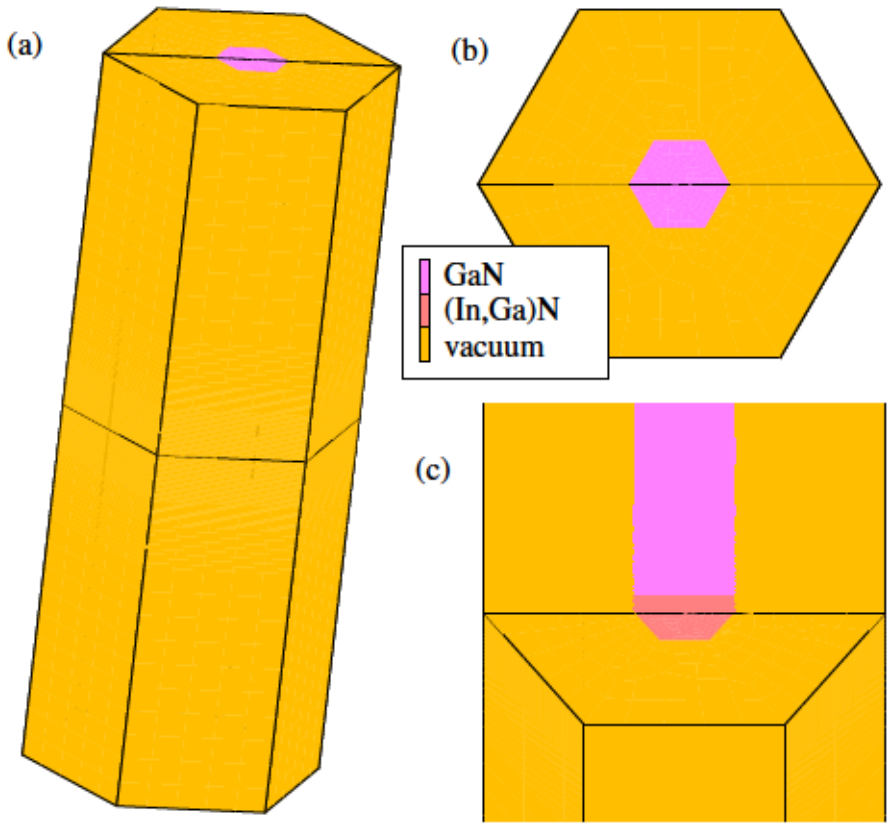

Figure 4.2 In (a) the outer surface of the full finite element method model is shown. The axial (In,Ga)N/GaN rod visible in pink is surrounded by vacuum colored in yellow. In (b) a top view image is shown. Importantly, the lateral width of the vacuum has to be at least twice the rod diameter. In (c) a perspective view inside the model is shown. Here, a part of the (In,Ga)N segment is visible which is colored in orange. The density of elements inside the rod is significantly higher compared to the vacuum.

rical entities for the subdivision of the full object have to be hexahedra. In the graphical interface MSC.Mentat this corresponds to choosing a 3D piezoelectric element type with *ID class: hex8* and *ID type: 163*. The model of the axial (In,Ga)N/GaN NW comprises three different material types as sketched in Fig. 4.2: The (In,Ga)N segment which is colored orange in (c), the GaN matrix shown in pink and the surrounding vacuum colored in yellow. In between the outer surface of the NW and the extent of the vacuum has to be at least two times the NW diameter in order ensure that the electric field decays sufficiently inside the vacuum. Moreover, the distance along the z-direction between (In,Ga)N segment and the bottom and top facet of the NW has to be large enough such that the piezoelectric field induced by the (In,Ga)N segment decays to a constant value. The lateral density of the finite elements inside the rod is significantly higher compared to the vacuum as visible, e. g., in Fig. 4.2(a) and (b). Additionally, along the vertical direction the subdivision of elements in the (In,Ga)N segment as well as in its vicinity is drastically increased in Fig. 4.2(a) and (c). This is necessary to cover the full implication of the complex strain distribution in this

region.

The material properties have to be assigned to each part of the model and for all of them the *anisotropic* mechanical material type as well as the non-mechanical material types *electrostatic* and *piezoelectric* have to be activated. For the vacuum the elasticity matrix as well as the piezoelectric coupling matrix are left blank. However, the electrostatic properties are chosen as being *isotropic* and the value of the vacuum permittivity has to be entered. For GaN and $In_xGa_{1-x}N$ the elastic constants have to be entered into the elasticity matrix which is given in Voigt notation [cf. Tab. 2.1] and, as mentioned in section 3.1, the entries for the elastic constants c_{44} and c_{66} have to be exchanged. The elastic constants for $In_xGa_{1-x}N$ are obtained using Vegard's law given by Eq. 2.1.4 whereas the elastic constants of GaN and InN in the present study are taken from Ref. [173]. The process of elastic strain relaxation is implemented via a virtual thermal expansion of the FEM grid based on Eq. 3.1.1. Furthermore, due to the lattice mismatch of about 10 % between GaN and InN, the *anisotropic thermal expansion properties* have to be entered for example as $\alpha_{ij} = 0$ for GaN which serves as the reference material and, e. g., $\alpha_{11} = \alpha_{22} = \alpha_{33} = 0.04$ for $In_{0.4}Ga_{0.6}N$ corresponding to an In content of 40 % and a lattice mismatch of 4 %.

The piezoelectric properties are described by the piezoelectric coupling matrix. Here, the *stress-based* option has to be selected and the components of the third-rank tensor *E[i,j,k]* are mapped to matrix components using Tab. 2.1 with [i,j,k]→[α,k]. As introduced in section 2.3, for the wurtzite crystal there exist five non-vanishing components in the piezoelectric coupling matrix whereas there are only three different piezoelectric constants as shown in Eq. 2.3.4. Translated to the graphical interface MSC.Mentat this coupling matrices for GaN and $In_{0.4}Ga_{0.6}N$ are shown as screen-shots in Figs. 4.3(a) and (b), respectively. Here, the piezoelectric constants are taken from Ref. [173] and entered in units of 100 nm which has been defined to be equal to one FEM unit. The components for $In_{0.4}Ga_{0.6}N$ are interpolated linearly. Moreover, as suggested in Ref. [174] it is assumed that $e_{15} = e_{31}$ and, importantly, owing to the fact that in MSC.Marc2008rl the shear components of the elasticity tensor are defined via $\gamma_\alpha = 2\varepsilon_\alpha$ with $\alpha \in \{4, 5, 6\}$ [cf. section 2.2], the component e_{15} has to be divided by two. To finalize the material properties necessary for the piezoelectric analysis the electrostatic properties for GaN and $In_{0.4}Ga_{0.6}N$ have to be specified. As for the vacuum, the *isotropic* type is chosen and the values of the permittivity for GaN and InN are again taken from Ref. [173] and the permittivity for $In_{0.4}Ga_{0.6}N$ is interpolated linearly.

A crucial step for the piezoelectric analysis with MSC.Marc2008rl is to impose the right boundary conditions which are all related to the *electrostatic* boundary condition class. The employed boundary conditions are visualized in Fig. 4.4. In Figs. 4.4(a) and (b), a *fixed potential* is implemented in the way that the nodal coordinates which lie on the outer surface of the vacuum are set to zero. This guarantees that the electric potential induced by the heterostructure NW interacts with the vacuum and decays to zero with increasing distance from the NW itself. This boundary condition can be interpreted as a radial constraint to the

(a)

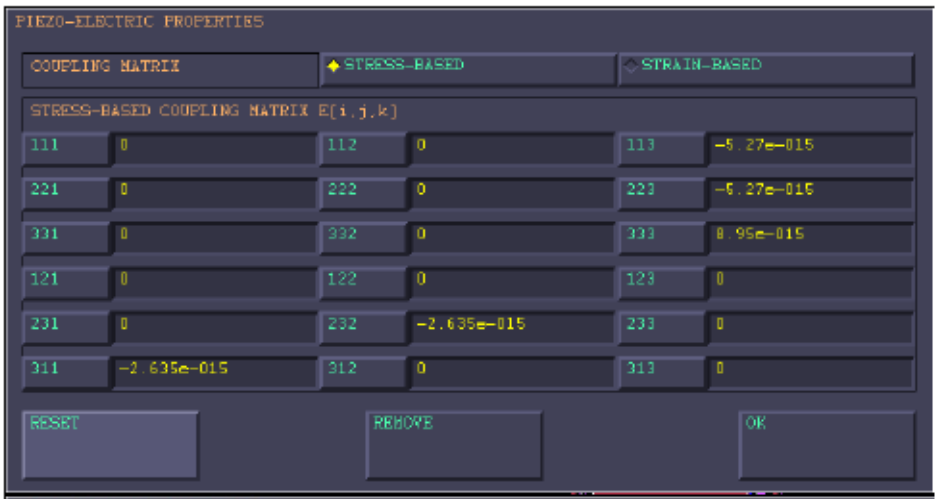

(b)

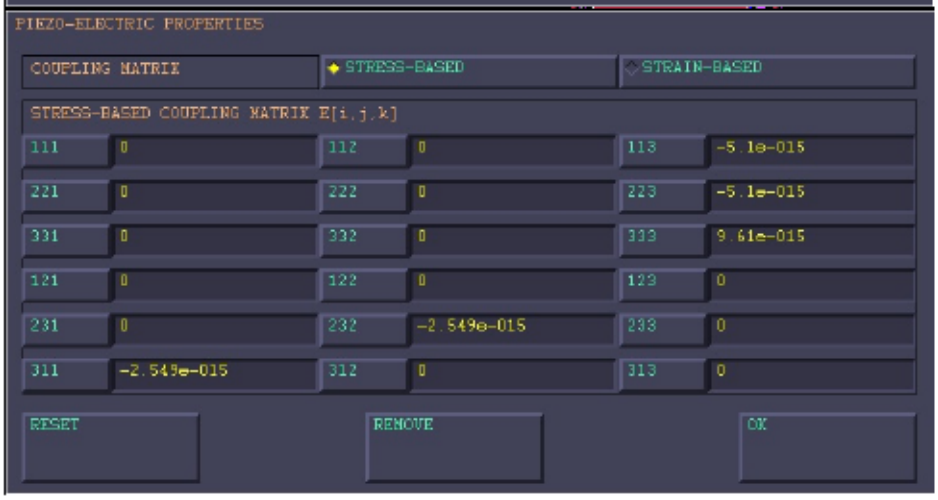

Figure 4.3 In (a) the piezoelectric coupling matrix as implemented in the graphical interface MSC.Mentat is shown for GaN. In (b) the respective piezoelectric coupling matrix for $In_{0.4}Ga_{0.6}N$ whereas the piezoelectric constants are interpolated linearly. Importantly, the *stress-based* coupling matrix has to be used.

electric potential inherent to the NW. In Figs. 4.4(c) and (d) an axial constraint is introduced. As discussed earlier an important property of III-nitride semiconductors is an inherent electric potential originating from a slight deviation from the perfect wurtzite crystal structure. As a consequence atomic dipoles form along the [0001]-direction giving rise to the macroscopic spontaneous polarization which in the presented model points along the vertical direction. The electric potential caused by the spontaneous polarization is implemented into the FEM model via *face charges*. These are placed on the bottom and top facets of the (In,Ga)N segment as displayed in Figs. 4.4(c) and (d), respectively. According to Ref. [173], the spontaneous polarizations are $P_{sp}(GaN)$ = -0.034 C/m^2 and $P_{sp}(InN)$ =-0.042 C/m^2 which are used to obtain the one for the $In_xGa_{1-x}N$ disk via linear interpolation given by $P_{sp}(In_xGa_{1-x}N) = x \cdot P_{sp}(InN) + (1\text{-}x)P_{sp}(GaN)$. For example, assuming an In content of 40 %, the difference $P_{sp}(In_{0.4}Ga_{0.6}N) - P_{sp}(GaN) = 0.0032$ C/m^2 serves as input for the face charge

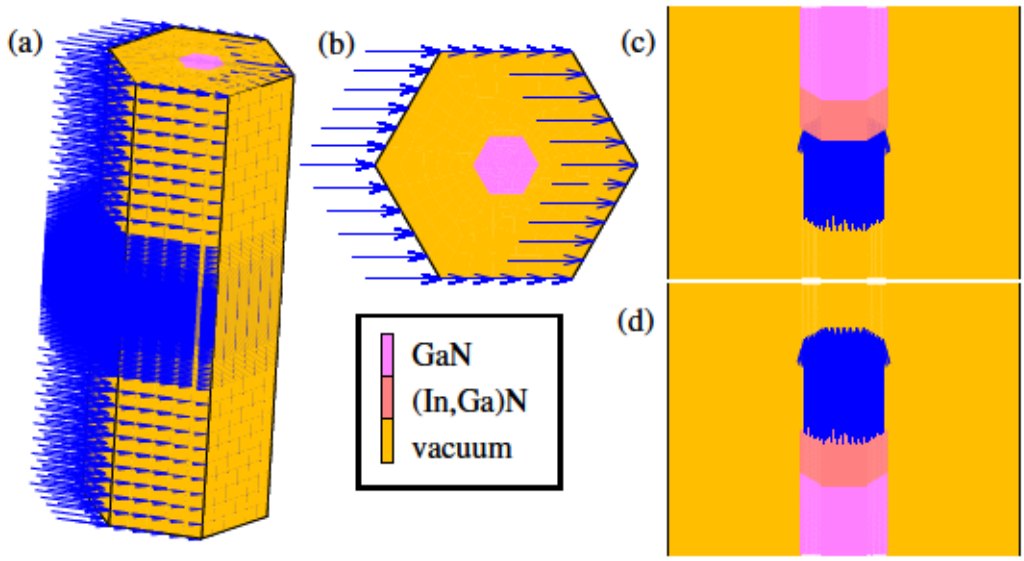

Figure 4.4 The boundary conditions applied to the piezoelectric analysis are visualized by blue arrows. In (a) and (b) nodal boundary conditions are employed to all nodes on the outer surface of vacuum. Here, the electric potential is set to zero. In (c) and (d) face charges are placed on the top and bottom interfaces between (In,Ga)N segment and GaN matrix. This mimics the presence of the spontaneous polarization. For a better visibility the GaN matrix below (c) and above (d) the (In,Ga)N segment are not displayed.

boundary condition. On the top interface a face charge of -0.0032 C/m^2 is placed and on the bottom interface a face charge of +0.0032 C/m^2. Eventually, this induces an electrostatic field originating from the spontaneous polarization. In Figs. 4.4(a) to (d), the boundary conditions are visualized by blue arrows. In (a) and (b) the boundary condition is applied to *nodes* and in cases (c) and (d) to *faces*. Consequently, the arrows point on nodes in the former case and on element faces in the latter.

As becomes clear from Eqs. 4.2.1 and 4.2.2, the strain is not only computed on the basis of Hooke's law but is modified by the presence of an internal electric field which alters the strain, too. An important consequence of the coupled solution of nodal displacements and electric potential is that the resulting strain distribution is slightly different to the one obtained within a purely elastic analysis which has been applied for computing the strain fields presented in chapter 3. Although the coupled solution of strain and electric potential seems to be the more realistic scenario a separate simulation of both quantities is pursued. This is due to the fact, that beforehand the FEM results of model (a) are compared to analytic calculations of strains and electric potential according to Refs. [129] and [172]. For the sake of comparability the simulations of the more complex models (b) and (c) are performed in the same manner. Consequently, it is possible to analyze the impact of the simplifications necessary to compute strains and electric potential analytically which will be discussed in the following section.

For solving the linear equation system the *piezoelectric analysis class* is selected. In the menu for *piezoelectric analysis options* the *advanced options* are selected as the *assumed strain*. Finally, the *multifrontal sparse* solver is chosen

which is an iterative solver based on the decomposition of the stiffness matrix.

4.3 Dependence of the electric potential on the (In,Ga)N segment dimension

To begin with, the strain distribution of an axial $In_xGa_{1-x}N$ segment with x = 0.4 embedded into a GaN NW with hexagonal cross-section as sketched in Fig. 4.1(c) shall be discussed. In Fig. 4.5, 2D vertical slices through the NW center from corner to corner are shown in the vicinity of the (In,Ga)N segment. In the top panel, the evolution of the in-plane strain distribution, $\varepsilon_{xx} + \varepsilon_{yy}$, and in the bottom panel the vertical normal component, ε_{zz}, are shown for an increasing disk thickness t from 0.5 to 6.5 nm. For small thicknesses the elastic relaxation occurs mainly at the outer side-facets and the center of the disk is subject to a strain distribution that is very similar to the one of an equivalent planar system. Here, the in-plane strain components show negative values corresponding to compressive strain and ε_{zz} is positive at all positions within the disk. However, the picture changes with increasing disk thickness. As expected from the study presented in chapter 3, a significant negative ε_{zz} component is observed while the ratio of NW radius and disk thickness approaches unity. Moreover, at the outer surface of the disk large positive ε_{zz} induce a concave deformation of the NW shape in the vicinity of the (In,Ga)N disk. At the same time the in-plane strain loses its compressive character and tends towards tensile strain. In all cases, however, the lattice mismatch between $In_xGa_{1-x}N$ and GaN induces significant strains at the interfaces which are expected to modify the polarization potentials and, thus, the electronic properties of the NW. It is important to note that the strain profiles simulated for models (a) and (b) [cf. Fig. 4.1] are comparable to the ones presented in Fig. 4.5 except for slightly larger local strains occurring in the corners of the hexagonal NWs in contrast to those seen at the side-facets.

In order to compare the electric potentials inherent to the three models (a) to (c) presented in Fig. 4.1, line profiles are extracted along the central axis vertically through the NW center at r = 0 as well as along a parallel line at the NW surface at r = R. The results are shown in Figs. 4.6(a) and (b), respectively, whereas the underlying models comprise a 4.5 nm thick $In_{0.4}Ga_{0.6}N$ disk embedded into a GaN NW with a diameter of 15 nm. A first observation is that all three models show qualitatively the same trends with deviations occurring mainly outside the $In_xGa_{1-x}N$ disk near the interfaces. In particular, a discrepancy between model (a) and models (b) and (c) is apparent. These deviations are a result of the fact that for this approach, the elastic, piezoelectric, and dielectric constants throughout the whole NW are assumed to be identical to those of GaN and the presence of the (In,Ga)N disk is solely mediated by the implementation of a lattice mismatch with the surrounding GaN matrix. In fact, the impact of using spatially non-varying material constants as in model (a) becomes increasingly inaccurate with increasing In content. However, the polarization potentials for models (b) and (c), where spatially varying material parameters are implemented, are in very good agreement. Consequently, the simplification of a cylindrical shape in con-

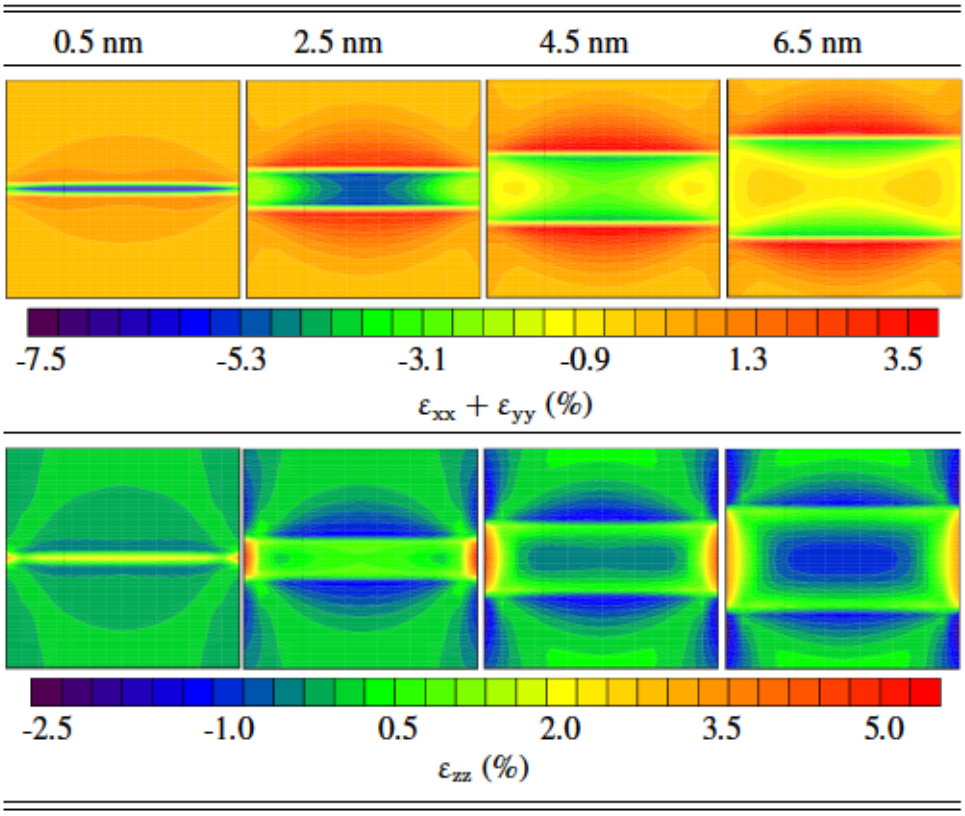

Figure 4.5 Cross-section of in-plane (top) and out-of-plane (bottom) elastic strain components for different thicknesses t of an $In_{0.4}Ga_{0.6}N$ disk embedded into a hexagonal GaN NW as sketched in Fig. 4.1. For thin disks the strain distribution is similar to an equivalent planar system, however, with increasing disk thickness large negative ε_{zz}-values are observed in the center of the disk which stands in stark contrast to planar systems where ε_{zz} is positive everywhere in the embedded layer.

trast to the actual hexagonal cross-section of the NWs appears to have only a minor influence on the line profiles. For the sake of completeness it is worth mentioning that the extrema of the polarization potential along an axis parallel to the NW growth direction (r = R) are slightly larger near the corners as compared to the ones near the center of a side-facet. This allows to conclude that concerning the simplifications necessary for an analytic treatment of the problem the impact of the cylindrical shape is minor compared to the use of spatially independent elastic constants which are largely responsible for the differences in the electric potential outside the active layer.

In Fig. 4.7, the normalized global maximum value of the polarization potential, $\max(V_p)/x$, is shown as a function of the QW thickness t which increases from 0.5 to 7 nm. The polarization potential is simulated for a hexagonal NW with a diameter of 15 nm corresponding to model (c) in Fig. 4.1. The evolution of $\max(V_p)/x$ is shown for an In content x of 20, 40 and 60 %, whereas the respective curves are normalized with the assumed In content. By that it becomes obvious that the absolute maximum of the polarization potential scales almost

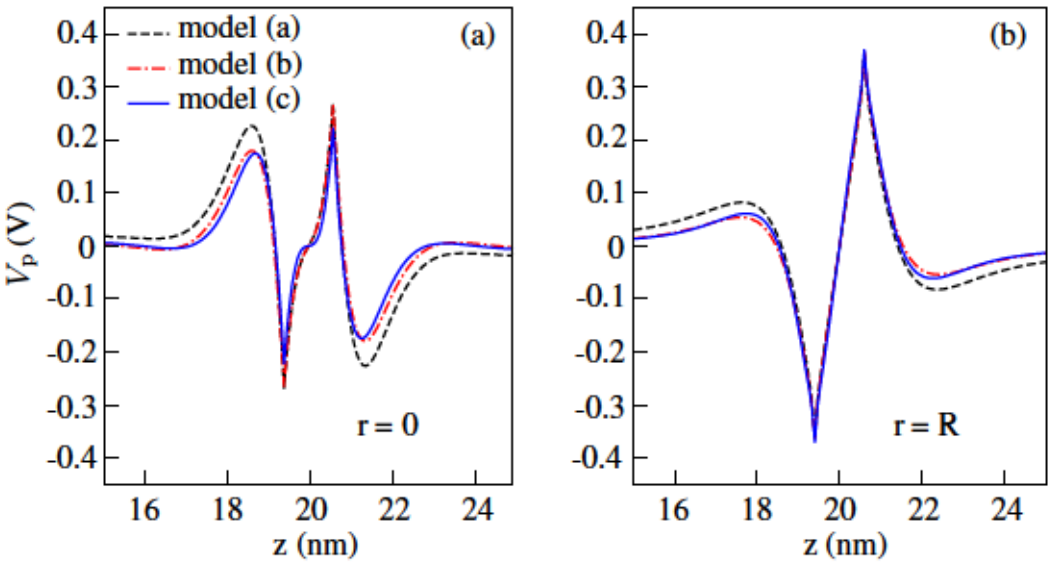

Figure 4.6 Line profiles of the electric potential in an axial $In_{0.4}Ga_{0.6}N$/GaN nanowire heterostructure with a diameter of 15 nm and a thickness of the $In_{0.4}Ga_{0.6}N$ disk of 4.5 nm. The underlying models (a) to (c) are visualized in Fig. 4.1. The line profiles in (a) are taken along the central axis of the nanowire at r = 0 and in (b) at the surface for the cylindrical models (a) and (b) or at the edge of the hexagonal cross-section of model (c) of the nanowire at r = R.

linearly with the In content of the $In_xGa_{1-x}N$ disk and only small modifications of the curve are seen for different In contents. In fact, in model (a) which corresponds to the analytic approach, the curves for different In contents are completely identical as the polarization potential scales strictly linearly with the In content. Moreover, only small deviations are observed for the curves shown in Fig. 4.7 when considering models (a) or (b) in comparison to model (c).

For an (In,Ga)N layer embedded into a planar GaN matrix a linear increase of the polarization potential is expected with increasing thickness of the layer the width. However, as can be seen in Fig. 4.7, for the investigated NW model a linear increase is observed only up to a thickness of about 2 nm and at a thickness of about 4.5 nm $\max(V_p)$ reaches its maximum after which a decrease is observed. This behavior translates into a limitation of the range of accessible electron-hole transition energies, as will be discussed in the section 4.4. At selected thicknesses the electric potential simulated using the FEM is shown in the insets in Fig. 4.7. The 2D slices taken vertically through the NW from corner to corner show a region in the vicinity of the QDs for the case of 40 % In. Apparently, for thin disks the electric potential has its maximum at the central axis of the NW, however, with increasing disk thickness the maximum shifts to the side-facets for thick disks.

This behavior is contemplated more closely in a quantitative manner in Figs. 4.8 (a) and (b). In Fig. 4.8(a) the maximum value of the polarization potential, $\max(V_p)$ is shown along the vertical axis of the NW at r = 0 (solid lines) as

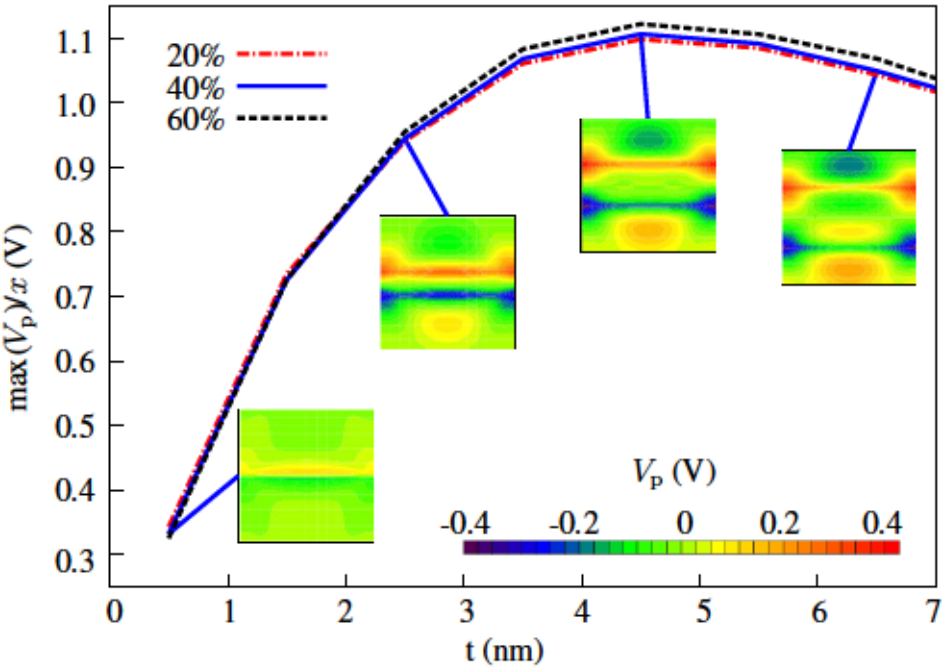

Figure 4.7 Overall maximum of the polarization potential divided by the respective In content as a function of the disk thickness t. On the basis of model (c) in Fig. 4.1 max(V_p) was extracted for In contents of 20, 40, and 60 %. The insets show a side-view of the polarization potential for selected thicknesses for an In content of 40 %.

well as along a parallel line at the side-facet at r = R (dash-dotted lines) as a function of the disk thickness t. The color coding corresponds to three different In contents of 20, 40 and 60 %. For all In contents the largest maximum value of max(V_p) can be found at a thickness of approximately 2.5 nm followed by a decrease of max(V_p) to a minimum value at 4.5 (x = 20 %), 5.5 (x = 40 %), and 6.5 nm (x = 60 %). After this point, the maximum of the polarization potential along the central axis of the NW increases again due to the spontaneous polarization. At the NW side-facet, the maximum of the electric potential has its largest value for disk thicknesses of 4.5 nm.

Figure 4.8(b) shows the ratio ξ=max[V_P(r = 0)]/max[V_P(r = R)] between the maximum potential along the central axis and the one along a parallel axis at the side-facets as a function of the disk thickness t. Until a thickness of about 2 nm the maximum value along the central axis is larger compared to the one at the side-facet. After this point this relationship is reversed. Eventually, above a thickness of about 2 nm, the extrema of the potential are located increasingly closer to the side-facets rather than at the central axis of the NW. Interestingly, the curves overlap for all three In contents, however, above a thickness of 4.5 nm a splitting of ξ is observed. This splitting owes to the fact that the minima of max(V_p) along the central NW axis (r = 0) as shown in Fig. 4.8(a) occur at different thicknesses for the In contents considered.

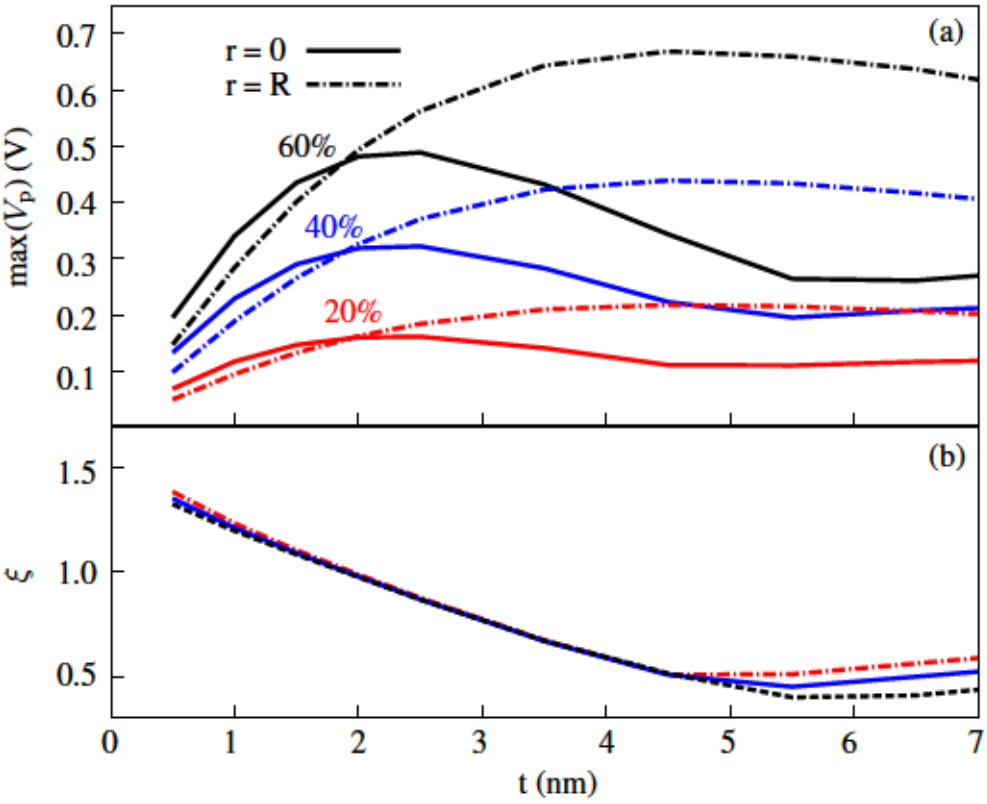

Figure 4.8 In (a) the maximum of the polarization potential along the central axis of the nanowire (solid) and along a parallel line at the side-facet (r = R, dashed-dotted) is shown as a function of the disk thickness *t*. The curves were simulated for model (c) in Fig. 4.1 and In contents of 20 (red), 40 (blue), and 60 % (black) were assumed. In (b) the ratio between the local maxima of the polarization potential along central axis at r = 0 and along the side-facets at r = R of the nanowire are shown as a function of the disk thickness *t*.

4.4 Consequences for the optical performance

The elastic strain components and the electric potential can serve as input for subsequent calculations of the electron and hole single particle wavefunctions and binding energies using an eight-band $\mathbf{k} \cdot \mathbf{p}$ model[1] for wurtzite crystals as described in Ref. [164] and references therein. Based on these simulations, conclusions about the impact of the above discussed dependence of the electric potential on the NW geometry can be drawn with respect to the resulting electronic properties which will be subject to the following discussion.

Figure 4.9 shows the energy difference between the electron and hole ground states $\Psi_{el,0}$ and $\Psi_{ho,0}$ as a function of the disk thickness. The simulations include the elastic properties and electric potential inherent to model (c) in Fig. 4.1, however, the difference if the same plot would be generated for model (a) is minor. The electron-hole ground state transition energy is computed for different In contents in steps of 20% In in the $In_xGa_{1-x}N$ disk from 20 up to 100 % In. The

[1] All presented $\mathbf{k} \cdot \mathbf{p}$ simulations are performed by Dr. O. Marquardt (Paul-Drude-Institut Berlin).

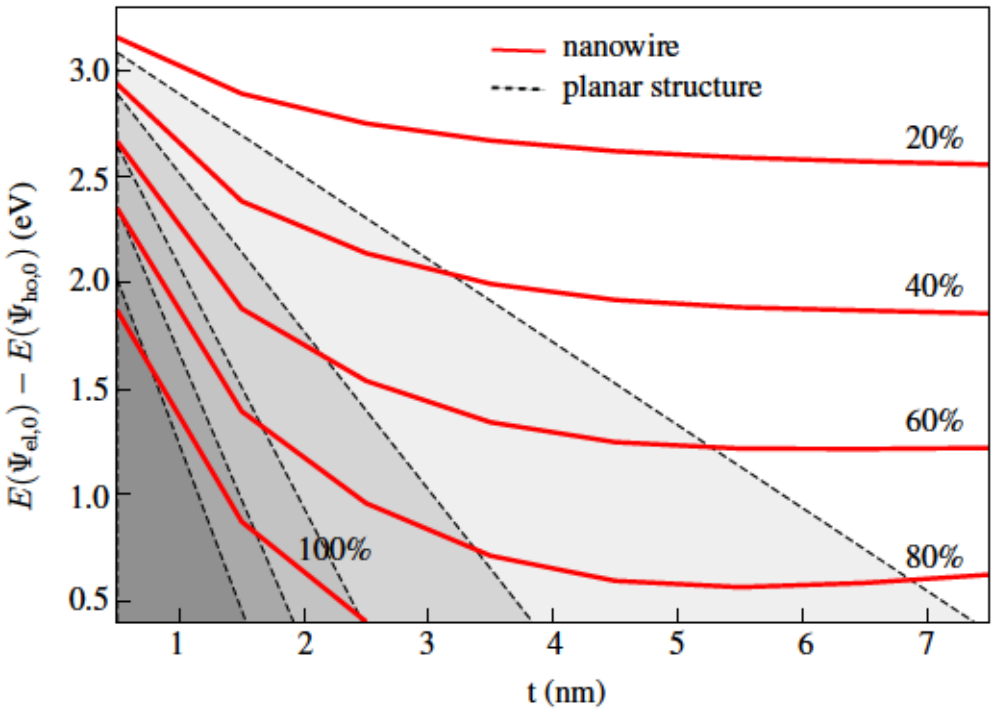

Figure 4.9 Electron-hole ground state transition energy in the $In_xGa_{1-x}N$/GaN nanowire heterostructure computed on the basis of the strain distribution and electric potential simulated by FEM for model (c) in Fig. 4.1 as a function of the disk thickness t. The assumed In content x is indicated at each curve. For comparison, the transition energies for the limiting case of a planar heterostructure with the same In contents are indicated by black dashed lines whereas the gradations of gray indicate the assumed In content from light gray (20 %) to dark gray (100 %).

dashed lines show the results for for a planar heterostructure with the same In contents whose properties are projected on an equivalent NW geometry inducing the same spatial confinement. Here, a linear relation of the transition energies and an increasing $In_xGa_{1-x}N$ layer thickness is observed. The gray scale of the shaded areas refers to a particular In content with light gray corresponding to 20 % In and dark gray to 100 % In.

As becomes clear in Fig. 4.1, the evolution of the transition energy with increasing disk thickness t differs drastically between the planar system and the equivalent NW heterostructure. The linear decrease with layer thickness inherent to planar systems owes to the QCSE. However, in case of NWs the transition energies tend to saturate for thicker disks. In fact, this observation gives the impression that the NW heterostructure eventually reaches a state which is free of internal electrostatic fields or, in other words, it seems that the QCSE vanishes. However, it is important to note that this saturation is not caused by a vanishing internal electrostatic field but is due to the progressive elastic relaxation of strain which results in a complicated interplay between an increasing vertical separation of electron and hole and a reduction of the polarization potential as discussed in Fig 4.7. It is important to note that for the discussed structural parameters of

the NW heterostructure the strain induced by the $In_xGa_{1-x}N$ disk is expected to be accommodated elastically for the entire parameter range discussed in Fig. 4.9 [cf. Ref. [62]].

A fundamental consequence of the saturation of the transition energy for thicker disks is, that, apparently, the range of accessible wavelength is limited and that long wavelength emission requires a significantly higher In content compared to an equivalent planar heterostructure system. For example, red emission at about 1.9 eV is predicted to be achieved with a planar heterostructure containing 20 % In at a layer thickness of about 3.5 nm. A NW heterostructure emitting at this wavelength and with the same layer thickness would require an In content of about 45 %. Alternatively, it is possible to employ a 5.5 nm thick disk with an In content of 40 % or a 1.5 nm thick disk with an In content of 60 %. In other words, it is necessary to incorporate significantly larger amounts of In for achieving a comparable emission wavelength with respect to the equivalent planar system.

Concerning the optical performance, the electron-hole overlap is a crucial parameter. Consequently, it is of great interest if the reduced electric potential as observed in Fig. 4.7 leads to an improved electron-hole overlap in the discussed NW heterostructures in comparison to their planar equivalents. For that, the material properties of a planar system are projected onto an equivalent NW geometry to have the same spatial confinement. Here, the electron-hole overlap $\mathcal{O}$, defined as the product of the 3D electron and hole ground state charge densities [cf. Ref. [175]], is extremely small (1.17×10^{-9}) for an emission at 1.9 eV. This result owes to the strong polarization potential. In comparison, looking at Fig. 4.9, emission at the same energy is predicted for NW heterostructures with an In content of 40 % and a 5.5 nm thick disk or 60 % In and a disk thickness of 1.5 nm. For these two structures, values of 4.06×10^{-5} and 1.56×10^{-3} are obtained, respectively. Here, of course the thinner disk leads to a decreased spatial separation and, thus, an improved overlap of electrons and holes along the growth direction. The obtained values allow to draw a first, conclusion that the electron-hole overlap is significantly improved compared to a planar layer system emitting at the same wavelength.

To investigate the electron and hole charge density distribution and their overlap in more detail, a systematic study is presented in Fig. 4.10. Here, the electron and hole ground state charge densities are shown for selected parameter sets based on model (c) in Fig. 4.1. The electron charge density is colored in red, the holes in blue and below that their respective overlap $\mathcal{O}$ is shown. In general, for either thin disks or a low In content the electron is confined in the center of the NW, as visible in Fig. 4.10. When increasing these two parameters, the electron tends to be confined in the corners of the hexagonal NW. However, the confinement of the hole proceeds in a more complex manner. Only when considering a disk thickness of 0.5 nm and an In content of 20 % the hole is confined in the NW center. With both, larger disk thickness and an increasing In content, the hole tends to be more and more confined at the NW surface. Here, two cases are observed: For example, for disk thicknesses of 4.5 and 6.5 nm and an In content of 60 % the hole is confined at the corner whereas for example at disk

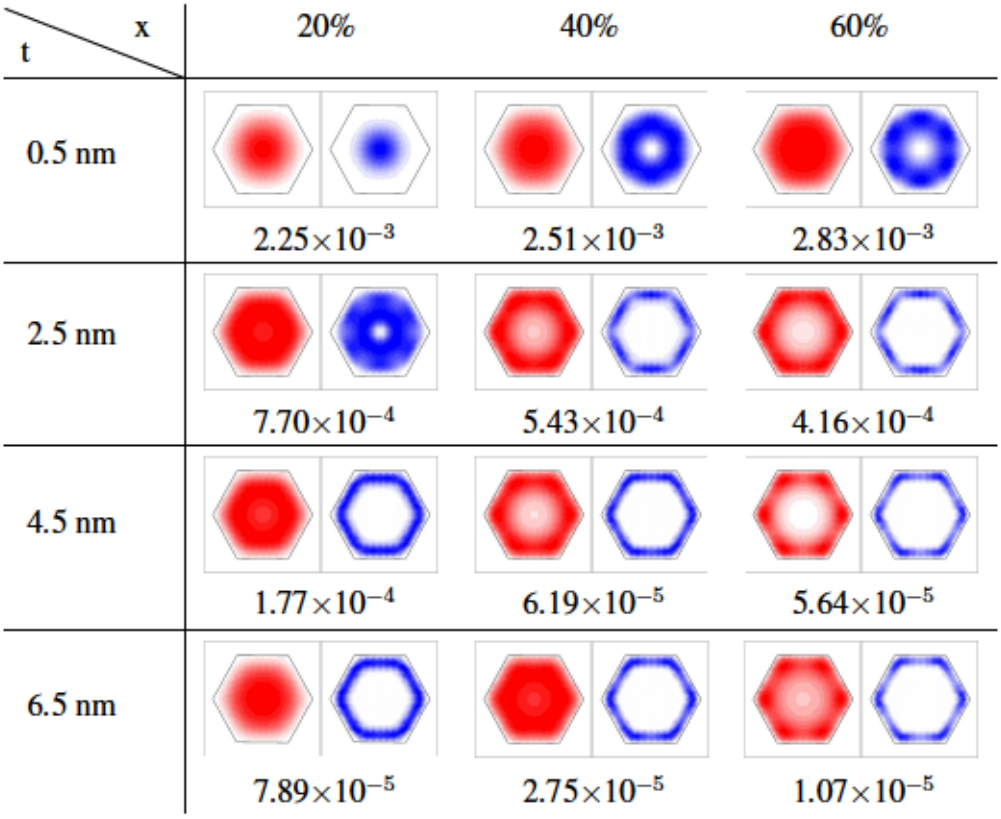

Figure 4.10 Systematic study of electron (red) and hole (blue) ground state charge densities for different In contents and disk thicknesses in top-view. The number below the charge densities indicates their respective overlap $\mathcal{O}$.

thicknesses of 2.5 nm the hole is confined at the side-facets as also reported in Ref. [176]. Moreover, due to the drop of the polarization potential along the NW axis visible in Fig. 4.6, the electron is confined at the top facet of the embedded $In_xGa_{1-x}N$ disk, whereas the hole resides at its bottom. Consequently, the vertical separation increases with increasing disk thickness yielding a reduction of the overlap as is indeed visible in Fig. 4.10. Obviously, the fact that electrons are generally confined at the corners whereas holes can either be located at the corners or at the side-facets leads to the requirement of choosing a configuration where the overlap of electron and hole is maximized. However, as this study suggests, no simple monotonic trend for the electron-hole overlap as a function of disk thickness and In content can be predicted and the optimal parameters have to be found uniquely for each NW configuration which of course is an elaborate procedure.

5 Scanning nanofocus x-ray diffraction on individual (In,Ga)N/GaN micro-rods

The 3D device design of micro-rods in a core-shell geometry, offers a drastic increase of the active area compared to the previously discussed axial NWs and conventional planar films [103, 177–179]. Especially interesting are $In_xGa_{1-x}N$ based devices where the incorporation of In from x = 0 to 1 allows to tune the emitted wavelength through the visible spectrum as discussed in Fig. 2.2. Consequently, these objects are discussed as the next generation of low cost, high efficiency LEDs.

However up to now, a major drawback of these structures is that the efficiency of conventional planar structures has not been reached yet. Reasons for that might be on the one hand that the growth regimes are usually different to the established ones used for planar structures [12]. On the other hand, conventional characterization techniques become insufficient with decreasing homogeneity within ensembles of low-dimensional objects as they lack either in resolution or are time consuming. Actually, it becomes necessary to obtain information about the morphology, the chemical composition and the resulting strain state of individual objects to draw conclusions about the overall condition of an ensemble and its optoelectronic performance.

In this respect, nanofocus x-ray diffraction with a resolution in the sub-µm regime available at synchrotron sources has proven to be a powerful technique [37, 40, 47, 58]. In scanning nanofocus x-ray diffraction experiments, information about the local strain state of individual objects within an ensemble has been retrieved [35, 36] and, recently, a 2D strain mapping scheme has been presented allowing to investigate micro-rod ensembles [52]. Moreover, due to the high spatial resolution, nanofocus x-ray diffraction investigations of the local strain state in low-dimensional objects can be correlated to subsequent, e. g., electrical or optical measurements performed on identical objects.

In this chapter, the strain field normal to the side-facets of three neighboring core-shell (In,Ga)N/GaN rod LEDs is investigated exploiting nanofocus x-ray diffraction. The strain state in individual facets of these rods is analyzed and correlated to representative spatially-resolved cathodoluminescence measurements performed on rods from the same sample. The results are interpreted by employing the numerical FEM and subsequent kinematic scattering simulations as introduced in sections 2.4 and 2.9, respectively. Parts of this chapter have been published in Ref. [180].

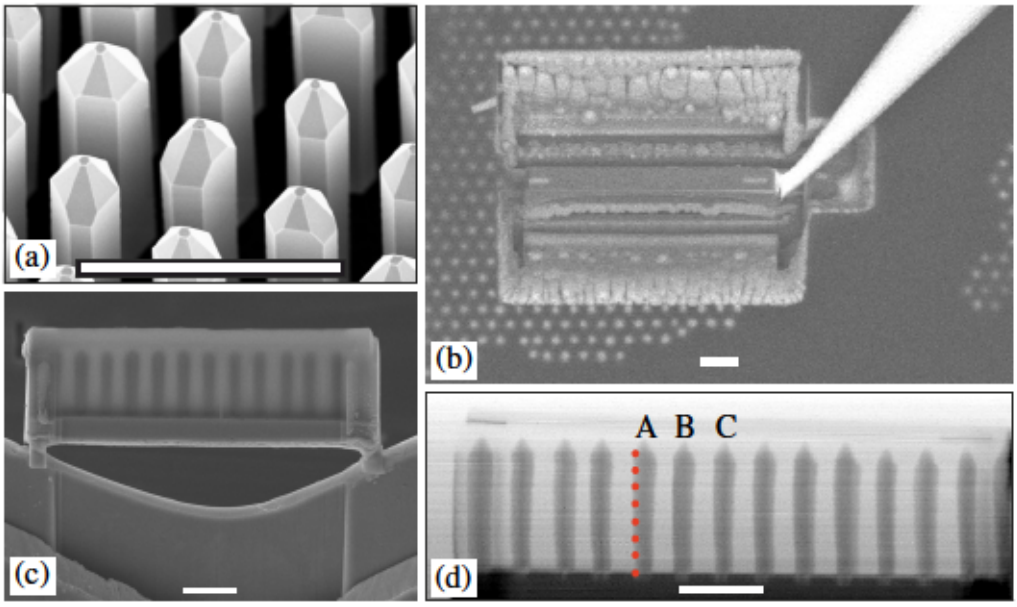

Figure 5.1 Bird's eye view scanning electron micrograph recorded under a tilt of 30° of the (In,Ga)N/GaN micro-rods as-grown (a). Next to the lamella trenches are visible as well as the manipulator needle used for lifting out (b). Scanning electron micrograph of the embedded sample mounted on a support (c), and scanning x-ray transmission image of the extracted lamella containing a single row of free-standing rods recorded with $150 \times 150\,\mathrm{nm}^2$ spot size (d). The rods A, B and C have been investigated whereas the left facet of rod A is discussed in particular. Here, the red dots indicate vertical sampling positions [cf. Fig. 5.9(a)]. The horizontal white scale bars refer to 5 µm in all images.

5.1 The core-shell (In,Ga)N/GaN rods

The (In,Ga)N/GaN micro-rods presented in Fig. 5.1 are grown by selective area metalorganic vapor phase epitaxy (MOVPE) on a GaN buffer layer on a Al_2O_3 substrate[1]. A SiO_x mask is deposited on top which is structured with holes of 800 nm in diameter and a pitch of 2.4 µm. In this way, the rods grow at predefined and well-ordered positions [cf. Fig. 5.1(a)]. For the growth of the n-doped GaN core, trimethylgallium, NH_3 and SiH_4 is injected into the vertical close coupled showerhead reactor. By the help of a low V/III ratio (33) and high SiH_4 flows (110 nmol/min in the first half of the growth, 16 nmol/min afterward) the vertical growth is favored [181]. Subsequent to the core growth, the shell layers of the LED structures are grown under standard layer conditions with high V/III ratios. First, an unintentionally doped GaN shell is deposited. Following this, a five-fold (In,Ga)N/GaN multi-quantum well (MQW) with an estimated QW real temperature of 700 °C and a Mg-doped p-GaN shell is grown. By an in-situ annealing under H_2 free atmosphere, the p-GaN is activated.

In order to obtain information about individual rods, a focused Ga^+ ion beam (FIB) is used to isolate a single row of neighboring, free-standing rods within a lamella[2]. Here, the FIB is an ideal preparation technique as it allows a targeted

[1]The investigated micro-rods are grown by the group of Prof. Dr. A. Waag (TU Braunschweig).
[2]The FIB preparation has been performed by Dr. M. Niehle (Paul-Drude-Institut Berlin).

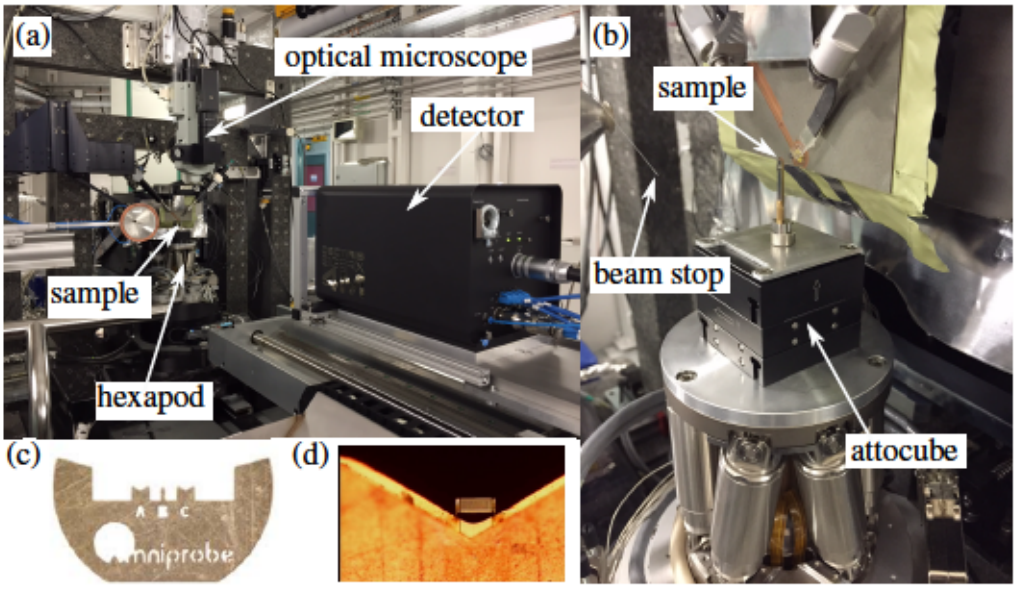

Figure 5.2 In (a) a photograph of the experimental setup at ID13 is shown. For a first alignment of the sample an optical microscope has been employed. The detector is placed about 50 cm behind the sample and can be moved within the x-y-plane. In (b) the sample environment is illustrated: On the hexapod an attocube is mounted with which the scanning movements are performed. On top of the scanning motor a brass pin is placed which holds a Cu grid as displayed in (c). In the optical microscope image (d), the lamella attached to one of the labeled pins of the Cu grid can be seen.

isolation of low-dimensional objects with the additional freedom of choosing its crystallographic orientation within a lamella [182]. For the FIB preparation, the rods are embedded by epoxy glue diluted with acetone to reduce the viscosity. For conductivity enhancement the glue is mixed with carbon black. The embedded rods are protected by a carbon depot with which the first and last rod of the lamella are also marked. Figure 5.1(b) shows a scanning electron microscope (SEM) image of the lamella with trenches next to it. With a manipulator needle the lamella is lifted out and mounted on a standard Cu grid, see Fig. 5.1(c). Using small beam sizes, fine polishing steps are performed to get rid of re-deposited GaN crystallites on the lamella surface. Due to the short penetration depth into the glue Ga atoms are not implanted into the rod themselves such that the active regions are still functioning. The orientation of the rods within the lamella is chosen in the way that an m-plane faces its neighboring m-plane such that the strain along the $\langle 10\bar{1}0 \rangle$-direction can be accessed.

5.2 Experimental setup at beamline ID13

Probing strain at the sub-µm scale with hard x-rays remains a domain of synchrotron-based, highly specialized experimental stations. The presented experimental data are recorded at beamline ID13, ESRF, consisting of Si-based NFLs as described in section 2.6 with which a spot size of $150 \times 150\,\mathrm{nm}^2$ FWHM and a photon flux of about 10^7 photons/second at 14.9 keV is realized. All diffraction

patterns are recorded using an EIGER 4M detector which has been placed about 50 cm away from the sample. This detector has a pixel size of $75 \times 75\,\mu m^2$, a total number of pixels of 2070×2167 and a maximum frame rate of 750 Hz [183]. The lamella was initially aligned using an optical microscope and its adjustment was further improved by scanning x-ray transmission. Employing the latter technique, the investigated lamella has been pictured and the result is presented in Fig. 5.1(d).

Figure 5.2(a) shows a photograph of the used nanoprobe setup in the experimental hutch of ID13 which is located about 100 m away from the undulator source. The 2D detector can be positioned in the x-y-plane and an optical microscope can be moved downwards for pre-aligning the sample. In (b) it is illustrated that the sample is mounted on an attocube which consists of three orthogonal piezo-motors utilized for the scanning experiment. This motor provides an accuracy of movements of about 10 nm and is placed on top of a hexapod which next to movements in orthogonal directions also allows to correct tilting of the sample. The sample holder is a specifically designed brass pin with an attached metal plate such that a Cu grid as displayed in (c) can be clamped mechanically. Behind the sample, a beam stop is installed to block the primary beam and to prevent damaging of the detector. The Cu grid has three labeled pins and on one of them the lamella is mounted as shown in the optical microscope image in (d). The experimental hutch is air-conditioned providing a stable climate inside the hutch with temperature fluctuations less than 100 mK.

5.3 Scanning nanofocus x-ray diffraction

To access the strain normal to the core-shell (In,Ga)N/GaN rod side-surface, two sets of lattice planes can be probed in an x-ray diffraction experiment. The $\{10\bar{1}0\}$ m-planes with a normal vector standing orthogonal on the side-facets and the $\{11\bar{2}0\}$ a-planes [cf. Fig. 2.1]. The vector normal to the a-planes points towards the corners of the hexagonal rod. While the x-ray beam diffracted on m-planes is sensitive to the strain pointing normal to the side-facets, the x-ray beam diffracted at a-planes is sensitive to the strain pointing towards the rod corners.

Figure 5.3 shows a stereographic projection of the reciprocal lattice of GaN onto the [0001]-direction. The a-plane reflections are connected by green dashed lines and the m-plane reflections by blue dashed lines. With respect to the substrate surface, both directions correspond to the most non-coplanar case and the corresponding scattering setup can be specified as GID. Due to the 3D geometry of the rods, the angles α_i and α_f measured with respect to the substrate are even exact zero such that the scattering plane lies parallel to the substrate surface. In that sense, it might be more convenient to consider the GaN core as reference for describing the scattering geometry which would mean that for measuring m-plane reflections the setup can be characterized as symmetric and coplanar.

In all what follows in this chapter, the experimental data are related to nanofocus x-ray diffraction experiments performed on $\{10\bar{1}0\}$ lattice planes. In particular, the strain states of three neighboring rods labeled with A, B and C in

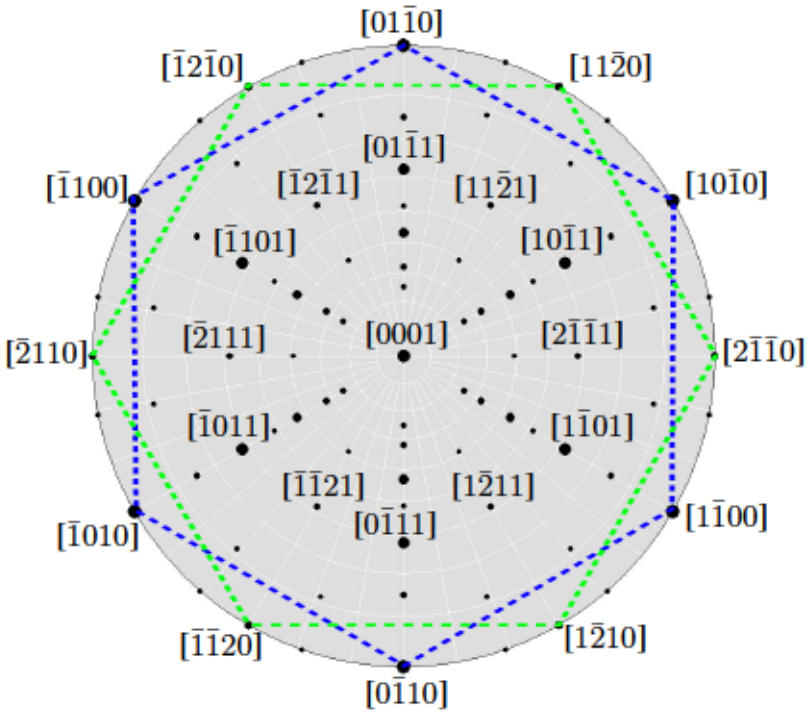

Figure 5.3 Stereographic projection of the reciprocal lattice of III-nitrides onto the [0001]-direction. The blue dashed lines connect the m-plane and the green dashed lines the a-plane reflections. Both reflections are sensitive to the strain field normal to the side-surface of the rods.

Fig. 5.1(d) are discussed. With a step size of 100 nm, the x-ray beam has been moved horizontally over the targets. At each position, angle-resolved maps have been recorded to retrieve information about the strain induced by the MQW which can be retrieved from the separation of GaN and (In,Ga)N-related peaks. Here, a typical scan comprises 71 steps in horizontal direction and, at each position, an angular interval of 5 ° has been probed with a resolution of 0.05 ° whereas an exposure time of 0.05 seconds has been applied. The described scan series has been repeated at eight different heights spaced at intervals of about 1 µm such that the range from bottom to just below the tip of the rod is covered as indicated by the red spots in the same figure.

An illustration of the scanning experiment using the example of one rod is provided in Fig. 5.4(a). Here, the indexes E1 to E7 refer to a horizontal movement of the x-ray probe across the object. Due to the spot size of about $150 \times 150\,\mathrm{nm}^2$ the spatial resolution in horizontal direction is about 1:10 with respect to the rod diameter. The shaded gray area indicates the scattering volume which is illuminated by the x-ray beam and $\mathbf{k}_i$ and $\mathbf{k}_f$ depict the wavevectors of the incoming and the scattered x-ray beam, respectively. Between positions E1 and E3 the beam mainly illuminates the vicinity close to the $(10\bar{1}0)$ m-facet and in particular the embedded MQW. In contrast, at the central location E4, exclusively areas near the symmetry axis are probed, and eventually, from E5 to E7, the effective scattering volume approaches the opposite MQW near the $(\bar{1}010)$ facet. Moreover, while the x-ray beam around position E1 is reflected in Bragg geometry,

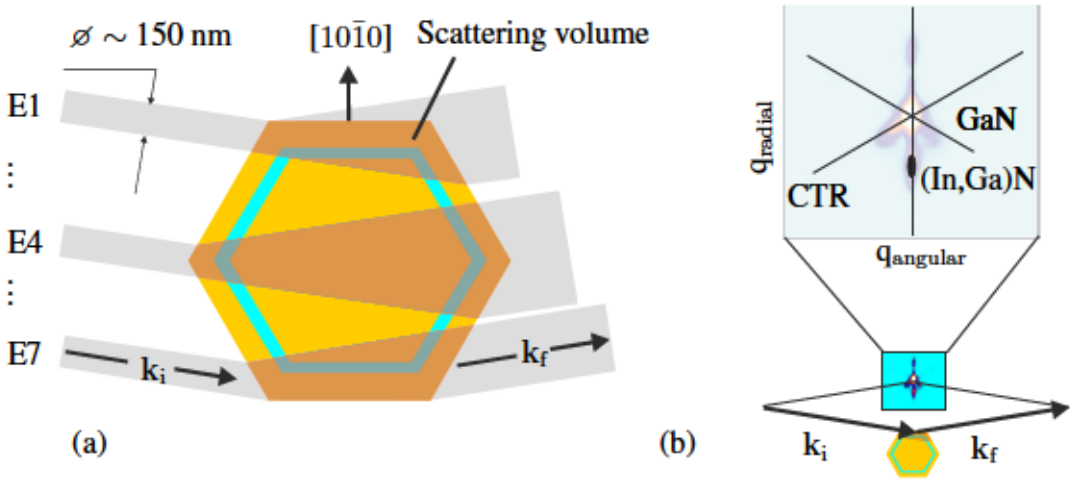

Figure 5.4 Sketch of the scattering volume at different beam positions on the rod (a). Here, $\mathbf{k}_i$ and $\mathbf{k}_f$ depict the wavevectors of incident and diffracted x-ray beams with a connecting scattering vector perpendicular to an m-plane, thus along [10$\bar{1}$0]. In the symmetric diffraction regime the reciprocal space is probed along the radial, here the [10$\bar{1}$0] direction. In the reciprocal space map, the peak separation along the radial direction (q_{rad}) contains information about the strain state whereas the angular direction (q_{ang}) is strain-insensitive and mainly influenced by the shape function of the rod. For the latter it is expected that the crystal truncations rods appear in a six-armed star as sketched in (b) which originates from the hexagonal cross-section of the rod.

the x-ray beam is transmitted through the rod for the following positions such that the Laue case is established [cf. Fig. 2.5].

Figure 5.4(b) shows a representative reciprocal space map (RSM) which is obtained from an angular scan at a fixed position on a rod. The wavevectors $\mathbf{k}_i$ and $\mathbf{k}_f$ indicate the diffraction of the x-ray beam on a m-plane facet in Bragg geometry. Both wavevectors define the scattering vector $\mathbf{q}$ [cf. Eq. 2.7.2] which can be composed of a radial contribution, q_{rad}, and an angular contribution, q_{ang}. When changing incident and exit angle in a symmetric diffraction setup, the magnitude of the scattering vector $\mathbf{q}$ is changed and the reciprocal space is probed along the radial, here the [10$\bar{1}$0] direction. Thereby, the length of the scattering vector $|\mathbf{q}|=|\mathbf{k}_f - \mathbf{k}_i|$ changes and due to different lattice parameters of GaN and (In,Ga)N one may expect to detect a separation of the corresponding Bragg reflections. In contrast, the (orthogonal) angular direction will be probed as long as $|\mathbf{q}|$= constant. This section of reciprocal space contains mainly information from the rod shape. Here, one expects to see crystal truncation rods [cf. section 2.8] with a star-like shape originating from the rod's hexagonal cross-section. Indeed this is observed when the intensity is displayed in logarithmic scale [see Fig. 5.6].

5.4 Data evaluation

Figure 5.5(a) shows a representative detector image with a clearly visible diffraction spot identified as the GaN (10$\bar{1}$0) Bragg reflection. The primary beam which is blocked by the beam stop lies in the same horizontal plane as the diffraction

spot. The region of interest marked with a red box (ROI 1) is used to create the composite image of a complete scan series as shown in Fig. 5.5(b). A scan series comprises 71 positions in steps of 100 nm in y-direction, which corresponds to the horizontal movement of the three rods A, B and C through the x-ray beam. At each position the incident angle is varied in steps of 0.05 ° over an interval of 5 ° resulting in 101 angular positions. Consequently, a full scanning series at one constant height comprises 7171 detector images. The composite image now shows the intensity in the same ROI for each individual detector frame of a full scanning series. The position of each individual ROI within the composite image is determined by its Θ-value as well as its horizontal y-position. In other words, for a fixed y-position ROIs along the vertical axis show the evolution of the detected intensity in steps of 0.05 °.

Starting inside the glue, rod A moves horizontally towards the x-ray beam and after approximately 1 µm the outer facet is reached. After a further shift of about 1.5 µm the x-ray beam leaves rod A and passes between rods A and B. With increasing y-positions, the x-ray beam reaches rods B and C. In vertical direction, the detected intensity within the ROI increases and slightly above the middle of the plot, the ROI is related to a Θ-value for which the Bragg condition for the GaN $(10\bar{1}0)$ reflection is met resulting in the most intense peak. Interestingly, while the Bragg condition for rods A and B is met for the same Θ-value, the Bragg condition for rod C is fulfilled 0.1 ° earlier. A possible explanation could be a slight tilt of rod C with respect to rods A and B.

The detector images are not yet conformal and have to be transformed into reciprocal space coordinates for evaluating the experimental data. In fact, from a set of angular-resolved detector frames belonging to the same y-position a RSM can be constructed in the way outlined in the following. In a first step, the intensity line profile of a single detector frame is obtained which is shown using the example of Fig. 5.5(a). Here, the ROI in blue (ROI 2) is used and the intensity of all pixels within ROI 2 are summed up in vertical direction. The summation comprises about 5 pixels in vertical direction which corresponds to an integration over approximately 0.0003 Å^{-1} in vertical direction. For this task, a specifically developed source code for the open source software package ImageJ is applied. Eventually, the assemblage of all line profiles of one angular-resolved scan series at a fixed y-position represents a 2D angular-resolved map of the intensity around a Bragg peak. Afterward, the transformation into reciprocal space coordinates is done via

$$\begin{aligned} q_{\text{rad}} &= \frac{2\pi}{\lambda}[\sin(\alpha_{\text{i}}) + \sin(\alpha_{\text{f}})]\,, \\ q_{\text{ang}} &= \frac{2\pi}{\lambda}[\cos(\alpha_{\text{i}}) - \cos(\alpha_{\text{f}})]\,, \end{aligned} \tag{5.4.1}$$

where α_{i} and α_{f} are defined with respect to the side-facet and are given by

$$\begin{aligned} \alpha_{\text{i}} &= -[b - O_{\text{b}}] * \tau + \Theta_{\text{B}} - [a - O_{\text{a}}] * \Delta\Theta\,, \\ \alpha_{\text{f}} &= [a - O_{\text{a}}] * \Delta\Theta + \Theta_{\text{B}}\,. \end{aligned}$$

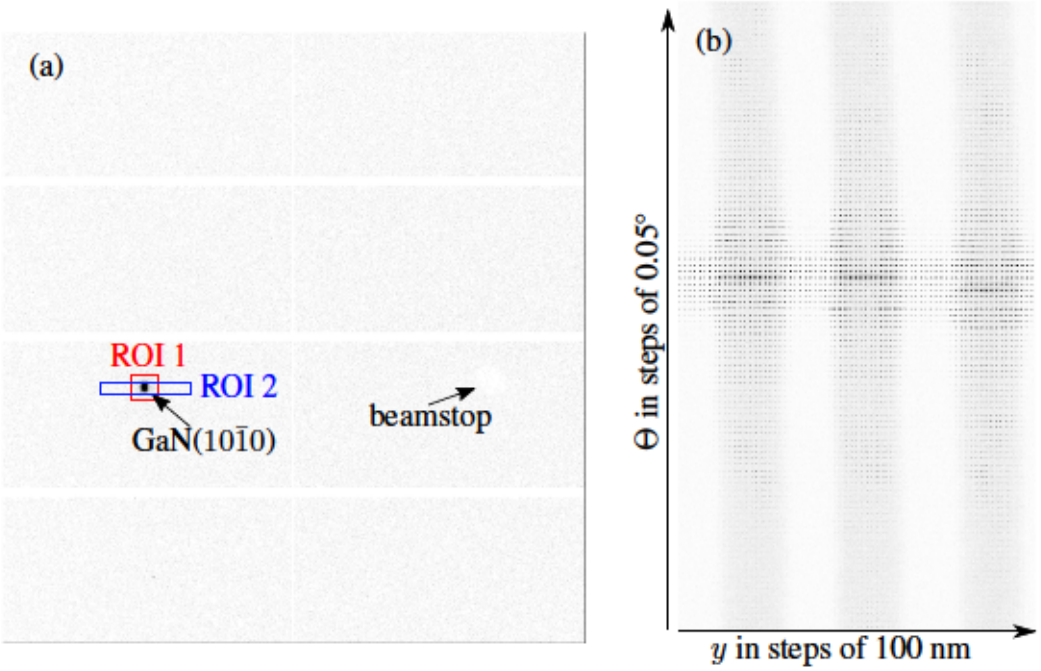

Figure 5.5 In (a) a representative detector image in Bragg condition for the GaN (10$\bar{1}$0) reflection is shown. The primary beam lies in the same horizontal plane as the diffracted x-ray beam but is blocked by the beam stop. By extracting ROI 1 from all images of a scanning series (7171 frames) a composite image can be constructed (b) where the vertical axis gives the angular scanning resolution and the horizontal axis the spatial scanning resolution which has been applied to the x-ray beam horizontal movement across rods A, B and C. The blue box labeled with ROI 2 shows the area over which the intensity has been vertically integrated to construct reciprocal space maps.

Here, a is the pixel number in horizontal direction with the largest value corresponding to the total number of detector frames. The pixel number in vertical direction is denoted by b whereas, here, the maximum value corresponds to the number of pixels along the horizontal direction in ROI 2. The offsets O_a and O_b in a and b, respectively, are measured with respect to the position of the GaN (10$\bar{1}$0) peak. Furthermore, the step size $\Delta\Theta$ is given by the angular resolution of the scan, here, 0.05 ° and the number of pixels per degree, τ, can be calculated from the pixel size of the detector and the distance between detector and sample.

In Fig. 5.6, a sequence of RSMs is presented which corresponds to scanning positions in y-direction over rod A in steps of 100 nm [cf. Fig. 5.5(b)] at a height just below the tip. From left to right the RSMs display the diffracted intensity of the GaN (10$\bar{1}$0) Bragg reflection starting at the left facet and moving to the right facet. The intensity is shown in logarithmic scale and the diffusely scattered intensity around the GaN (10$\bar{1}$0) peak shows the CTRs in form of a six-armed star representing the hexagonal cross-section of the rod. Interestingly, all six CTRs are only clearly visible at the outer rod positions corresponding to the left and right facet. Moreover, the strong intensity modulation along $\mathrm{q_{rad}}$ at $\mathrm{q_{ang}} = 0$ is mainly visible at these positions, too, and vanishes if the x-ray beam is diffracted in the rod center. These observations will be elaborated in the following section.

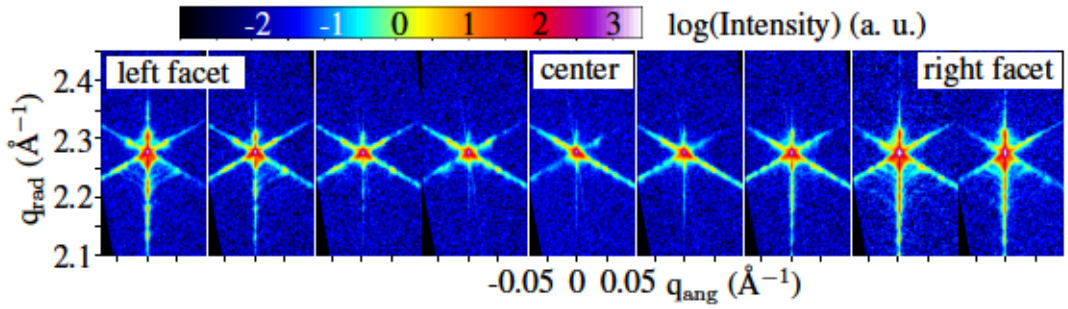

Figure 5.6 Reciprocal space maps of the scattered intensity in logarithmic scale at different horizontal positions on rod A. The reciprocal space maps from left to right correspond to a movement of rod A with respect to the x-ray beam, accordingly. The horizontal translation in steps of 100 nm has been performed at a constant height just below the tip of rod A. The diffusely scattered intensity around the main GaN $(10\bar{1}0)$ Bragg reflection displays the hexagonal cross-section of the rod in form of crystal truncation rods.

5.5 Results and discussion

Figure 5.7(a) shows a representative excerpt of the measured RSMs retrieved from rod A at its highest position in Fig. 5.1(d). All RSMs contain a contribution at the nominal position for relaxed GaN at $q_{rad} = 2.277$ Å^{-1}. However, at smaller q_{rad} a pronounced peak related to (In,Ga)N is only detected at positions E1 and E7 and looses intensity while the beam moves towards the rod center [cf. Fig. 5.6]. At position E4, where the x-ray beam hits the symmetry axis, the contribution vanishes completely.

This can be understood by looking at the strain map [cf. Fig. 5.8] as simulated by the FEM using the commercial package MSC.Marc2008rl. Here, the ε_{xx} component of the *total* strain tensor is displayed which takes relaxed GaN as reference. In the simulation, a constant QW thickness of 3 nm and an In content of 10 % is assumed. The elastic constants are taken from Ref. [152], while for the ternary (In,Ga)N alloy they are obtained via linear interpolation following Vegard's law [cf. Eq. 2.1.4]. Noteworthy to say that the inherent six-fold symmetry of the problem is virtually reduced to a two-fold symmetry as soon as plotted in Cartesian coordinates. However, if the incident plane wave is diffracted on the $\{10\bar{1}0\}$ lattice planes, i. e., along the x-axis, ε_{xx} maps directly the strain component to which the x-ray beam is sensitive to.

In orthogonal coordinates, the two opposing m-facets parallel to the y-axis have zero contribution in ε_{yy} such that ε_{xx} is maximal. The surface normals of the four m-facets in between are a superposition of x- and y-direction, resulting in non-zero ε_{xx} and ε_{yy} components. This explains the smaller values for ε_{xx} inherent to the four inclined side-facets as visible in Fig. 5.8. Comparing the strain map with the volume illuminated by the x-ray beam [cf. Fig. 5.4(a)] indicates that at position E1 the MQW in the $(10\bar{1}0)$-facet is covered - an area where ε_{xx} approaches its maximum. At position E4, however, the x-ray beam illuminates a volume where ε_{xx} is considerably smaller. That is why the separation between GaN and (In,Ga)N peak decreases and cannot be resolved anymore.

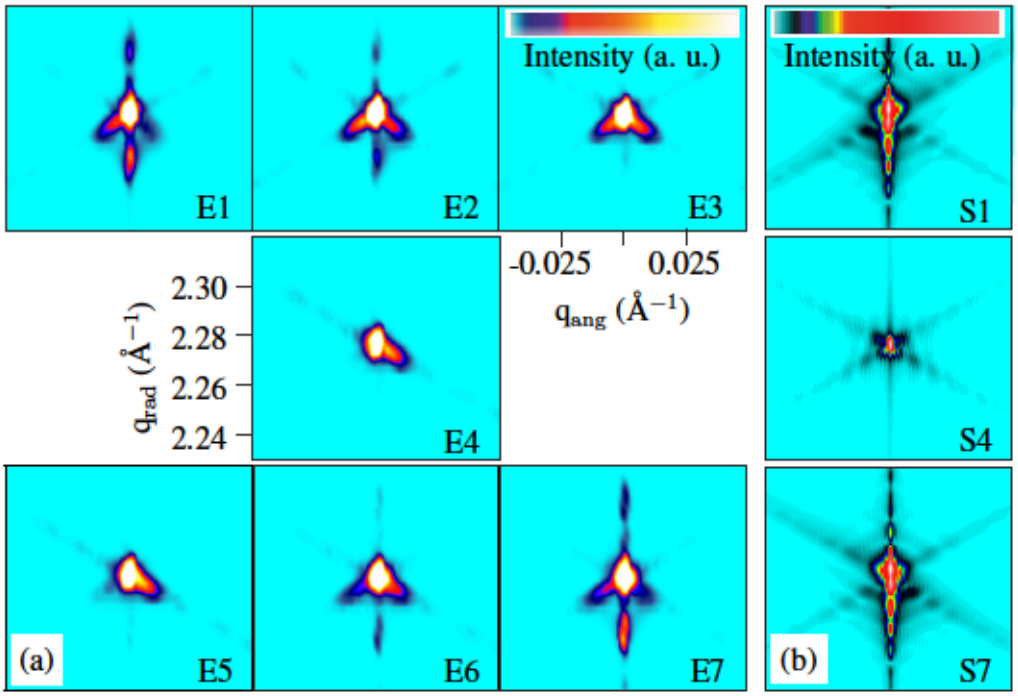

Figure 5.7 In (a) experimental reciprocal space maps measured at different horizontal positions are shown. The positions correspond to the sketch in Fig. 5.4(a). In radial direction a separation between (In,Ga)N and GaN peak is expected as indeed visible at positions E1 and E7. However, this contribution completely vanishes at position E4 which is a central position on the rod. In (b) simulated scattering patterns are depicted which are computed using Eq. 5.5.2. Here, positions S1, S4, S7 correspond to positions E1, E4, E7 and show good agreement to the measured reciprocal space maps.

When reaching the opposing facet at E7, ε_{xx} becomes maximal again while ε_{yy} vanishes. Hence, the (In,Ga)N peak reappears. This indicates that the resolution of the x-ray beam allows to distinguish the strain field in individual facets.

To confirm this interpretation, kinematic scattering simulations are performed which include the displacement field obtained by FEM. In the limit of weak photon scattering, which is justified for low-dimensional structures, the kinematic scattering approach is particularly powerful for simulating intensity patterns of diffusely scattered x-rays as introduced in section 2.9. In order to mimic the situation of the performed nanofocus x-ray diffraction experiment a Gaussian beam profile

$$G(\mu,\sigma) \equiv \frac{1}{\sqrt{2\pi}\sigma} \exp\left[-\frac{(r_i-\mu)^2}{2\sigma^2}\right] \tag{5.5.1}$$

is appended to the kinematic sum [cf. section 2.9]

$$I(\mathbf{q}) \propto \left|\sum_i G(\mu,\sigma) f_i(\mathbf{q}) \exp\left[i\mathbf{q}\cdot(\mathbf{r}_i+\mathbf{u}(\mathbf{r}_i))\right]\right|^2 \tag{5.5.2}$$

which makes it possible to position the beam center with μ and to tune the

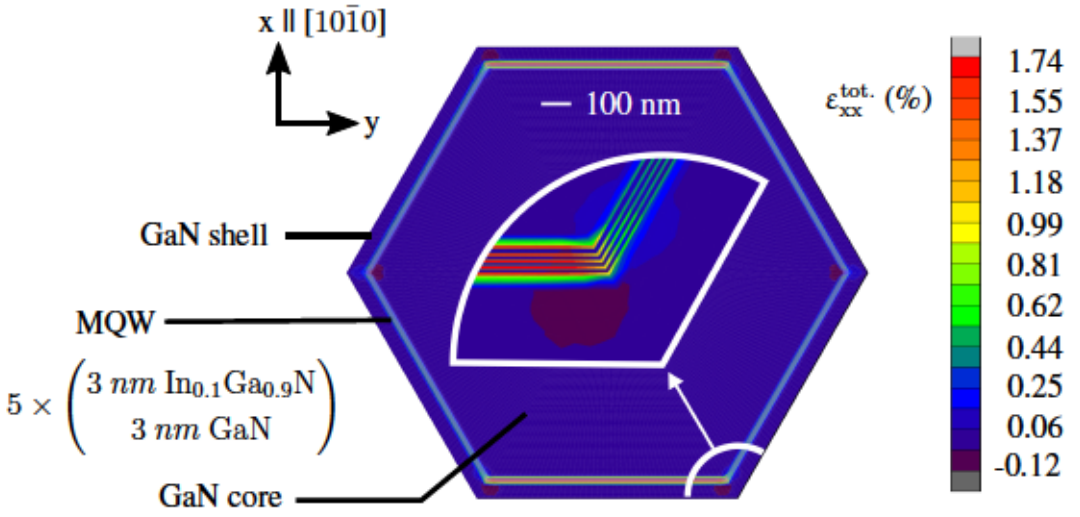

Figure 5.8 Top-view image of the total strain component ε_{xx} as derived by finite element method assuming an embedded, symmetric five-fold GaN/(In,Ga)N MQW containing 10 % In and a QW thickness of 3 nm. Importantly, the strain component is shown in Cartesian coordinates yielding a two-fold symmetry. This component is of particular interest as it displays the deformation along the facet normal to which an x-ray beam scattered, e. g., on the (10$\bar{1}$0)-facet is sensitive to.

FWHM which is related to the variance σ via σ=FWHM/2ln(2). In the kinematic sum $\mathbf{q} = (q_x, q_y, q_z)$ denotes the scattering vector, $f_i(\mathbf{q})$ is the atomic form factor, and $\mathbf{r}_i$ points towards the individual atoms [cf. section 2.9]. The atomic displacement $\mathbf{u}(\mathbf{r}_i)$ is retrieved via interpolation of the atomic coordinates $\mathbf{r}_i$ with the displacement field $\mathbf{u}$ obtained from FEM.

Figure 5.7(b) shows three simulated RSMs based on Eq. 5.5.2 matching positions E1 (S1), E4 (S4) and E7 (S7) of Fig. 5.7(a). At positions S1 and S7, the modulation of the x-ray diffraction pattern due to elastic strain caused by the MQW is clearly visible. It is this modulation which vanishes in S4, where the beam is positioned in the rod center. The good agreement between experiment and simulations allows to conclude that the x-ray beam is actually sensitive to the local strain field induced by a MQW in a single facet. Moreover, it indicates that the MQW is strained in the direction normal to the side-facet. Further evidence for the beam position on the rod is the appearance and disappearance of CTRs, which can be related to the illuminated side-facets [59]. All six CTRs become only visible, if the beam illuminates three neighboring side-facets simultaneously [cf. S1 and S7]. Moreover, this phenomenon can be observed in Fig. 5.6 which shows the CTRs in a more pronounced way due to the applied logarithmic scale.

By moving the x-ray beam vertically along the rod it is possible to detect fluctuations of the local strain field in individual side-facets. Figure 5.9(a) shows line profiles of the scattered intensity along [10$\bar{1}$0], which is the strain sensitive q_{rad} direction. The line profiles are extracted from experimental RSMs taken at eight different heights in steps of about 1 µm on the left facet of rod A as indicated by the red spots in Fig. 5.1(d). As expected from the FEM simulations,

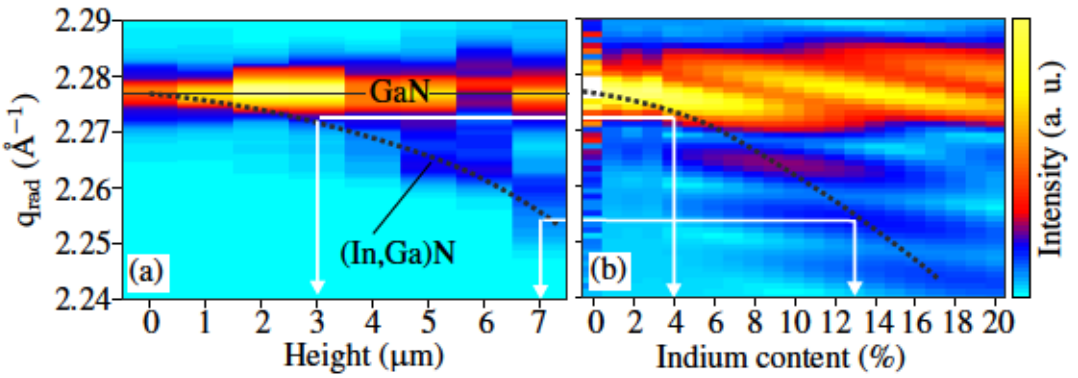

Figure 5.9 In (a) a sequence of line profiles along q_{rad} (q_{ang} = 0) extracted from measured reciprocal space maps at the positions indicated by the red spots in Fig. 5.1(d) are shown. In (b) simulated line profiles along the same direction for different In contents ranging from 0 to 20 % are presented. The dashed black lines are a guide to the eye indicating the position of the (In,Ga)N-related peak with respect to the rod height (a) and the In content (b). The (In,Ga)N peak positions at different heights in (a) can be directly translated - via solid white arrow lines - into different In contents (b).

a peak at the q_{rad}-value for relaxed GaN is visible at all line profiles. However, for the bottom 3 µm it is not possible to detect any (In,Ga)N-related contribution. Only beyond this level a weak fingerprint, just below the GaN peak, appears and shifts to smaller q_{rad}-values with increasing scanning height. This means that the magnitude of the strain normal to the side-facet increases gradually along the rid height.

Figure 5.10 presents RSMs extracted from positions on the left and right facets of rods A, B and C for seven different rod heights. For all three rods the bottom two RSMs provide hardly any indication for an (In,Ga)N-related peak which is expected to appear below the GaN $(10\bar{1}0)$ reflection. However, starting approximately at the middle, another reflection just below the GaN peak can be observed. Its position moves to lower q_{rad}-values depicting that the magnitude of the strain normal to the side-facet increases along the rod height. As this behavior is well reproduced for all investigated facets of rods A, B and C the detailed investigation of the left facet of rod A [cf. Fig. 5.9] can be seen as a representative study.

In order to find the origin of the observed strain gradient, the dependency of the peak position on the In content as well as on the QW thickness has been simulated employing Eq. 5.5.2. Via transmission electron microscopy analysis, a QW width of about (3 ± 1) nm has been observed. However, a fluctuation of the width by ± 1 nm is found to have a weak influence on the diffraction pattern and the (In,Ga)N peak position. Moreover, FEM simulations confirm that a QW thickness variation in the order of 1 nm changes the maximum value of ε_{xx} only by a very small amount (0.002 %), thus approaching the planar case at the facet center. However, a change of the chemical composition has indeed a strong impact on the (In,Ga)N peak position as the subsequent replacement of Ga by In atoms directly increases the lattice mismatch with the surrounding GaN

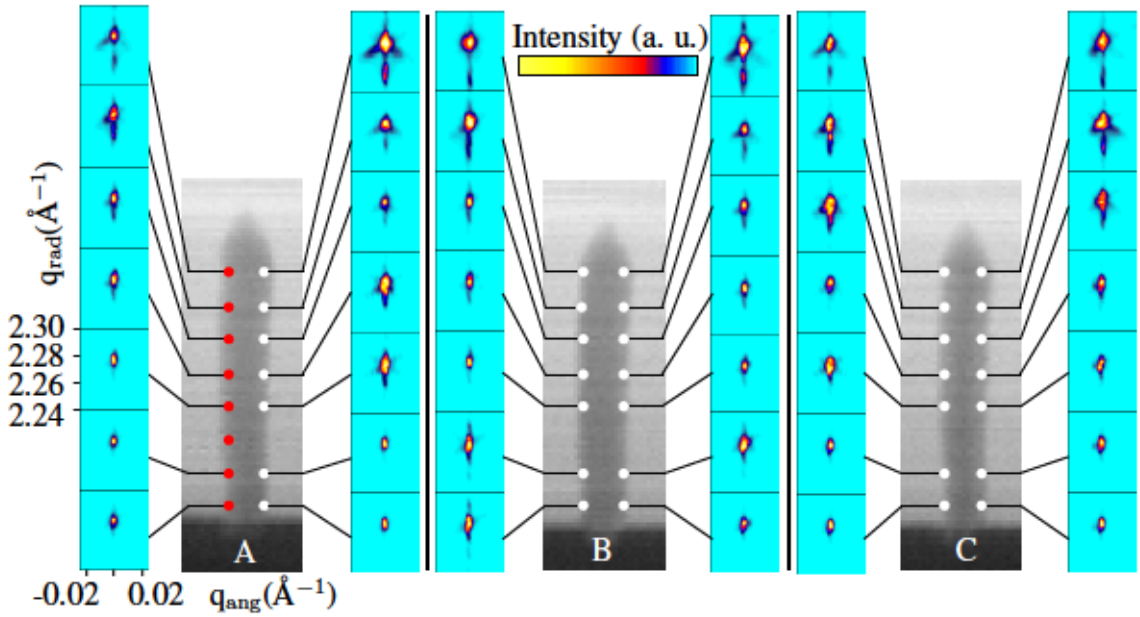

Figure 5.10 The measured diffusely scattered intensity around the GaN $(10\bar{1}0)$ reflection is shown in reciprocal space maps which have been recorded at the left and right facets of rods A, B and C. The beam positions are indicated by the white spots whereas the red spots correspond to positions of Fig. 5.9. In the lower part of the rods, there is hardly any indication for an (In,Ga)N-related reflection. However, starting approximately in the middle of the rods a second peak appears below the GaN reflection which can be attributed to the (In,Ga)N multi quantum well. Its position moves to lower q_{rad}-values indicating that the magnitude of the strain normal to the side-facet increases along the rod height.

matrix. This correlation can be directly seen in the simulated line profiles shown in Fig. 5.9(b). Here, the scattered intensity is plotted as a function of the In content and q_{rad}. The beam position on the rod is chosen such that the maximum of the beam profile is placed in the middle of the MQW embedded close to the $(10\bar{1}0)$-facet, corresponding to position E1 in Fig. 5.7(a). The GaN contribution stays at a constant q_{rad}-value, however, as soon as the five-fold (In,Ga)N MQW is considered the GaN peak smears out due to interference effects. Moreover, the (In,Ga)N peak, appearing below the GaN bulk contribution, bends towards smaller q_{rad}-values with increasing In content. As a guide for the eyes the dashed line in Fig. 5.9(b) follows the maximum of the (In,Ga)N-related peak. The modulation along q_{rad} (for a fixed In content) is due to the shape function matching the periodicity of the outer p-type GaN shell of about 70 nm thickness. On the basis of kinematic scattering simulations shown in Fig. 5.9(b) it is possible to conclude that the In content x in the $In_xGa_{1-x}N$ MQW changes from about 4±1 to 13±1 % over a height of 4 µm which is indicated by the white arrows. A possible scenario to explain this effect is the high density of rods which induces a diffusion gradient in the gas phase during the MQW growth. Due to the fact, that the GaN core is grown first and then overgrown by (In,Ga)N and GaN shells suggests that the diffusion length of In atoms on rod side-facets is too short in order to establish a homogeneous In distribution over the total rod height within

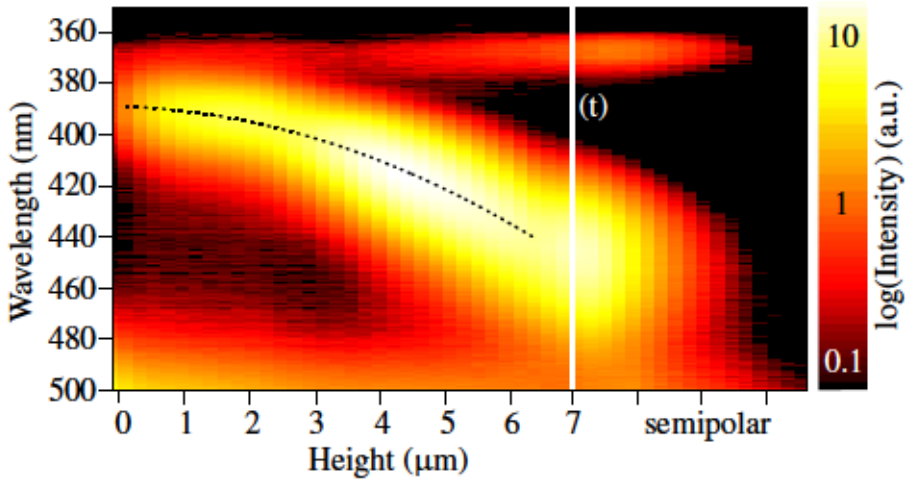

Figure 5.11 A spatially-resolved sequence of cathodoluminescence spectra (line scan) of a representative core-shell (In,Ga)N/GaN micro-rod is shown. Hereby, the intensity is plotted as a function of the emitted wavelength versus the rod height. At a wavelength of 365 nm the near-band-edge luminescence of GaN is observed. Starting at a wavelength of about 390 nm the emission from the multi quantum well can be seen which is red-shifted up to 440 nm along the rod height as indicated by the dashed line. The line (t) marks the onset of the top region where r-planes form the rod tip. Here, emission at an even higher wavelength is observed.

the (In,Ga)N QWs.

The gradient in the In content along the rod height has a significant impact on the optical performance of the LED. Figure 5.11 shows representative cathodoluminescence (CL) spectra[3] from line scans along a single rod obtained at a substrate tilt of 30° by exciting small regions of about 0.01 µm^2 with an electron probe of 15 keV and about 170 pA. At a wavelength of 365 nm the near-band-edge luminescence from GaN is visible. In the bottom region of the rod, the MQW emits at a wavelength of 390 nm. Above a height of approximately 2 µm the emitted wavelength is gradually red-shifted to larger wavelengths up to 440 nm at the top of the sidewall. Due to the orientation dependent growth mechanism, the In incorporation on the r-planes at the rod tip proceeds in a different fashion compared to the side-facets. Here, a higher In content is observed as well as a smaller QW width. This results in an emission at even higher wavelength, here at about 450 nm. At a wavelength of about 500 nm yellow luminescence resulting from point defects inside the GaN matrix can be observed [184]. The overall trend shown in Fig. 5.11 has been observed for all investigated individual LED-rods at different positions on the wafer and agrees very well with the investigation of the strain field via nanofocus x-ray diffraction [cf. Fig. 5.9].

5.6 Concluding remarks

In this chapter, a spatially-resolved investigation of the local strain field in individual core-shell (In,Ga)N/ GaN micro-rods using nanofocus x-ray diffraction is

[3]The cathodoluminescence spectra have been recorded by Dr. J. Ledig (TU Braunschweig).

presented. The resolution of about 1:10 of the spot size with respect to the rod diameter and an even better resolution along the rod height allows to analyze the local strain field normal to the side-facets within individual facets and to detect a significant strain gradient in the MQW along the rod height. With supporting FEM and subsequent kinematic scattering simulations it is possible to identify a gradient in the In content along the rod height as the origin. The strain analysis has been complemented with spatially-resolved CL measurements showing that the strain gradient can be directly correlated to a significant red-shift of the MQW emission wavelength along the rod height. Eventually, the presented results confirm that the sub-μm resolution available at synchrotron sources provides an ideal technique to locally analyze µm-sized individual objects.

6 Analysis of structure and composition of an individual (In,Ga)N/GaN rod side-facet

The previous chapter has been concluded with the determination of the In content in (In,Ga)N/GaN rods which remains an ongoing challenging task. Furthermore, nanofocus x-ray diffraction has proven to be a highly suitable technique to access the local strain field in individual side-facets of core-shell micro-rods. The thereby observed strain gradient has been attributed to fluctuations of the chemical composition. However, if structural inhomogeneities of the core-shell structure are significant they also have to be considered for determining the In content. Especially, the QW width is of particular importance as it represents an additional parameter which alters the strain state and, thus, can be used to engineer the band gap [92, 185]. Consequently, next to a homogeneous In distribution it is important to control the QW width during the fabrication process. A direct imaging of structural parameters is possible using, e. g., high-angle annular dark-field scanning transmission electron microscopy (HAADF STEM). Here, however, the sample preparation is destructive and the field-of-view limited.

This triggers the idea of combining nanofocus x-ray diffraction and reflectivity. If both experiments are performed on the same side-facet of an individual rod at the very same position it should be possible to correlate the strain measured by x-ray diffraction and the structural parameters obtained via x-ray reflectivity. If the structural parameters are well known they can serve as input for constructing a model of the rod within the FEM approach. With the prerequisite of purely elastic strain relaxation and a homogeneous distribution of In atoms, the In content then remains the only free parameter to tune the strain state. This can be exploited to fit subsequently performed kinematic scattering simulation to the experimental data and, thereby, to determine the In content with a significantly improved accuracy.

Building up on the experiments presented in chapter 5, this chapter deals with the investigation of a two-fold (In,Ga)N QW embedded into a GaN matrix in a core-shell micro-rod geometry. At distinct positions on one individual side-facet, nanofocus x-ray diffraction and reflectivity experiments are performed in order to analyze the structure and chemical composition of the side-facet with spatial resolution. The results are interpreted by comparing the experimental data to kinematic scattering simulations based on the strain induced deformation field computed using the FEM. Furthermore, results from HAADF STEM measurements which have been performed on a series of rods from the very same sample complement the synchrotron experiments. Parts of this chapter have been published in Ref. [186].

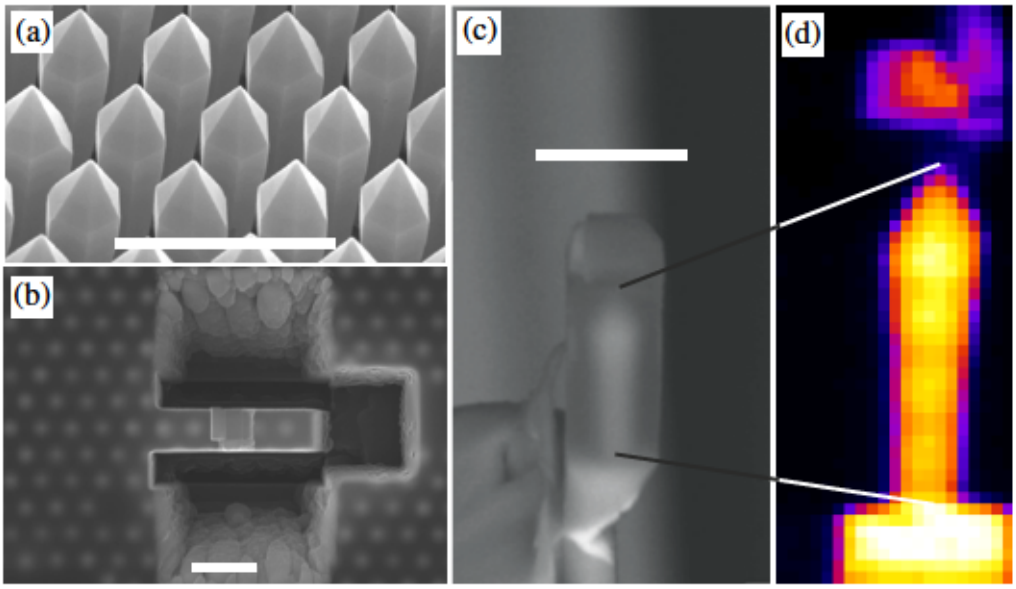

Figure 6.1 Scanning electron microscope micrograph of the as-grown (In,Ga)N/GaN core-shell micro-rods (a). Before focused ion beam preparation the rods have been embedded into polymer glue. To isolate a lamella, trenches are cut as seen in (b). Finally, the isolated rod is mounted on a Cu grid (c). In (d) the Ga Kα_1 fluorescence is shown in a map recorded by scanning the nanofocus x-ray beam over the sample. On top of the glue (about 2 µm above the rod) a Ga droplet resulting from focused ion beam preparation can be observed. The white scale bar refers to a length of 5 µm.

6.1 Growth and sample preparation of (In,Ga)N/GaN micro-rods

The (In,Ga)N/GaN core-shell micro-rods comprise an n-doped GaN core surrounded by two 5 nm thick (In,Ga)N QWs with an intended In content of about 30 %. In between the double quantum well (DQW), a GaN barrier of 5 nm is grown and a p-doped GaN shell of 100 nm surrounds the DQW. The rods are grown by selective area metalorganic vapor phase epitaxy (MOVPE) in a close-coupled showerhead reactor under continuous growth mode[1]. The template consists of a 30 nm thick SiO_x mask on a GaN buffer layer on [0001]-oriented sapphire. Holes in the dielectric mask are produced by photolithography and reactive ion etching by inductively coupled plasma. These holes have diameters of 800 nm defining the width of the GaN core and are arranged in a hexagonal pattern with a pitch of 2.4 µm determining the rod distribution as shown in Fig. 6.1(a). The template has been heated up in the reactor under N_2 carrier gas. Then, a short growth step under high V/III ratio of 1000 and under H_2 carrier gas is performed to start the growth of the GaN cores in the hole openings. Subsequently, the 3D-growth-step of the micro-rods is carried out under low V/III ratio of 77 and a SiH_4 flow of 37 nmol/min for an n-type doping and an increased vertical growth rate [187, 188]. The temperature during this 20 min

[1]The investigated micro-rods are grown by the group of Prof. Dr. A. Waag (TU Braunschweig).

long step has been held at 1060 °C. The shell growth steps are again conducted at a high V/III ratio: Starting with a low- and high-temperature GaN spacer layer, continuing with two QWs which are separated by a GaN barrier and terminating with several Mg-doped GaN layers for p-type doping. Both QWs are grown at a real temperature of 690 °C. After the growth, an in-situ annealing has been performed for 10 min at 770 °C in order to activate the Mg dopants.

Using a Ga^+ FIB, a single rod is extracted from the sample[2]. To protect the rod from Ga implantation, the sample is embedded in epoxy glue diluted with acetone to reduce the viscosity. With a carbon depot on top, the conductivity is increased such that charging of the sample is alleviated. In a first step, trenches are cut next to the lamella as seen in the SEM micrograph shown in Fig. 6.1(b). With a manipulator needle, the lamella containing several rods is lifted out and mounted on a copper grid commonly used for transmission electron microscopy experiments [cf. Fig. 5.2(c)]. In a series of final fine-polishing steps, the investigated rod shown in Fig. 6.1(c) is isolated and cleaned from re-deposited GaN crystallites [182]. The FIB preparation ensures that the detected x-ray scattering signal stems from the single object, only, and that it is not superimposed by potential neighbors.

6.2 Experimental setup at beamline P06

To investigate the local strain field in nm-sized structures one usually relies on highly specialized nanofocus x-ray diffraction setups available at 3rd-generation synchrotrons. The data presented in this chapter have been recorded at the nanoprobe beamline P06 at PETRAIII at DESY in Hamburg, Germany [139], where a focus size of $80\times90\,nm^2$ is reached using nanofocusing refractive x-ray lenses as introduced in section 2.6. With an additional pre-focusing lens a photon flux of about 10^9 photons/sec is generated at a photon energy of 17 keV.

Figure 6.2 shows photographs taken at different perspectives of the experimental hutch of beamline P06. On the right hand side in (a), the vacuum pipe through which the x-ray beam enters the experimental hutch is visible. The case in the middle of the photograph hosts the sample environment. Everything is mounted on a massive block of granite to minimize the influence of vibrations. Upon a separate block of granite, the detector table is placed. In the presented photographs, the detector is positioned at a distance of 2 m with a scattering angle of about 16 ° which corresponds to two times the Bragg angle of the GaN $(10\bar{1}0)$ reflection at 17 keV. All x-ray diffraction data presented in this chapter are recorded using a PILATUS 300K 2D-area detector. This detector comprises a pixel size of $172\times172\,\mu m^2$ with a dynamic range of 20 bits and a format of 487×619 pixels [189]. In (b) the optical microscope is visible which is used for pre-aligning the sample in the focus point of the x-ray beam. Moreover, from this angle of view a first impression of the sample environment can be gained. The latter is once again visible in an enlarged photograph in (c). As described in

[2]The FIB preparation has been performed by Dr. M. Niehle (Paul-Drude-Institut Berlin).

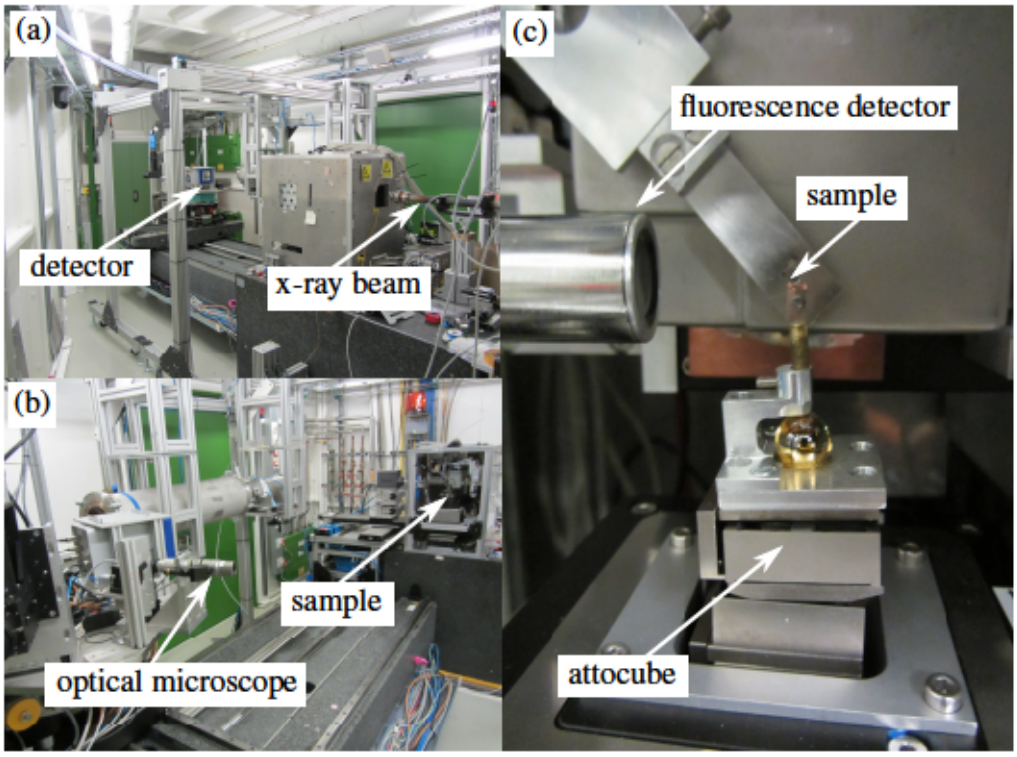

Figure 6.2 Different views of the experimental hutch at beamline P06 at PETRAIII, DESY. In (a) the vacuum pipe can be seen through which the x-ray beam enters the experimental hutch. The 2D-detector is positioned 2 m away from the sample which is mounted inside the box on the detector table visible on the right in (b). Next to the area-detector a pin diode and an optical microscope are used. In (c) an enlarged view of the sample environment is shown. As at beamline ID13 the scanning is performed by an attocube [cf. section 5.2]. A sample holder made of brass holds the copper grid on which the single micro-rod is mounted. The fluorescence detector left of the detector window is used for positioning the x-ray beam on the micro-rod.

section 5.2, the sample holder is made of brass and the copper grid on which the single rod is mounted is clamped by a metal plate. The scanning is performed with an attocube which contains several piezo-motors. In contrast to the setup at ID13 there is no hexapod to compensate tilting of the sample, however, as visible in (c) within the range of several degrees this could be done directly with the attocube. As a consequence, the motor movements in the experiments are done using virtual axis. On the left, the detector window of a vortex fluorescence detector is visible which is used for positioning the x-ray beam on the rod.

6.3 X-ray diffraction with sub-100 nm spatial resolution

In a first step, an optical microscope is used to align the sample in the focus point of the x-ray beam which was found via a ptychographic reconstruction of a Siemens star. For a more accurate positioning of the beam on the rod-facet, x-ray fluorescence is employed. A Ga Kα_1 fluorescence intensity map of the rod is shown in Fig. 6.1(d) and Fig. 6.3(a). In the latter image, two dashed lines are

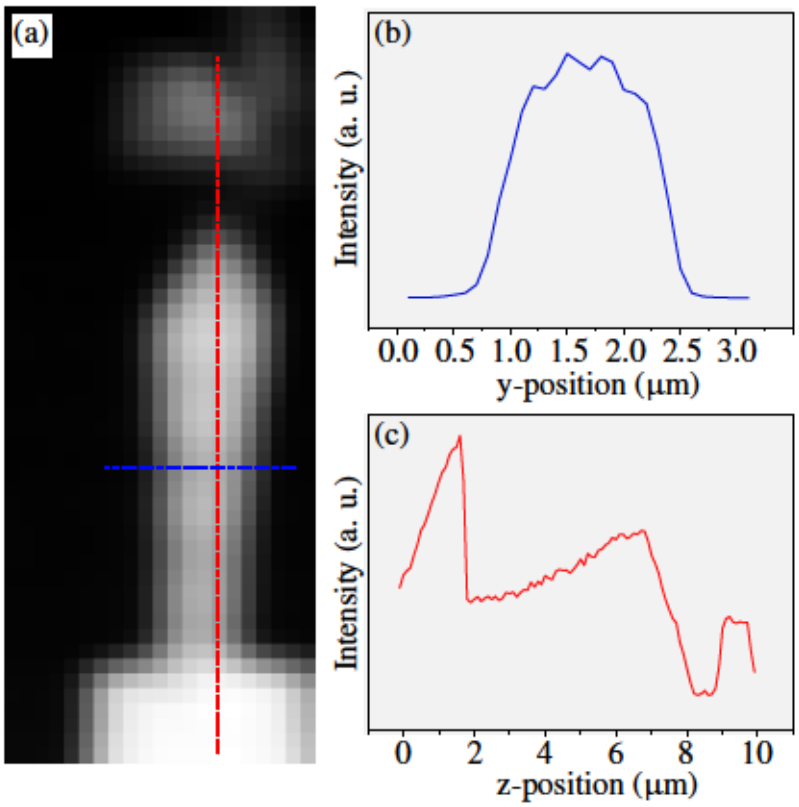

Figure 6.3 In (a), a spatially-resolved map of the Ga Kα_1 fluorescence intensity is shown. The blue dashed line indicates the direction along which the line profile shown in (b) is recorded (step size 100 nm) and reveals the horizontal profile of the rod from which a diameter of about 1.4 μm can be retrieved. In (c) the Ga Kα_1 fluorescence intensity is shown as a function of the rod height as indicated by the red dashed line in (a). The highest detected intensity between 0 and 2 μm is attributed to the GaN buffer layer. Between 2 and 8 μm extends the micro-rod. The peak between about 9 and 10 μm corresponds to a Ga droplet which is deposited on top of the glue during FIB preparation.

drawn which indicate how the x-ray beam has been positioned on the rod. In Fig. 6.3(b) a line profile of the Ga Kα_1 fluorescence intensity is shown which is recorded along a horizontal line over the rod as indicated by the blue dashed line. With the applied step size of 100 nm a rod diameter of about 1.4 μm can be retrieved. Furthermore, the red dashed line shown in (a) results in the line profile in (c) of the Ga Kα_1 fluorescence intensity as a function of the rod height. The rods are grown on a GaN buffer layer explaining the high intensity from 0 to 2 μm followed by the rod itself which extends from 2 to 8 μm. Here, from about 7 to 8 μm, one can see the rod tip. Consequently, the overall height is about 6 μm. Between about 9 to 10 μm again higher intensity is detected which originates from the Ga droplet which has been deposited on top of the glue during FIB preparation. A first interesting observation is an increasing intensity along the rod length from bottom to top. This indicates that there is less material at the bottom compared to the top part and fits to the observation of an increasing rod diameter from bottom to top as seen with SEM. Based on line scans comparable to (c) the vertical position of the x-ray beam on the rod has been determined

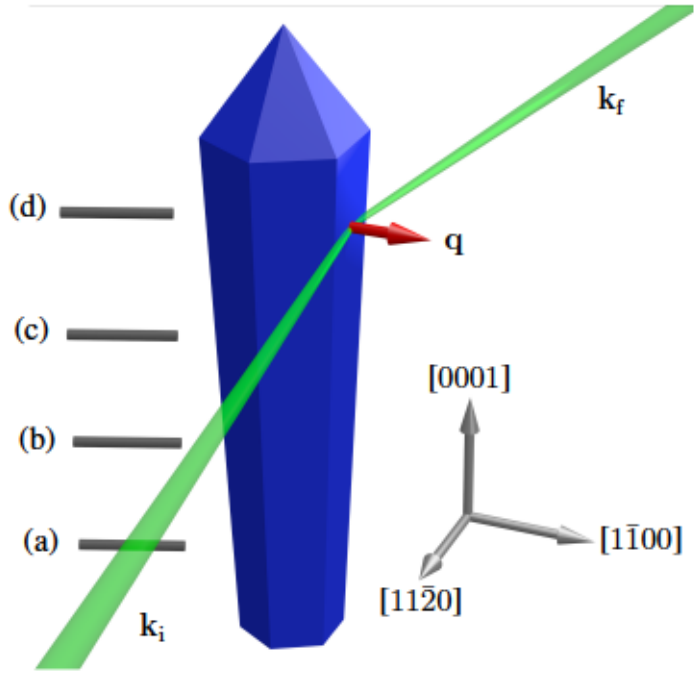

Figure 6.4 Sketch of the applied diffraction geometry. To investigate the strain field normal to the m-plane facet the hexagonal (1$\bar{1}$00) reflection was measured. The diffraction plane lies parallel to the substrate surface and is spanned by the incoming beam $\mathbf{k}_i$ and the diffracted beam $\mathbf{k}_f$, defining the scattering vector $\mathbf{q} = \mathbf{k}_f - \mathbf{k}_i$. The measurements were performed at four heights labeled with (a), (b), (c), and (d). These labels refer to all in the following presented data.

whereas horizontal line scans as shown in (b) are used to position the x-ray beam on the side-facet. Here, the inflection point, e. g., on the right side of curve (b) has been chosen.

To access the strain normal to the m-plane facet, which is the hexagonal $\langle 1\bar{1}00\rangle$-direction, nanofocus x-ray diffraction experiments are conducted on the $\{1\bar{1}00\}$ lattice planes. The measurements are performed at four positions labeled with (a), (b), (c), and (d) separated by about 1 µm on one individual side-facet of the isolated rod as sketched in Fig. 6.4. All data shown in the following will be labeled accordingly such that they can be directly identified with these four heights. At these positions rocking curves are performed over 4 ° around the GaN (1$\bar{1}$00) Bragg reflection with an angular resolution of 0.01 °. At each height, the scans are repeated at several horizontal positions to ensure that actually a position directly on the facet has been measured. Due to the fact that the outer facet is not perpendicular to the substrate but inclined, it is necessary to realign the sample with respect to the x-ray beam for each position individually. This has been done as described within Fig. 6.3.

On the very same positions (a) to (d) on the rod, nanofocus x-ray reflectivity measurements are performed. Here, the primary beam is reflected at the interfaces of the core-shell structure within one side-facet. Therefore, the rod has been turned by 2.5 ° starting at -0.5 ° in steps of 0.01 °. For planar system one would expect to detect no intensity below 0°. However, due to the small size of

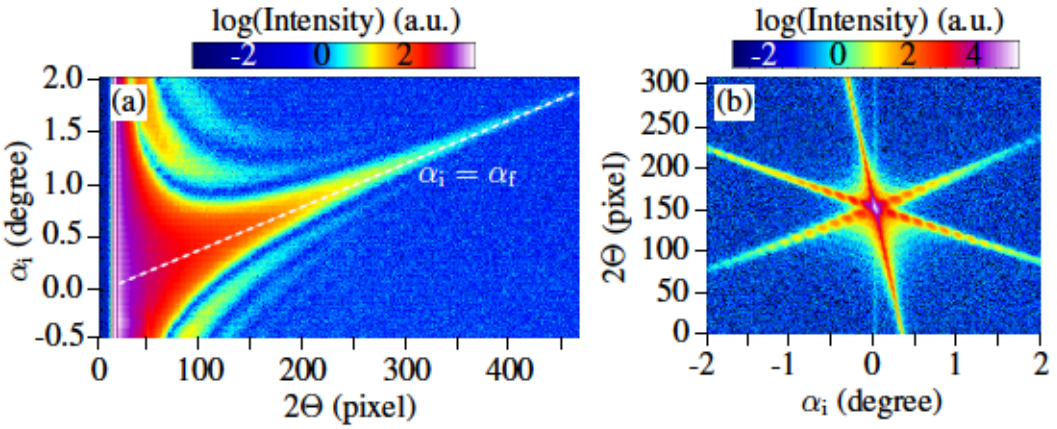

Figure 6.5 Two-dimensional maps of the scattered intensity as a function of incident and scattering angle. In (a) a representative map of the reflected intensity recorded at the lowest position in Fig. 6.4 can be seen. Next to the intense streak at $\alpha_i = \alpha_f$, reaching from the bottom left to the top right, satellites can be observed. In (b), the diffusely scattered intensity around the GaN $(1\bar{1}00)$ reflection reveals the shape function of the hexagonal rod cross-section in form of CTRs which are modulated by finite-size oscillations.

the rod, a reflected beam is also detected in Laue geometry ($\alpha_i < 0$). To increase the resolution, the detector is placed 2 m behind the sample in the direction of the primary beam which is blocked by a beam stop. It is important to note, that the scattering plane for both, the diffraction and the reflection geometry, remains the same and contains the facet normal such that Fig. 6.4 applies to both cases.

6.4 Data evaluation

During a nanofocus x-ray diffraction scanning experiment at one position on the rod, a data set comprising 400 detector frames is produced. As described in the previous section such a data set is angular-resolved with respect to the incident angle α_i, here, in steps of 0.01 °. Similar to section 5.4, the data processing is done using a specifically developed source code for the open source software package ImageJ. For the series of detector frames a ROI is defined around the Bragg reflection comparable to ROI 2 in Fig. 5.5(a) and the intensity within this ROI is summed up vertically for each horizontal pixel position. Here, the integration over 5 pixels corresponds to an integration over approximately 0.001 $Å^{-1}$ in vertical direction. The resulting line profiles correspond to the integrated intensity of each detector frame and can be used to construct a 2D map of the scattered intensity as a function of the incident angle α_i and the scattering angle 2Θ. As described in section 5.4, by employing Eqs. 5.4.1 and 5.4.2, the intensity maps are transformed into reciprocal space coordinates for interpreting the experimental results.

Figure 6.5 shows two representative maps of the scattered intensity as a function of incident and scattering angle which are reconstructed from line profiles of angular-resolved scanning experiments. In Fig. 6.5(a) the result of a representative nanofocus x-ray reflectivity experiment is shown which is recorded at

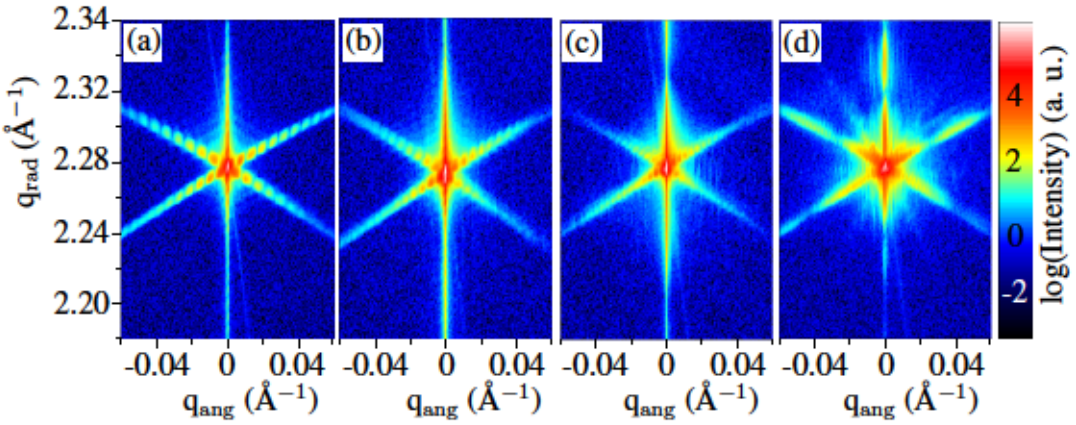

Figure 6.6 Reciprocal space maps of the diffusely scattered intensity in logarithmic scale around the GaN (1$\bar{1}$00) reflection. The maps are recorded at four positions (a), (b), (c), and (d) as sketched in Fig. 6.4 on one individual facet. Along the angular direction the shape function of the rod is visible in form of a six-armed star. The crystal truncation rods are modulated by the shape function related to the structural parameters of the illuminated volume. The radial direction is sensitive to the strain induced by the two (In,Ga)N quantum wells.

height (a). The high intensity streak reaching from the bottom left to the top right is the reflected x-ray beam at $\alpha_i = \alpha_f$ and is expected to hold information about structural parameters of the core-shell geometry. An interesting feature are the satellites next to the main streak which will be subject to the following discussion. In Fig. 6.5(b), a map of the diffusely scattered intensity around the GaN (1$\bar{1}$00) reflection is shown. Here, the shape function of the hexagonal rod cross-section is clearly visible in form of a six-armed star.

6.5 Results and discussion

Figure 6.6 shows the diffusely scattered intensity around the GaN (1$\bar{1}$00) reflection in reciprocal space. In radial direction (q_{rad}), the (1$\bar{1}$00) reflection is sensitive to the strain normal to the m-plane facet. Hence, it directly measures the deformation of the {1$\bar{1}$00} lattice planes induced by the lattice mismatch between the (In,Ga)N DQW and the surrounding GaN matrix. Consequently, the diffraction profile along q_{rad} offers a way to quantify the In content incorporated in the DQW.

In angular direction (q_{ang}) the reflection is sensitive to the hexagonal rod geometry. The rods shape function shows a six-armed star and along each of the six CTRs, oscillations are visible containing direct information about the structural parameters of the illuminated volume. The fact that many oscillations are present, see in Fig. 6.6(a), originates from the high crystal quality of the illuminated volume in combination with the small focus of the x-ray beam corresponding to averaged information of a comparatively small volume. Such details could only be resolved in ensemble measurements if all scattering objects would be perfectly identical [190].

The labels (a), (b), (c), and (d) in Fig. 6.6 correspond to the rod heights as

FEM simulation parameters				
Position	(a)	(b)	(c)	(d)
GaN shell (nm)	90	110	170	270
GaN barrier (nm)	4	6	6	16
(In,Ga)N QWs (nm)	4	4	5	9
Facet width (nm)	650	700	750	850
In content (%)	6	10	22	18

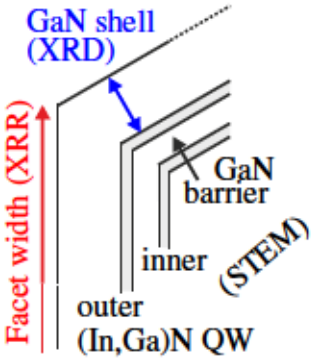

Table 6.1 Structural parameters and In content used to model the deformation field within a finite element approach. Parameters in blue are retrieved from nanofocus x-ray diffraction (XRD). The facet widths written in red are obtained from x-ray reflectivity (XRR) experiments [cf. Fig. 6.8]. Structural parameters shown in black are geared to the STEM measurements presented in Fig. 6.11. These values are taken at positions where the identical GaN shell thickness is obtained [cf. Fig. 6.4]. By fitting the kinematic scattering simulations to experimental data shown in Fig. 6.7, the local In content is retrieved. The adjacent sketch illustrates the respective structural parameters and the method by which they are obtained.

sketched in Fig. 6.4. Obviously, the shape functions for all four heights look different indicating a strong structural inhomogeneity along the height of the investigated facet. For example, it is obvious that the periodicity along the CTRs increases with increasing height. These Kiessig fringes are the Fourier transform of the shell sequence in the side-facet. In fact, the retrieved thickness values ($d = 2\pi/\Delta q$) are related to the width of the outer GaN shell surrounding the DQW and, interestingly, an increase in thickness towards the tip by a factor of three is observed. Moreover, Fig. 6.6(d) shows larger periods modulating the CTRs which refer to a thickness of about 16 nm. A comparison to STEM measurements presented in the following indicates that these oscillations are related to the GaN barrier. All structural parameters retrieved from x-ray diffraction experiments are shown in blue in Tab. 6.1 and serve as structural input for subsequent FEM simulations.

Based on the structural parameters presented in Tab. 6.1, the strain induced linear elastic deformation inherent to the rod is simulated for positions (a) to (d) employing the FEM. The values for DQW and GaN barrier thicknesses for models (a), (b), and (c) are geared to the STEM measurements given in Fig. 6.11. As these values are in a range of only a few nanometer they result in comparatively large periods along the CTRs in x-ray diffraction patterns. Due to the applied scan range, it is not possible to resolve these oscillations in the presented data [cf. Fig. 6.6]. Additionally, different facet widths are implemented for all four positions which are shown in red in Tab. 6.1. These values are deduced from nanofocus x-ray reflectivity experiments presented in Fig. 6.8 which are performed at the very same heights as sketched in Fig. 6.4. For modeling the mechanical properties of the materials, the elastic constants for GaN and InN given in Ref. [152] are used and the ones for the $In_xGa_{1-x}N$ alloy are interpo-

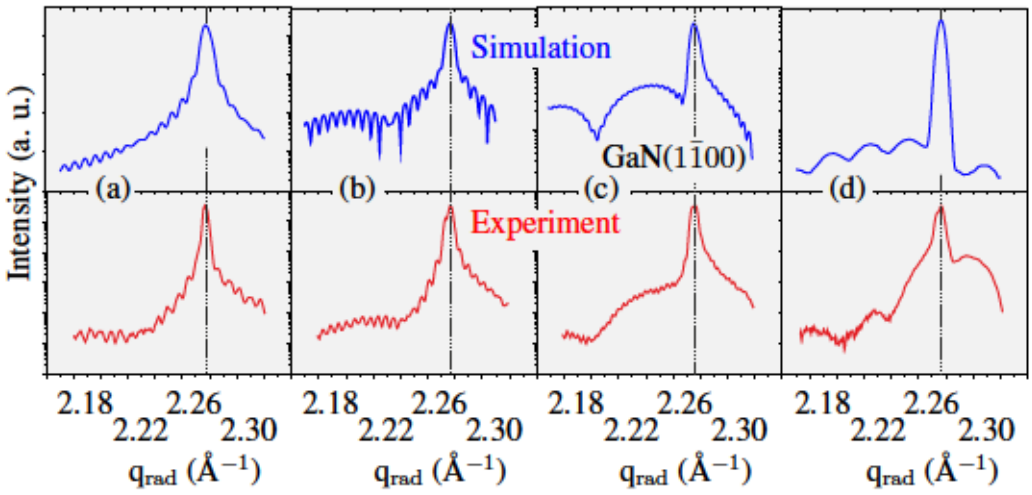

Figure 6.7 Simulated (top) and experimentally measured (bottom) line scans along q_{rad} of the intensity in logarithmic scale through the GaN (1$\bar{1}$00) reflection. Each column labeled with (a), (b), (c), and (d) refers to one height position on the rod, see Fig. 6.4. The experimental line scans are extracted from Fig. 6.6. The simulated line scans are computed using kinematic scattering theory based on the deformation field retrieved from finite element method calculations taking into account of the parameters given in Tab. 6.1.

lated linearly using Eq. 2.1.4, where x is the In content.

The retrieved deformation field, $\mathbf{u}$, induced by the DQW is used to compute the displacement $\mathbf{u}(\mathbf{r})$ of the atomic positions $\mathbf{r}$ of the wurtzite GaN crystal. The atomic coordinates and their displacement enter the subsequent kinematic scattering simulations which are applied to compute the scattered intensity in reciprocal space around the GaN (1$\bar{1}$00) reflection. In order to mimic the situation of the nanofocus x-ray diffraction experiment, a Gaussian beam profile is appended to the kinematic sum [cf. Eq. 5.5.2]

$$I(\mathbf{q}) \propto \left| \sum_i \frac{e^{-(r_{i,x}-\mu)^2/2\sigma^2} e^{i\mathbf{q}\cdot(\mathbf{r}_i+\mathbf{u}(\mathbf{r}_i))}}{\sqrt{2\pi}\sigma} \right|^2 \tag{6.5.1}$$

such that it is possible to define beam position, μ, and FWHM via σ. This allows to compute the scattered intensity I as a function of the scattering vector $\mathbf{q}$ originating from a distinct volume of the rod. Due to the comparatively small size of the illuminated rod volume, it is justified to neglect multiple scattering events of a single photon such that the kinematic plane wave approach remains valid [76].

Figure 6.7 displays line scans along q_{rad} around the GaN (1$\bar{1}$00) reflection. For each height a simulated line profile (top) based on the FEM and the according experimental scan (bottom) extracted from Fig. 6.6 at $q_{ang} = 0$ is shown. All experimental line profiles look very characteristic and contain distinct features of the illuminated volume. The FEM simulations suggest that most parts of the wire comprise relaxed GaN and, indeed, all line profiles show a strong peak at the expected position of relaxed GaN at $q_{rad} = 2.277\,\text{Å}^{-1}$. Furthermore, fine oscillations which modulate the line profiles refer to the shape function of the outer GaN shell and reveal a clear trend to higher periodicity from Fig. 6.7(a)

to (c) indicating an increase of the outer GaN shell thickness. Underlying the fine oscillations, broader oscillations are present whose frequency also increases towards the top.

All simulated profiles are computed using kinematic scattering theory by applying Eq. 6.5.1, where a beam width of 90 nm is assumed and in all cases the beam maximum is positioned in the middle of the DQW. The displacement field of the atomic positions serves as input for the scattering simulation which were obtained via interpolation with the displacement field computed using the FEM. Hence, the parameters applied for the FEM simulation [cf. Tab. 6.1] can be used to fit the simulated line profile to the experimental data.

The broader oscillations are sensitive to the superposition of GaN barrier and DQW which define the distance between two minima. A variation of the In content mainly shifts the minima position along q_{rad}. At positions (a) and (b), the GaN barrier and DQW thickness have a stronger impact on the peak shape and the In content mainly changes the amplitude of the oscillations. In cases (c) and (d), a change of the In content has a greater impact on the position of the minima. While the simulations describe the experimental data very accurately in (a) and (b), there is an increasing discrepancy visible in (c) and (d). This observation can be attributed to the presence of structural inhomogeneities, such as the onset of plastic relaxation towards the top. Concerning the sensitivity of the simulated line profiles it is worth mentioning that a variation of the In content of $\pm 1\,\%$ as well as a thickness variation of ± 1 nm of QW or barrier has a clearly visible impact. Moreover, it is important to note that the better the structure of the rod is known the more accurate the In content can be determined via FEM simulations which of course demands that relaxation occurs purely elastic.

From STEM measurements [see Fig. 6.11] performed on a representative rod from the same sample, it is possible to estimate the GaN barrier and QW thicknesses shown in black in Tab. 6.1. Hence, the only free remaining parameter in the FEM simulations is the In content. Consequently, within the framework of linear elasticity theory it is possible to determine the In content with comparatively high accuracy. The obtained values for the In content at the four heights are given in the bottom row of Tab. 6.1 and show a significant increase towards the tip by almost a factor of 4 from position (a) to (c).

Interestingly, for fitting the simulated line profile at position (d) (just below the tip) to the according experimental data it is necessary to assume a smaller In content of only 18 % compared to position (c). This means that elastic deformation is reduced again after a certain height. However, from previous studies of comparable samples a further increase of the In content to the top is expected [191]. The origin of this decrease is found by STEM investigations showing a strong increase of plastic relaxation in the top region most probably due to a higher In content and, thus, a larger lattice mismatch which cannot be compensated by purely elastic relaxation. Here, the crystal quality is significantly reduced compared to the bottom part of the rod [see Fig. 6.11].

Plastic relaxation is not included in the simulations and demands a critical interpretation of the obtained values for the In content. But, if two mechanisms of

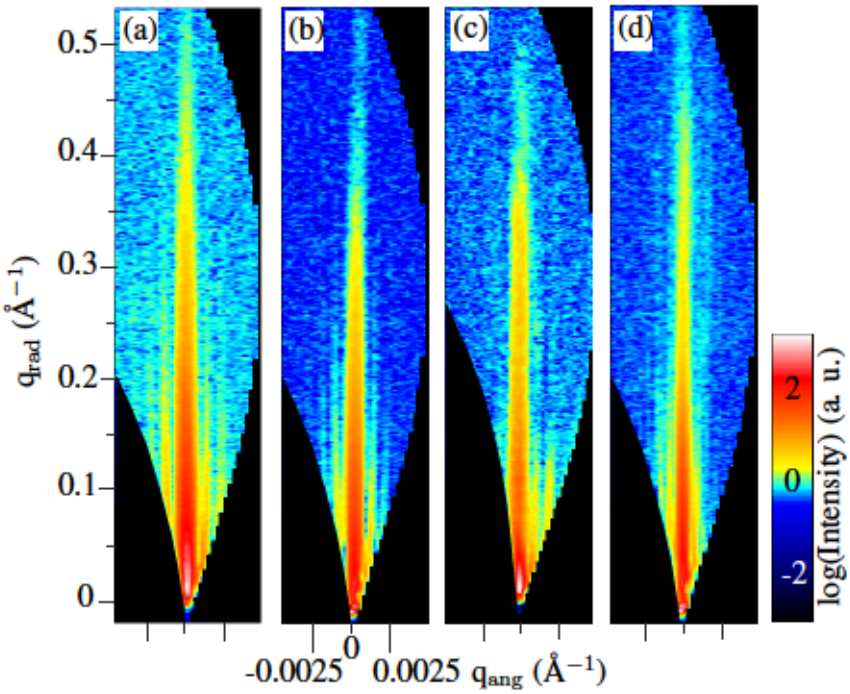

Figure 6.8 Reciprocal space maps of the reflected intensity in logarithmic scale. The labels (a), (b), (c), and (d) refer to the heights sketched in Fig. 6.4. In q_{ang}-direction satellites next to the CTR are visible whose periodicity refers to the facet width.

strain relaxation are present at the same time, namely plastic and elastic relaxation, the simulation, which considers only the elastic part, is expected to give a lower estimate of the In content. Moreover, the clear trend of a significant gradient in the In content towards the tip is observed in both approaches and the values given in Tab. 6.1 are comparable to the values retrieved by STEM [cf. Fig. 6.11].

In addition to nanofocus x-ray diffraction, nanofocus x-ray reflectivity measurements are performed on the heights as sketched in Fig. 6.4. Figure 6.8 shows experimentally retrieved nanofocus x-ray reflectivity maps in reciprocal space recorded at the very same positions (a), (b), (c), and (d). Next to the main CTR, lateral satellites are visible in q_{ang}-direction. The distance between subsequent minima along q_{ang} refers to the width of the illuminated facet. As expected from the above presented structural investigations of the rod, a decrease of the spacing between the satellites is observed translating to an increase of the facet width by about 200 nm from position (a) to (d). Accordingly, the rod diameter increases from 1.3 to 1.7 µm. These values are comparable to SEM investigations of similar rods of the same sample and enter the FEM simulations with the values given in red in Tab. 6.1.

Along q_{rad}, the high intensity streak at $q_{ang} = 0$ is expected to reveal structural information about the DQW and the GaN barrier thickness. However, for several reasons the data evaluation has shown to be a challenging task. First, the intensity of the reflected signal decreases by more than five orders of magnitude within several degrees. Second, the decreased crystal quality due to defects in the top region of the rod leads to non-sharp crystal interfaces between (In,Ga)N

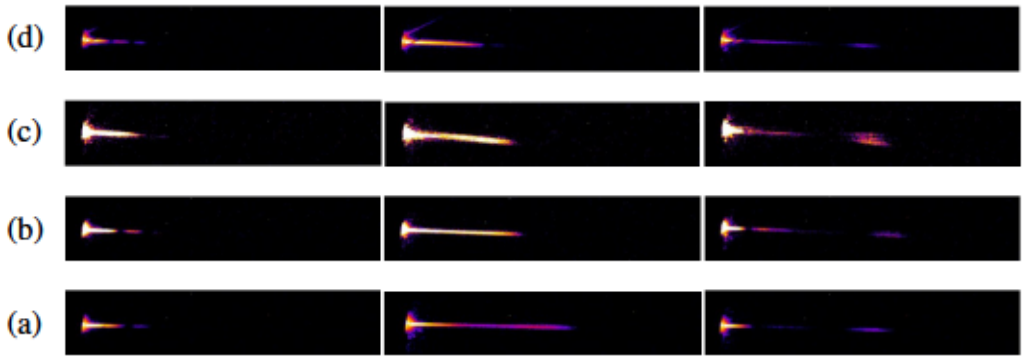

Figure 6.9 Selected specular reflections at different incident angles are shown. The labels (a) to (d) correspond to the positions in Fig. 6.4 and the three columns represent qualitative snapshots at different angles α_i of the incident beam within the interval $[0\,°, 2\,°]$. All reflected streaks are inclined downwards with respect to the scattering plane, whereas in (a) this effect is the weakest and in (c) the strongest. Moreover, in the third column of line (c) it is clearly visible that the specular beam splits into three parts. Most probably this observation arises form the fact that the interfaces between the shells are inclined to each other. Moreover, at the top height (d) a streak resulting from the r-plane facets at the tip can be seen.

and GaN regions. Moreover, the different parts of the rod, i. e., shell, barrier and DQW are all inclined by several degrees such that up to three reflected streaks are observed deviating by up to 5° from the diffraction plane. Exemplary, this can be seen in Fig. 6.9. Here, the labels (a) to (d) correspond to the positions in Fig. 6.4 and the three columns represent snapshots at different angles α_i of the incident beam within the interval $[0\,°, 2\,°]$. In the first column the incident angle is small, in the second intermediate and in the third column the incident angle is the largest. All specular reflections are inclined downwards from the scattering plane. Moreover in the third column at position (c) the specular beam clearly splits into three separate streaks indicating that the x-ray beam is reflected from interfaces which are inclined by several degrees with respect to each other. Additionally, kinematic scattering simulations reveal that the intensity profile is highly sensitive to the beam position on the rod such that also non-exact positioning of the x-ray beam might play a role. However, the missing structural parameters could be retrieved using HAADF STEM which will be discussed in the following.

As described in Ref. [186], HAADF STEM is employed[3] to investigate the chemical composition of several rods from the same sample as the rod investigated by nanofocus x-ray diffraction. Hence, the experimental results of both methods are directly comparable within the range of inhomogeneity of the sample. Using the FIB as outlined in section 6.1, a lamella containing several rods has been isolated. The rods in the lamella are aligned in a way that an m-plane faces its neighbor's m-plane so that a projection onto the $\{11\bar{2}0\}$ lattice planes is possible. The lamella is further thinned by FIB to get rid of the inclined m-facets. Thus, in a cross-section STEM experiment, the electron beam is directed along

[3]The HAADF STEM measurements have been conducted by M.Sc. L. Nicolai (Paul-Drude-Institut Berlin).

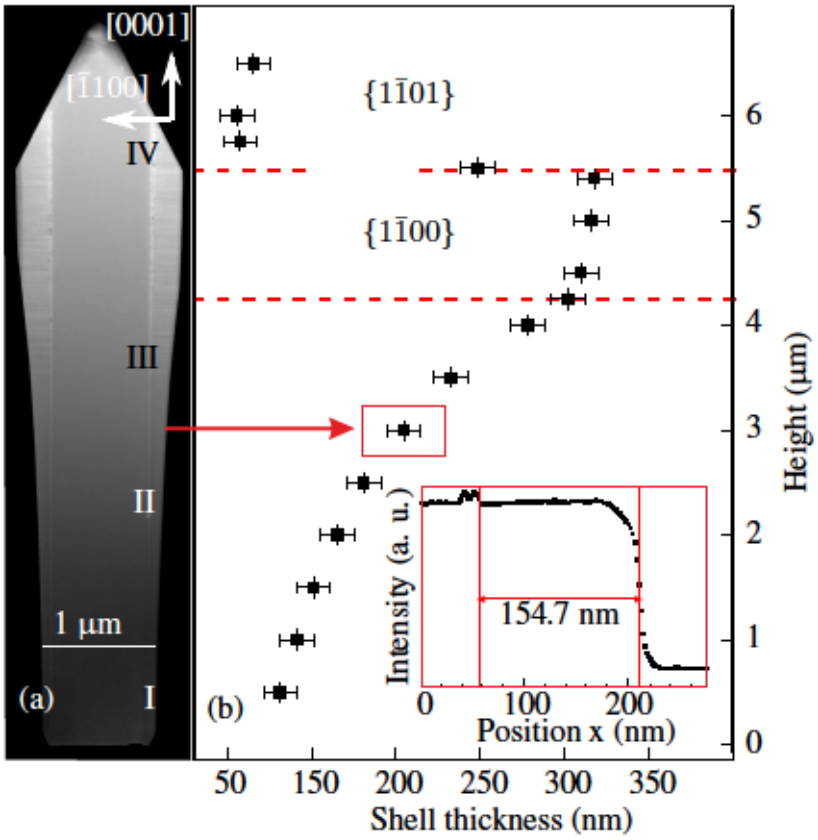

Figure 6.10 (a) HAADF STEM cross-section micrograph of the (In,Ga)N/GaN rod recorded along the [11$\bar{2}$0]-direction. The four positions I, II, III, and IV refer to a detailed STEM analysis [cf. Fig. 6.11]. (b) The thickness of the outer GaN shell on the right side of the rod as a function of the height. The inset in (b) gives an example of how the intensity profile was used to determine the shell thickness. The presented case refers to a height indicated by the red arrow in (a) resulting in the data point marked with a red box in (b). Between the horizontal dashed red lines the shell thickness approaches a constant value.

the DQW in two opposing m-facets.

Figure 6.10(a) displays a HAADF STEM cross-section micrograph of a representative individual rod. It shows that the GaN core thickness remains constant. However, the outer GaN shell thickness increases drastically. To quantify the thickness gradient, horizontal line profiles with an integration width of 100 nm of the HAADF intensity are taken at different rod heights. Exemplary, the inset in Fig. 6.10(b) shows that the thickness is obtained by measuring the distance between the peak originating from the outer QW and the turning point of the intensity profile. The inset intensity profile is taken at a height of 3 µm (marked with the red arrow) and results in the data point marked with a red box. Following this procedure, Fig. 6.10(b) provides the shell thickness as a function of rod height. It is clearly visible that the shell thickness increases drastically from about 80 nm to about 270 nm from bottom to top. Interestingly, above approximately 4.2 µm the shell thickness approaches a constant value and actually m-facets are formed. Due to the formation of a tip with {1$\bar{1}$01} facets the shell thickness decreases above the second dashed line. The values fit very well to

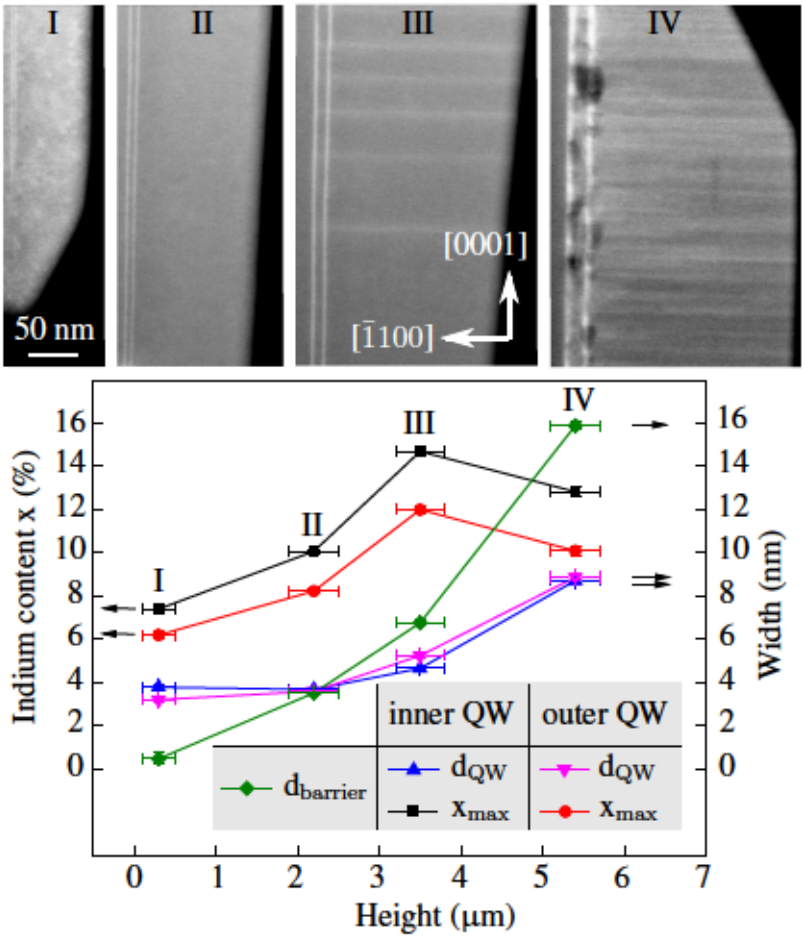

Figure 6.11 (top) HAADF STEM micrographs at position I-IV as displayed in Fig. 6.10. The scale bar applies to all four micrographs. At positions III and IV, stacking faults are visible which run horizontally from quantum wells (vertical bright stripes) towards the GaN shell surface. By fitting the quantum well peak intensity, the quantum well thicknesses, d_{QW}, the GaN barrier thickness $d_{barrier}$ and the In composition x_{max} could be extracted. Their evolution with respect to the rod height is shown in the bottom graph.

the shell thicknesses obtained from nanofocus x-ray diffraction measurements and substantiate the comparability of both results. Especially in the top region, both methods yield almost identical values. By comparing the shell thicknesses obtained by nanofocus x-ray diffraction with the values retrieved by STEM [cf. Fig. 6.10] it is possible to precisely correlate positions (a) to (d) to the actual heights. Moreover, it allows to deduce the missing structural parameters [i. e. DQW and barrier thickness] for the FEM simulations which could not be obtained from nanofocus x-ray diffraction and reflectivity experiments.

At positions I-IV marked in Fig. 6.10(a), HAADF STEM micrographs with higher magnification have been taken in order to quantify the evolution of QW and barrier thickness as well as the In content. The respective micrographs are shown in Fig. 6.11(top). As the scale bar applies to all four micrographs, it is clearly visible that both, the DQW and the barrier increase in thickness. Moreover, at positions III and IV stacking faults run horizontally from the DQW to-

wards the GaN shell surface. Furthermore, at position IV the crystal quality is significantly reduced.

Intensity line profiles with an integration width of about 180 nm have been taken for positions I-IV and sigmoidal functions are used to fit the (In,Ga)N QW intensity peaks to determine the FWHM which is interpreted as the QW thickness. The distance between the QW peak positions subtracted by half of the width of each peak results in the GaN barrier thickness. The result is shown in Fig. 6.11(bottom). Following the trend of the outer GaN shell both DQW and barrier show a significant increase of their thickness from bottom (position I) to top (position IV). Up to approximately the middle of the rod the QW thickness remains constant at about 4 nm. However, between positions III and IV the thickness almost doubles. An even stronger increase in thickness is observed for the GaN barrier. Starting at about 1 nm, the barrier thickness increases up to 16 nm. The nanofocus x-ray diffraction experiment performed at the highest position [cf. Fig. 6.6(d)] shows broad oscillations along the CTRs referring to a thickness of also 16 nm. Hence, we can attribute these oscillations to the GaN barrier. Interestingly, despite the fact that the GaN barrier increases drastically both inner and outer QW show very similar thicknesses over the full height. In addition, as described in Ref. [186], the contrast of the (In,Ga)N to GaN could be used to estimate the alloy composition. The result in Fig. 6.11(bottom) shows a significant increase along the rod height comparable to the result of the nanofocus x-ray diffraction analysis. However, in the region where plastic relaxation sets in and voids are visible (position IV) the approach looses accuracy. Moreover, due to the superior spatial resolution of STEM compared nanofocus x-ray diffraction it is possible to resolve that the inner QW comprises an In content that is up to 3 % larger compared to the one of the outer QW.

6.6 Concluding remarks

Individual (In,Ga)N/GaN core-shell micro-rods are investigated in terms of structural properties, local strain field and chemical composition via nanofocus x-ray diffraction, reflectivity and HAADF STEM. Thereby, it is found that the multi-shell structure exhibits a significant increase in thickness in all sub-shells from bottom to top along the rod. Consequently, the rod diameter increases and only at a certain height m-plane facets are formed. Based on the structural parameters retrieved from both complementary methods, FEM and subsequent kinematic scattering simulations are performed. Due to the fact, that the structural parameters of the shells are very well approximated, it is possible to fit the x-ray diffraction profiles by the In content which is the sole free remaining parameter. By that it is possible to prove that the increase of shell thickness goes along with a significant increase in the In content. As long as relaxation occurs purely elastic, the presented approach for an accurate determination of the In content is expected to be highly reliable. Due to the higher resolution, HAADF STEM not only shows that the In content increases but also that the In content in the inner QW is higher compared to the outer one. Moreover, HAADF STEM measurements reveal that

the top region of the rod is subject to plastic relaxation. Here, it is found that elastic relaxation decreases and that strain is relieved by plastic relaxation expressed by an increasing density of horizontal partial dislocation lines. In the top area an even higher In content is expected, however, as only elastic relaxation is considered in the FEM simulations only a lower limit of the actual In content can be retrieved. The presented study demonstrates that by combining nanofocus x-ray diffraction complemented with FEM-based kinematic scattering simulations and HAADF STEM on ideally the same object, a deep insight about structure and chemical composition of low-dimensional semiconductors can be obtained.

7 Conclusion

In this thesis, nanofocus x-ray diffraction and the numerical finite element method (FEM) are applied to investigate the deformation field in (In,Ga)N/GaN nanowires (NWs) and micro-rods. Thereby, the work contributes to the fundamental understanding of the local strain distribution and the deduced optical properties of axial (In,Ga)N/GaN NWs and provides instructive insights about structure and chemical composition of (In,Ga)N/GaN core-shell micro-rod light emitting diodes (LEDs). The gained knowledge can be used to engineer the strain field and, thus, to control the optoelectronic properties of potential devices. Moreover, from the detailed analysis of core-shell micro-rods conclusions can be drawn how to improve their growth with respect to homogeneity which likewise leads to an enhanced light exploitation. Next to addressing questions related to materials science, this thesis also intends to investigate the feasibility of nanofocus x-ray diffraction for analyzing low-dimensional semiconductors. In this respect, the experiments performed on individual micro-rods show that especially for µm-sized objects the provided resolution in the order of $100\times100\,\mathrm{nm}^2$ is ideal to obtain decisive insights about the local strain distribution.

In detail, the first part of this thesis deals with a counterintuitive strain relaxation scenario inherent to axial NW heterostructures. By applying the FEM, the dependence of the vertical normal component of the elastic strain tensor, ε_{zz}, on the ratio of NW radius and (In,Ga)N segment length is analyzed using the example of an axial (In,Ga)N/GaN NW. While for small segment lengths a strain distribution similar to that of an equivalent planar sequence is observed, a clearly negative ε_{zz} value is found if the ratio of radius and segment length approaches unity. Significant shear strain components accompanied by a strong convex deformation of the outer segment surface are discussed as the origin of this phenomenon and manifest the crucial difference to equivalent planar systems where shear strains are non-existing and, thus, ε_{zz} is always positive or zero. Furthermore, in literature an ongoing assumption was that due to the high surface-to-volume ratio a complete relaxation of the embedded (In,Ga)N segment should be observed. The presented study shows that for large segment lengths indeed full relaxation occurs in the center of the segment, however, at the free surface and especially at the interfaces to the GaN matrix, a considerable strain is observed. Owing to the fact, that in linear elasticity the strain components are dimensionless, the presented phenomenon can be scaled arbitrarily to other dimensions and In contents as long as strain relaxation proceeds elastically. Moreover, the effect is of relevance for a variety of other axial NW heterostructures, too.

The finding, that the ε_{zz} component can be tuned from tensile to compressive has important consequences as it offers a new degree of freedom for engineering the strain distribution and might be used to minimize the inherently strong built-

in potential. Therefore, in the subsequent study the FEM is applied to compute the electric potential in [0001]-oriented axial (In,Ga)N/GaN NWs arising from the piezoelectric and the spontaneous polarization. In particular, the electric potential is discussed in dependence on the ratio of NW radius and segment length and, actually, it is found that the complex strain distribution related to shear strains yields a decisive deviation from the expected linear increase of the electric potential with the segment length. This deviation leads to the consequence that the range of accessible wavelengths for a given NW geometry is significantly reduced. Moreover, it yields that the distribution of electron and hole ground state charge densities proceeds in a non-trivial manner and for each configuration, the appropriate parameters have to be found independently to guarantee an optimum overlap of electron and hole wavefunctions.

Additionally to the purely theoretical investigation of axial (In,Ga)N/GaN NWs, experimental investigations of core-shell (In,Ga)N/GaN micro-rod LEDs are presented. Via prior cathodoluminescence (CL) measurements it has been found that the emission wavelength along the height of core-shell (In,Ga)N/GaN micro-rod LEDs is red-shifted. However, the origin of this effect remained unclear. To shed light on this open question, nanofocus x-ray diffraction experiments are performed on single core-shell (In,Ga)N/GaN rods. Using a focused ion beam, a row of neighboring rods is isolated in a lamella which enables the investigation of individual objects. By scanning the focused x-ray beam over selected rods, it is possible to resolve the local strain field in individual side-facets. As a result of the high spatial resolution, a significant strain gradient along the rod height is detected which is translated into an In content by employing the FEM and subsequent kinematic scattering simulations. Thereby, it is found that the In content increases by about 10 % from the rod middle to the top which matches very well the CL measurements performed on rods from the same sample. The presented experiments prove that due to the sub-µm resolution, nanofocus x-ray diffraction provides a powerful technique to locally analyze the strain distribution in µm-sized individual objects. In fact, this spatial resolution is ideal to measure the local strain state even within individual facets of a single rod in its as-grown environment, while methods with higher, e. g., atomistic resolution or with lower penetration depth would fail.

The In content is one of the crucial parameters for controlling the optical performance of micro-rod LEDs and, obviously, an accurate determination of the latter is of great interest. To improve the translation of the strain state into an In content the structural parameters within the illuminated volume has to be taken into account because structural inhomogeneities additionally modify the strain field. The complete characterization of structure and chemical composition is demonstrated using the example of a single micro-rod comprising a two-fold (In,Ga)N quantum well embedded into GaN core-shell geometry. At selected heights the local strain distribution in an individual side-facet is analyzed. Moreover, at the same positions nanofocus x-ray reflectivity is employed to obtain structural information. Additionally performed scanning transmission electron microscopy (STEM) measurements conducted on rods from the same

sample complement the synchrotron experiments and provide further insights about structure and plastic relaxation. The accumulation of the gained results show that all sub-shells face a drastic increase in thickness from bottom to top. Taking into account the structural inhomogeneity, the retrieved shell thicknesses serve as input for FEM simulations of the deformation field in the illuminated regions. Due to the fact that the local structure is well known, the In content serves as the sole free remaining parameter and can be used to fit subsequent kinematic scattering simulations to the experimentally measured nanofocus x-ray diffraction profiles. Thereby, the In content can be determined with an even higher accuracy and appears to increase significantly. As a consequence of plastic relaxation in the top region of the investigated rod, the proposed method loses accuracy and the retrieved In content in the top region can be interpreted as a lower boundary.

Outlook

There exist a variety of ideas for future research projects building up directly on the experiments and techniques presented in this thesis. Accordingly, they are related to the investigation of low-dimensional objects both experimentally by employing nanofocus x-ray diffraction and theoretically using the FEM.

To begin with, it would be highly interesting to provide an experimental proof of the counterintuitive strain relaxation behavior in axial NWs via nanofocus x-ray diffraction as presented in chapter 3.

Furthermore, CL investigations of recently grown core-shell (In,Ga)N/GaN micro-rod LEDs showed indications for the formation of In-rich columns at the edges of the hexagonal objects. First estimations predict a difference in the In content of about 20 % from corner to side-facet. Moreover, the formation of an In-rich quantum dot in the rod apex is predicted with an even higher In content. Nanofocus x-ray diffraction seems to be highly promising to investigate these features in detail and to quantify the differences in the In content.

Next to micro-rods, also (In,Ga)N/GaN fins are fabricated and optimized with respect to light exploitation [192] and first experiments using nanofocus x-ray diffraction have recently been conducted. The size of the fins exceeds the height of the investigated micro-rods by more than three times. This makes the high spatial resolution in the sub-µm regime available at specialized synchrotron beamlines even more attractive as a detailed strain analysis using other methods such as STEM would be very time consuming.

A big difference compared to conventional x-ray diffraction with comparatively large beam sizes is that when using a collimated beam individual objects can be identified and investigated by complementary methods. In this respect, it is planned to correlate nanofocus x-ray diffraction results of structure and composition of individual objects to STEM measurements performed on the very same object. Moreover, prior to these experiments, the optical properties of the object shall be investigated via spatially-resolved CL measurements allowing to correlate the emission wavelength to the inherent strain state and structural in-

homogeneities. Moreover, in collaboration with other groups experiments are planned in which nanofocus x-ray tomography, 3D x-ray fluorescence and x-ray diffraction are performed at the same time on the same object. Hereby, a setup where three detectors are operated simultaneously is employed. Also collaborations including coherent x-ray diffraction imaging on (In,Ga)As/GaAs core-shell NWs have recently been started.

Finally, the presented $k \cdot p$ calculations of the optical properties based on the strain distribution and the electric potential computed via FEM give rise to a plethora of potential studies. For example, an advantage of the FEM is that models of arbitrary shapes can be simulated. This is of great interest as in general the hexagonal NW shape is slightly deformed to various shapes and the impact on the optical properties of this deformation is planned to be analyzed in detail. Moreover, sometimes NWs do not stand up straight but are bent and in the most drastic case the NW growth results in arch-like NW shapes. How this deformation influences the optical properties would also be an interesting follow up study.

Bibliography

[1] O. Hayden, R. Agarwal, and W. Lu. Semiconductor nanowire devices. *Nano Today*, 3:12–22, 2008.

[2] J. Johansson and K. A. Dick. Recent advances in semiconductor nanowire heterostructures. *CrystEngComm*, 13:7175, 2011.

[3] H. E. Jackson, L. M. Smith, and C. Jagadish. Recent Advances in Semiconductor Nanowire Heterostructures. *ECS Trans.*, 64:1–5, 2014.

[4] J. Claudon, J. Bleuse, N. S. Malik, M. Bazin, P. Jaffrennou, N. Gregersen, C. Sauvan, P. Lalanne, and J.-M. Gerard. A highly efficient single-photon source based on a quantum dot in a photonic nanowire. *Nat. Photonics*, 4:174–177, 2010.

[5] M. E. Reimer, G. Bulgarini, N. Akopian, M. Hocevar, M. B. Bavinck, M. A. Verheijen, E. P. A. M. Bakkers, L. P. Kouwenhoven, and V. Zwiller. Bright single-photon sources in bottom-up tailored nanowires. *Nat. Commun.*, 3:737, 2012.

[6] M. J. Holmes, K. Choi, S. Kako, M. Arita, and Y. Arakawa. Room-Temperature Triggered Single Photon Emission from a III-Nitride Site-Controlled Nanowire Quantum Dot. *Nano Lett.*, 14:982–986, 2014.

[7] F. Qian, S. Gradečak, Y. Li, C.-Y. Wen, and C. M. Lieber. Core/Multishell Nanowire Heterostructures as Multicolor, High-Efficiency Light-Emitting Diodes. *Nano Lett.*, 5:2287–2291, 2005.

[8] K. Kishino, A. Kikuchi, H. Sekiguchi, and S. Ishizawa. InGaN/GaN nanocolumn LEDs emitting from blue to red. *Proc. SPIE*, 6473:64730T–64730T–12, 2007.

[9] H.-W. Lin, Y.-J. Lu, H.-Y. Chen, H.-M. Lee, and S. Gwo. InGaN/GaN nanorod array white light-emitting diode. *Appl. Phys. Lett.*, 97:073101, 2010.

[10] A. Waag, X. Wang, S. Fündling, J. Ledig, M. Erenburg, R. Neumann, M. Al Suleiman, S. Merzsch, J. Wei, S. Li, H.-H. Wehmann, W. Bergbauer, M. Straßburg, A. Trampert, U. Jahn, and H. Riechert. The nanorod approach: GaN NanoLEDs for solid state lighting. *Phys. Status Solidi*, 8:2296–2301, 2011.

[11] A.-L. Bavencove, G. Tourbot, J. Garcia, Y. Désières, P. Gilet, F. Levy, B. André, B. Gayral, B. Daudin, and L. S. Dang. Submicrometre resolved optical characterization of green nanowire-based light emitting diodes. *Nanotechnology*, 22:345705, 2011.

[12] S. Li and A. Waag. GaN based nanorods for solid state lighting. *J. Appl. Phys.*, 111:071101, 2012.

[13] S. Zhao, H. P. T. Nguyen, M. G. Kibria, and Z. Mi. III-Nitride nanowire optoelectronics. *Prog. Quantum Electron.*, 44:14–68, 2015.

[14] X. Duan, Y. Huang, R. Agarwal, and C. M. Lieber. Single-nanowire electrically driven lasers. *Nature*, 421:241–245, 2003.

[15] F. Qian, Y. Li, S. Gradečak, H. Park, Y. Dong, Y. Ding, Z. L. Wang, and C. M. Lieber. Multi-quantum-well nanowire heterostructures for wavelength-controlled lasers. *Nat. Mater.*, 7:701–706, 2008.

[16] D. Saxena, S. Mokkapati, P. Parkinson, N. Jiang, Q. Gao, H. H. Tan, and C. Jagadish. Optically pumped room-temperature GaAs nanowire lasers. *Nat. Photonics*, 7:963–968, 2013.

[17] J. Kamimura, P. Bogdanoff, J. Lähnemann, C. Hauswald, L. Geelhaar, S. Fiechter, and H. Riechert. Photoelectrochemical Properties of (In,Ga)N Nanowires for Water Splitting Investigated by in Situ Electrochemical Mass Spectroscopy. *J. Am. Chem. Soc.*, 135:10242–10245, 2013.

[18] J. Kamimura, P. Bogdanoff, M. Ramsteiner, L. Geelhaar, and H. Riechert. Photoelectrochemical properties of InN nanowire photoelectrodes for solar water splitting. *Semicond. Sci. Technol.*, 31:74001, 2016.

[19] J. Luo, L. Steier, M.-K. Son, M. Schreier, M. T. Mayer, and M. Grätzel. Cu2O Nanowire Photocathodes for Efficient and Durable Solar Water Splitting. *Nano Lett.*, 16:1848–1857, 2016.

[20] K. Tomioka, T. Tanaka, S. Hara, K. Hiruma, and T. Fukui. III-V Nanowires on Si Substrate: Selective-Area Growth and Device Applications. *IEEE J. Sel. Topics Quantum Electron.*, 17:1112–1129, 2011.

[21] W. Guo, A. Banerjee, P. Bhattacharya, and B. S. Ooi. InGaN/GaN disk-in-nanowire white light emitting diodes on (001) silicon. *Appl. Phys. Lett.*, 98:193102, 2011.

[22] M. Hocevar, G. Immink, M. Verheijen, N. Akopian, V. Zwiller, L. Kouwenhoven, and E. Bakkers. Growth and optical properties of axial hybrid III–V/silicon nanowires. *Nat. Commun.*, 3:1266, 2012.

[23] D. Zhu, D. J. Wallis, and C. J. Humphreys. Prospects of III-nitride optoelectronics grown on Si. *Reports Prog. Phys.*, 76:106501, 2013.

[24] K. Kishino and S. Ishizawa. Selective-area growth of GaN nanocolumns on Si(111) substrates for application to nanocolumn emitters with systematic analysis of dislocation filtering effect of nanocolumns. *Nanotechnology*, 26:225602, 2015.

[25] J. Xiang, W. Lu, Y. Hu, Y. Wu, H. Yan, and C. M. Lieber. Ge/Si nanowire heterostructures as high-performance field-effect transistors. *Nature*, 441:489–493, 2006.

[26] J. Appenzeller, J. Knoch, M. T. Bjork, H. Riel, H. Schmid, and W. Riess. Toward nanowire electronics. *IEEE Trans. Electron Devices*, 55:2827–2845, 2008.

[27] P. Fei, P.-H. Yeh, J. Zhou, S. Xu, Y. Gao, J. Song, Y. Gu, Y. Huang, and Z. L. Wang. Piezoelectric Potential Gated Field-Effect Transistor Based on a Free-Standing ZnO Wire. *Nano Lett.*, 9:3435–3439, 2009.

[28] K. Tomioka, M. Yoshimura, and T. Fukui. A III-V nanowire channel on silicon for high-performance vertical transistors. *Nature*, 488:189–192, 2012.

[29] Y. Yu, W. Li, P. Wu, C. Jiang, and X. Xiao. Gate dielectric ion implantation to modulate the threshold voltage of In_2O_3 nanowire field effect transistors. *Appl. Phys. Lett.*, 109:193505, 2016.

[30] B. Tian, X. Zheng, T. J. Kempa, Y. Fang, N. Yu, G. Yu, J. Huang, and C. M. Lieber. Coaxial silicon nanowires as solar cells and nanoelectronic power sources. *Nature*, 449:885–889, 2007.

[31] J. Wallentin, N. Anttu, D. Asoli, M. Huffman, I. Åberg, M. H. Magnusson, G. Siefer, P. Fuss-Kailuweit, F. Dimroth, B. Witzigmann, H. Q. Xu, L. Samuelson, K. Deppert, and M. T. Borgström. InP nanowire array solar cells achieving 13.8% efficiency by exceeding the ray optics limit. *Science*, 339:1057–1060, 2013.

[32] B. R. Yakami, U. Poudyal, S. R. Nandyala, G. Rimal, J. K. Cooper, X. Zhang, J. Wang, W. Wang, and J. M. Pikal. Steady state and time resolved optical characterization studies of Zn_2SnO_4 nanowires for solar cell applications. *J. Appl. Phys.*, 120:163101, 2016.

[33] J. Als-Nielsen and D. McMorrow. *Elements of modern x-ray physics*. John Wiley and Sons, Ltd, 2001.

[34] C. Mocuta, J. Stangl, K. Mundboth, T. H. Metzger, G. Bauer, I. A. Vartanyants, M. Schmidbauer, and T. Boeck. Beyond the ensemble average: X-ray microdiffraction analysis of single SiGe islands. *Phys. Rev. B*, 77:245425, 2008.

[35] M. Hanke, M. Dubslaff, M. Schmidbauer, T. Boeck, S. Schöder, M. Burghammer, C. Riekel, J. Patommel, and C. G. Schroer. Scanning x-ray diffraction with 200 nm spatial resolution. *Appl. Phys. Lett.*, 92:193109, 2008.

[36] A. Biermanns, D. Carbone, S. Breuer, V. L. R. Jacques, T. U. Schülli, L. Geelhaar, and U. Pietsch. Distribution of zinc-blende twins and wurtzite segments in GaAs nanowires probed by X-ray nanodiffraction. *Phys. status solidi – Rapid Res. Lett.*, 7:860–863, 2013.

[37] J. Gulden, S. O. Mariager, A. P. Mancuso, O. M. Yefanov, J. Baltser, P. Krogstrup, J. Patommel, M. Burghammer, R. Feidenhans'l, and I. A. Vartanyants. Coherent X-ray nanodiffraction on single GaAs nanowires. *Phys. Status Solidi*, 208:2495–2498, 2011.

[38] T. Stankevič, D. Dzhigaev, Z. Bi, M. Rose, A. Shabalin, J. Reinhardt, A. Mikkelsen, L. Samuelson, G. Falkenberg, I. A. Vartanyants, and R. Feidenhans'l. Strain mapping in an InGaN/GaN nanowire using a nanofocused x-ray beam. *Appl. Phys. Lett.*, 107:103101, 2015.

[39] T. Stankevič, S. Mickevičius, M. Schou Nielsen, O. Kryliouk, R. Ciechonski, G. Vescovi, Z. Bi, A. Mikkelsen, L. Samuelson, C. Gundlach, and R. Feidenhans'l. Measurement of strain in InGaN/GaN nanowires and nanopyramids. *J. Appl. Crystallogr.*, 48:344–349, 2015.

[40] M. Keplinger, R. Grifone, J. Greil, D. Kriegner, J. Persson, A. Lugstein, T. Schülli, and J. Stangl. Strain distribution in single, suspended germanium nanowires studied using nanofocused x-rays. *Nanotechnology*, 27:055705, 2016.

[41] J. Segura-Ruiz, G. Martínez-Criado, J. A. Sans, R. Tucoulou, P. Cloetens, I. Snigireva, C. Denker, J. Malindretos, A. Rizzi, M. Gomez-Gomez, N. Garro, and A. Cantarero. Direct observation of elemental segregation in InGaN nanowires by X-ray nanoprobe. *Phys. status solidi–Rapid Res. Lett.*, 5:95–97, 2011.

[42] J. Segura-Ruiz, G. Martínez-Criado, C. Denker, J. Malindretos, and A Rizzi. Phase Separation in Single $In_xGa_{1-x}N$ Nanowires Revealed through a Hard X–ray Synchrotron Nanoprobe. *Nano Lett.*, 14:1300–1305, 2014.

[43] G. Bussone, R. Schott, A. Biermanns, A. Davydok, D. Reuter, G. Carbone, T. U. Schülli, A. D. Wieck, and U. Pietsch. Grazing-incidence X-ray diffraction of single GaAs nanowires at locations defined by focused ion beams. *J. Appl. Crystallogr.*, 46:887–892, 2013.

[44] G. Bussone, H. Schäfer-Eberwein, E. Dimakis, A. Biermanns, D. Carbone, A. Tahraoui, L. Geelhaar, P. Haring Bolívar, T. U. Schülli, and

U. Pietsch. Correlation of Electrical and Structural Properties of Single As-Grown GaAs Nanowires on Si (111) Substrates. *Nano Lett.*, 15:981–989, 2015.

[45] T. W. Cornelius, A. Davydok, V. L. R. Jacques, R. Grifone, T. U. Schülli, M. I. Richard, G. Beutier, M. Verdier, T. H. Metzger, U. Pietsch, and O. Thomas. In situ three-dimensional reciprocal-space mapping during mechanical deformation. *J. Synchrotron Radiat.*, 19:688–94, 2012.

[46] M. A. Pfeifer, G. J. Williams, I. A. Vartanyants, R. Harder, and I. Robinson. Three-dimensional mapping of a deformation field inside a nanocrystal. *Nature*, 442:63–66, 2006.

[47] I. Robinson and R. Harder. Coherent X-ray diffraction imaging of strain at the nanoscale. *Nat Mater*, 8:291–298, 2009.

[48] A. Diaz, C. Mocuta, J. Stangl, B. Mandl, C. David, J. Vila-Comamala, V. Chamard, T. H. Metzger, and G. Bauer. Coherent diffraction imaging of a single epitaxial InAs nanowire using a focused x-ray beam. *Phys. Rev. B*, 79:125324, 2009.

[49] Y. Takahashi, N. Zettsu, Y. Nishino, R. Tsutsumi, E. Matsubara, T. Ishikawa, and K. Yamauchi. Three-Dimensional Electron Density Mapping of Shape-Controlled Nanoparticle by Focused Hard X-ray Diffraction Microscopy. *Nano Lett.*, 10:1922–1926, 2010.

[50] V. Favre-Nicolin, F. Mastropietro, J. Eymery, D. Camacho, Y. M. Niquet, B. M. Borg, M. E. Messing, L.-E. Wernersson, R. E. Algra, E. P. A. M. Bakkers, T. H. Metzger, R. Harder, and I. Robinson. Analysis of strain and stacking faults in single nanowires using Bragg coherent diffraction imaging. *New J. Phys.*, 12:035013, 2010.

[51] G. Xiong, O. Moutanabbir, M. Reiche, R. Harder, and I. Robinson. Coherent X-Ray Diffraction Imaging and Characterization of Strain in Silicon-on-Insulator Nanostructures. *Adv. Mater.*, 26:7747–7763, 2014.

[52] T. Stankevič, E. Hilner, F. Seiboth, R. Ciechonski, G. Vescovi, O. Kryliouk, U. Johansson, L. Samuelson, G. Wellenreuther, G. Falkenberg, R. Feidenhans'l, and A. Mikkelsen. Fast Strain Mapping of Nanowire Light-Emitting Diodes Using Nanofocused X-ray Beams. *ACS Nano*, 9:6978–6984, 2015.

[53] A. Davtyan, A. Biermanns, O. Loffeld, and U. Pietsch. Determination of the stacking fault density in highly defective single GaAs nanowires by means of coherent diffraction imaging. *New J. Phys.*, 18:63021, 2016.

[54] D. Dzhigaev, A. Shabalin, T. Stankevič, U. Lorenz, R. P. Kurta, F. Seiboth, J. Wallentin, A. Singer, S. Lazarev, O. M. Yefanov, M. Borgström, M. N. Strikhanov, L. Samuelson, G. Falkenberg, C. G. Schroer, A. Mikkelsen,

R. Feidenhans'l, and I. A. Vartanyants. Bragg coherent x-ray diffractive imaging of a single indium phosphide nanowire. *J. Opt.*, 18:064007, 2016.

[55] M. Hanke, C. Eisenschmidt, P. Werner, N. D. Zakharov, F. Syrowatka, F. Heyroth, P. Schäfer, and O. Konovalov. Elastic strain relaxation in axial Si/Ge whisker heterostructures. *Phys. Rev. B*, 75:161303, 2007.

[56] M. Keplinger, D. Kriegner, J. Stangl, T. Mårtensson, B. Mandl, E. Wintersberger, and G. Bauer. Core–shell nanowires: From the ensemble to single-wire characterization. *Nuc. Instruments and Methods Phys. Res. Sect. B Beam Interact. with Mater. Atoms*, 268:316–319, 2010.

[57] M. Keplinger, B. Mandl, D. Kriegner, V. Holý, L. Samuelsson, G. Bauer, K. Deppert, and J. Stangl. X-ray diffraction strain analysis of a single axial $InAs_{1-x}P_x$ nanowire segment. *J. Synchrotron Radiat.*, 22:59–66, 2015.

[58] M. Dubslaff, M. Hanke, M. Burghammer, S. Schröder, R. Hoppe, C. G. Schroer, Yu. I. Mazur, Zh. M. Wang, J. H. Lee, and G. J. Salamo. In(Ga)As/GaAs(001) quantum dot molecules probed by nanofocus high resolution x-ray diffraction with 100 nm resolution. *Appl. Phys. Lett.*, 98:213105, 2011.

[59] M. Dubslaff, M. Hanke, J. Patommel, R. Hoppe, C. G. Schroer, S. Schöder, and M. Burghammer. Scanning X-ray nanodiffraction: from the experimental approach towards spatially resolved scattering simulations. *Nanoscale Res. Lett.*, 7:1–8, 2012.

[60] T. Etzelstorfer, M. J. Süess, G. L. Schiefler, V. L. R. Jacques, D. Carbone, D. Chrastina, G. Isella, R. Spolenak, J. Stangl, H. Sigg, and A. Diaz. Scanning X-ray strain microscopy of inhomogeneously strained Ge microbridges. *J. Synchrotron Radiat.*, 21:111–118, 2014.

[61] S. Nakamura, S. Pearton, and G. Fasol. *The Blue Laser Diode*. Springer-Verlag Berlin Heidelberg, second edition, 2000.

[62] F. Glas. Critical dimensions for the plastic relaxation of strained axial heterostructures in free-standing nanowires. *Phys. Rev. B*, 74:121302, 2006.

[63] T. Kuykendall, P. Ulrich, S. Aloni, and P. Yang. Complete composition tunability of InGaN nanowires using a combinatorial approach. *Nat. Mater.*, 6:951–956, 2007.

[64] T. Kuykendall, A. M. Schwartzberg, and S. Aloni. Gallium Nitride Nanowires and Heterostructures: Toward Color-Tunable and White-Light Sources. *Adv. Mater.*, 27:5805–5812, 2015.

[65] C. Kittel. *Introduction to solid state physics*. John Wiley and Sons, Ltd, 1967.

[66] J. P. Hirth and J Lothe. *Theory of dislocations*. John Wiley and Sons, Inc., 1982.

[67] J. F. Nye. *Physical properties of crystals*. Oxford University Press 1957, 1985.

[68] A. Sommerfeld. *Mechanik der deformierbaren Medien*. Verlag Harri Deutsch, 1992.

[69] N. W. Ahscroft and D. Mermin. *Festkörperphysik*. Oldenburg Wissenschaftsverlag GmbH, 2007.

[70] R. Gross and A. Marx. *Festkörperphysik*. Oldenburg Wissenschaftsverlag GmbH, 2012.

[71] B. M. Neubert. *GaInN/GaN LEDs auf semipolaren Seitenfacetten mittels selektiver Epitaxie hergestellter GaN-Streifen*. Cuviller Verlag, 2008.

[72] K.-J. Bathe. *Finite element procedures in engineering analysis*. Prentice-Hall, Inc., Englewood Cliffs, New Jersey 07632, 1982.

[73] MSC Software Corporation. *MSC.Marc and Mentat Users's Guide and Volume A: Theory and User Information 2008rl*.

[74] B. E. Warren. *X-ray diffraction*. Dover Publications, Inc., New York, 1990.

[75] U. Pietsch, V. Holý, and T. Baumbach. *High-resolution x-ray scattering*. Springer-Verlag New York, LLC, 2004.

[76] J. Stangl, C. Mocuta, V. Chamard, and D. Carbone. *Nanobeam X-Ray Scattering*. Wiley-VCH Verlag GmbH and Co. KGaA, 2013.

[77] J. J. Wierer, D. A. Steigerwald, M. R. Krames, J. J. O'Shea, M. J. Ludowise, G. Christenson, Y.-C. Shen, C. Lowery, P. S. Martin, S. Subramanya, W. Götz, N. F. Gardner, R. S. Kern, and S. A. Stockman. High-power AlGaInN flip-chip light-emitting diodes. *Appl. Phys. Lett.*, 78:3379–3381, 2001.

[78] V. Zabelin, D. A. Zakheim, and S. A. Gurevich. Efficiency improvement of AlGaInN LEDs advanced by ray-tracing analysis. *IEEE J. Quantum Electron.*, 40:1675–1686, 2004.

[79] S.-R. Jeon, M. Gherasimova, Z. Ren, J. Su, G. Cui, J. Han, H. Peng, Y.-K. Song, A. V. Nurmikko, L. Zhou, W. Goetz, and M. Krames. High Performance AlGaInN Ultraviolet Light-Emitting Diode at the 340 nm Wavelength. *Jpn. J. Appl. Phys.*, 43:L1409–L1412, 2004.

[80] O. Ambacher. Growth and applications of Group III-nitrides. *J. Phys. D. Appl. Phys.*, 31:2653, 1998.

[81] J. H. Choi, A. Zoulkarneev, S. I. Kim, C. W. Baik, M. H. Yang, S. S. Park, H. Suh, U. J. Kim, H. Bin Son, J. S. Lee, M. Kim, J. M. Kim, and K. Kim. Nearly single-crystalline GaN light-emitting diodes on amorphous glass substrates. *Nat. Photonics*, 5:763–769, 2011.

[82] F. Schuster, M. Hetzl, S. Weiszer, J. A. Garrido, M. de la Mata, C. Magen, J. Arbiol, and M. Stutzmann. Position-Controlled Growth of GaN Nanowires and Nanotubes on Diamond by Molecular Beam Epitaxy. *Nano Lett.*, 15:1773–1779, 2015.

[83] B. J. May, A. T. M. Golam Sarwar, and R. C. Myers. Nanowire LEDs grown directly on flexible metal foil. *Appl. Phys. Lett.*, 108:141103, 2016.

[84] M. Feneberg, M. Röppischer, C. Cobet, N. Esser, J. Schörmann, T. Schupp, D. J. As, F. Hörich, J. Bläsing, A. Krost, and R. Goldhahn. Optical properties of cubic GaN from 1 to 20 eV. *Phys. Rev. B*, 85:155207, 2012.

[85] Y. L. Casallas-Moreno, M. Pérez-Caro, S. Gallardo-Hernández, M. Ramírez-López, I. Martínez-Velis, A. Escobosa-Echavarría, and M. López-López. Study of structural properties of cubic InN films on GaAs(001) substrates by molecular beam epitaxy and migration enhanced epitaxy. *J. Appl. Phys.*, 113:214308, 2013.

[86] S. Kako, M. Holmes, S. Sergent, M. Bürger, D. J. As, and Y. Arakawa. Single-photon emission from cubic GaN quantum dots. *Appl. Phys. Lett.*, 104:011101, 2014.

[87] P. Kidd. *XRD of Gallium Nitride and Related Compounds: Strain, Composition and Layer Thickness*. Panalytical, Almelo, 2009.

[88] J. Wu. When group-III nitrides go infrared: New properties and perspectives. *J. Appl. Phys.*, 106:011101, 2009.

[89] B. Damilano, N. Grandjean, J. Massies, L. Siozade, and J. Leymarie. InGaN/GaN quantum wells grown by molecular-beam epitaxy emitting from blue to red at 300 K. *Appl. Phys. Lett.*, 77:1268, 2000.

[90] J. H. Son and J.-L. Lee. Strain engineering for the solution of efficiency droop in InGaN/GaN light-emitting diodes. *Opt. Express*, 18:5466–5471, 2010.

[91] X. Yang, M. Arita, S. Kako, and Y. Arakawa. Formation of m-plane InGaN/GaN quantum dots using strain engineering of AlGaN/AlN interlayers. *Appl. Phys. Lett.*, 99:61914, 2011.

[92] M. Wölz, M. Ramsteiner, V. M. Kaganer, O. Brandt, L. Geelhaar, and H. Riechert. Strain Engineering of Nanowire Multi-Quantum Well Demonstrated by Raman Spectroscopy. *Nano Lett.*, 13:4053–4059, 2013.

[93] Y. Zhao, S. H. Oh, F. Wu, Y. Kawaguchi, S. Tanaka, K. Fujito, J. S. Speck, S. P. DenBaars, and S. Nakamura. Green Semipolar $(20\bar{2}\bar{1})$ InGaN Light-Emitting Diodes with Small Wavelength Shift and Narrow Spectral Linewidth. *Appl. Phys. Express*, 6:62102, 2013.

[94] Y.-L. Tsai, C.-Y. Liu, C. Krishnan, D.-W. Lin, Y.-C. Chu, T.-P. Chen, T.-L. Shen, T.-S. Kao, M. D. B. Charlton, P. Yu, C.-C. Lin, H.-C. Kuo, and J.-H. He. Bridging the „green gap“ of LEDs: giant light output enhancement and directional control of LEDs via embedded nano-void photonic crystals. *Nanoscale*, 8:1192–1199, 2016.

[95] C. Zhao, T. K. Ng, R. T. ElAfandy, A. Prabaswara, G. B. Consiglio, I. A. Ajia, I. S. Roqan, B. Janjua, C. Shen, J. Eid, A. Y. Alyamani, M. M. El-Desouki, and B. S. Ooi. Droop-Free, Reliable, and High-Power InGaN/GaN Nanowire Light-Emitting Diodes for Monolithic Metal-Optoelectronics. *Nano Lett.*, 16:4616–4623, 2016.

[96] O. Ambacher, J. Majewski, C. Miskys, A. Link, M. Hermann, M. Eickhoff, M. Stutzmann, F. Bernardini, V. Fiorentini, V. Tilak, B. Schaff, and L. F. Eastman. Pyroelectric properties of Al(In)GaN/GaN hetero- and quantum well structures. *J. Phys. Condens. Matter*, 14:3399, 2002.

[97] P. Waltereit, O. Brandt, A. Trampert, H. T. Grahn, J. Menniger, M. Ramsteiner, M. Reiche, and K. H. Ploog. Nitride semiconductors free of electrostatic fields for efficient white light-emitting diodes. *Nature*, 406:865–868, 2000.

[98] M. Leroux, N. Grandjean, M. Laügt, J. Massies, B. Gil, P. Lefebvre, and P. Bigenwald. Quantum confined Stark effect due to built-in internal polarization fields in (Al,Ga)N/GaN quantum wells. *Phys. Rev. B*, 58:R13371–R13374, 1998.

[99] H. Masui, J. Sonoda, N. Pfaff, I. Koslow, S. Nakamura, and S. P. DenBaars. Quantum-confined Stark effect on photoluminescence and electroluminescence characteristics of InGaN-based light-emitting diodes. *J. Phys. D. Appl. Phys.*, 41:165105, 2008.

[100] S. De, A. Layek, S. Bhattacharya, D. Kumar Das, A. Kadir, A. Bhattacharya, S. Dhar, and A. Chowdhury. Quantum-confined stark effect in localized luminescent centers within InGaN/GaN quantum-well based light emitting diodes. *Appl. Phys. Lett.*, 101:121919, 2012.

[101] J. Lähnemann, P. Corfdir, F. Feix, J. Kamimura, T. Flissikowski, H. T. Grahn, L. Geelhaar, and O. Brandt. Radial Stark Effect in (In,Ga)N Nanowires. *Nano Lett.*, 16:917–925, 2016.

[102] P. Horenburg, E. R. Buß, U. Rossow, H. Bremers, F. A. Ketzer, and A. Hangleiter. Strain dependence of In incorporation in m-oriented

GaInN/GaN multi quantum well structures. *Appl. Phys. Lett.*, 108:102105, 2016.

[103] T. Schimpke, M. Mandl, I. Stoll, B. Pohl-Klein, D. Bichler, F. Zwaschka, J. Strube-Knyrim, B. Huckenbeck, B. Max, M. Müller, P. Veit, F. Bertram, J. Christen, J. Hartmann, A. Waag, H.-J. Lugauer, and M. Strassburg. Phosphor-converted white light from blue-emitting InGaN microrod LEDs. *Phys. Status Solidi*, 6:1577–1584, 2016.

[104] T. Wang. Topical Review: Development of overgrown semi-polar GaN for high efficiency green/yellow emission. *Semicond. Sci. Technol.*, 31:93003, 2016.

[105] E. Ertekin, P. A. Greaney, D. C. Chrzan, and T. D. Sands. Equilibrium limits of coherency in strained nanowire heterostructures. *J. Appl. Phys.*, 97:114325, 2005.

[106] H. Ye, P. Lu, Z. Yu, Y. Song, D. Wang, and S. Wang. Critical Thickness and Radius for Axial Heterostructure Nanowires Using Finite-Element Method. *Nano Lett.*, 9:1921–1925, 2009.

[107] K. L. Kavanagh. Misfit dislocations in nanowire heterostructures. *Semicond. Sci. Technol.*, 25:024006, 2010.

[108] S. D. Hersee, A. K. Rishinaramangalam, M. N. Fairchild, L. Zhang, and P. Varangis. Threading defect elimination in GaN nanowires. *J. Mater. Res.*, 26:2293–2298, 2011.

[109] M. V. Nazarenko, N. V. Sibirev, K. W. Ng, F. Ren, W. S. Ko, V. G. Dubrovskii, and C. Chang-Hasnain. Elastic energy relaxation and critical thickness for plastic deformation in the core-shell InGaAs/GaAs nanopillars. *J. Appl. Phys.*, 113:104311, 2013.

[110] O. Salehzadeh, K. L. Kavanagh, and S. P. Watkins. Geometric limits of coherent III-V core/shell nanowires. *J. Appl. Phys.*, 114, 2013.

[111] X. Yan, S. Fan, X. Zhang, and X. Ren. Analysis of Critical Dimensions for Nanowire Core-Multishell Heterostructures. *Nanoscale Res. Lett.*, 10:389, 2015.

[112] J.W. Matthews and A.E. Blakeslee. Defects in epitaxial multilayers: I. Misfit dislocations . *J. Cryst. Growth*, 27:118 – 125, 1974.

[113] J. W. Matthews. Defects associated with the accommodation of misfit between crystals. *J. Vac. Sci. Technol.*, 12:126–133, 1975.

[114] C. A. Parker, J. C. Roberts, S. M. Bedair, M. J. Reed, S. X. Liu, and N. A. El-Masry. Determination of the critical layer thickness in the InGaN/GaN heterostructures. *Appl. Phys. Lett.*, 75:2776, 1999.

[115] S. Pereira, M. R. Correia, E. Pereira, C. Trager Cowan, F. Sweeney, K. P. O'Donnell, E. Alves, N. Franco, and A. D. Sequeira. Structural and optical properties of InGaN/GaN layers close to the critical layer thickness. *Appl. Phys. Lett.*, 81:1207, 2002.

[116] D. Dobrovolskas, A. Vaitkevičius, J. Mickevičius, Ö. Tuna, C. Giesen, M. Heuken, and G. Tamulaitis. Correlation between structure and photoluminescence properties in InGaN epilayers with thicknesses below and above critical thickness. *J. Appl. Phys.*, 114:163516, 2013.

[117] E. Wintersberger, N. Hrauda, D. Kriegner, M. Keplinger, G. Springholz, J. Stangl, G. Bauer, J. Oswald, T. Belytschko, C. Deiter, F. Bertram, and O. H. Seeck. Analysis of periodic dislocation networks using x-ray diffraction and extended finite element modeling. *Appl. Phys. Lett.*, 96:131905, 2010.

[118] J. Oswald, E. Wintersberger, G. Bauer, and T. Belytschko. A higher-order extended finite element method for dislocation energetics in strained layers and epitaxial islands. *Int. J. Numer. Methods Eng.*, 85:920–938, 2011.

[119] Y. Gao and Z. L. Wang. Electrostatic Potential in a Bent Piezoelectric Nanowire. The Fundamental Theory of Nanogenerator and Nanopiezotronics. *Nano Lett.*, 7:2499–2505, 2007.

[120] G. Mantini, Y. Gao, A. D'Amico, C. Falconi, and Z. Lin Wang. Equilibrium piezoelectric potential distribution in a deformed ZnO nanowire. *Nano Res.*, 2:624–629, 2009.

[121] R. Giuseppe, G. Mantini, A. Di Carlo, A. D'Amico, C. Falconi, and Z. L. Wang. Piezoelectric potential in vertically aligned nanowires for high output nanogenerators. *Nanotechnology*, 22:465401, 2011.

[122] A. D. Bykhovski, B. L. Gelmont, and M. S. Shur. Elastic strain relaxation and piezoeffect in GaN-AlN, GaN-AlGaN and GaN-InGaN superlattices. *J. Appl. Phys.*, 81:6332–6338, 1997.

[123] E. T. Yu, X. Z. Dang, P. M. Asbeck, S. S. Lau, and G. J. Sullivan. Spontaneous and piezoelectric polarization effects in III–V nitride heterostructures. *J. Vac. Sci. Technol. B Microelectron. Nanom. Struct.*, 17:1742, 1999.

[124] M. E. Aumer, S. F. LeBoeuf, B. F. Moody, and S. M. Bedair. Strain-induced piezoelectric field effects on light emission energy and intensity from AlInGaN/InGaN quantum wells. *Appl. Phys. Lett.*, 79:3803–3805, 2001.

[125] J. Lähnemann, O. Brandt, C. Pfüller, T. Flissikowski, U. Jahn, E. Luna, M. Hanke, M. Knelangen, A. Trampert, and H. T. Grahn. Coexistence

of quantum-confined Stark effect and localized states in an (In,Ga)N/GaN nanowire heterostructure. *Phys. Rev. B*, 84:155303, 2011.

[126] M. A. Caro, S. Schulz, and E. P. O'Reilly. Theory of local electric polarization and its relation to internal strain: Impact on polarization potential and electronic properties of group-III nitrides. *Phys. Rev. B*, 88:214103, 2013.

[127] W. Z. Tawfik, G. Y. Hyeon, and J. K. Lee. Stress-induced piezoelectric field in GaN-based 450-nm light-emitting diodes. *J. Appl. Phys.*, 116:164503, 2014.

[128] X. Zhang, V. G. Dubrovskii, N. V. Sibirev, and X. Ren. Analytical Study of Elastic Relaxation and Plastic Deformation in Nanostructures on Lattice Mismatched Substrates. *Cryst. Growth Des.*, 11:5441–5448, 2011.

[129] V. M. Kaganer and A. Y. Belov. Strain and x-ray diffraction from axial nanowire heterostructures. *Phys. Rev. B*, 85:125402, 2012.

[130] Machine Parameters PETRA III (Design Values). *http://photon-science.desy.de/facilities/petra_iii/machine/parameters/index_eng.html*, 2017-01-16.

[131] Unified Data Sheet, P06 - Micro and Nano-Probe Beamline. *http://photon-science.desy.de/facilities/petra_iii/beamlines/p06_hard_x_ray_micro_probe/unified_data_sheet_p06/index_eng.html*, 2017-01-04.

[132] A. Snigirev, V. Kohn, I. Snigireva, and B. Lengeler. A compound refractive lens for focusing high-energy X-rays. *Nature*, 384:49–51, 1996.

[133] B. Lai, W. B. Yun, D. Legnini, Y. Xiao, J. Chrzas, P. J. Viccaro, V. White, S. Bajikar, D. Denton, F. Cerrina, E. Di Fabrizio, M. Gentili, L. Grella, and M. Baciocchi. Hard x-ray phase zone plate fabricated by lithographic techniques. *Appl. Phys. Lett.*, 61:1877–1879, 1992.

[134] G. Schneider, T. Schliebe, and H. Aschoff. Cross–linked polymers for nanofabrication of high–resolution zone plates in nickel and germanium. *J. Vac. Sci. Technol. B Microelectron. Nanom. Struct. Process. Meas. Phenom.*, 13:2809–2812, 1995.

[135] E. Di Fabrizio, F. Romanato, M. Gentili, S. Cabrini, B. Kaulich, J. Susini, and R. Barrett. High-efficiency multilevel zone plates for keV X-rays. *Nature*, 401:895–898, 1999.

[136] P. Kirkpatrick and A. V. Baez. Formation of Optical Images by X-Rays. *J. Opt. Soc. Am.*, 38:766–774, 1948.

[137] Y. Suzuki and F. Uchida. Hard x–ray microprobe with total–reflection mirrors. *Rev. Sci. Instrum.*, 63:578–581, 1992.

[138] M. J. Moghimi, J. Fernandes, A. Kanhere, and H. Jiang. Micro-Fresnel-Zone-Plate Array on Flexible Substrate for Large Field-of-View and Focus Scanning. *Sci. Rep.*, 5:15861, 2015.

[139] C. G. Schroer, P. Boye, J. M. Feldkamp, J. Patommel, D. Samberg, A. Schropp, A. Schwab, S. Stephan, G. Falkenberg, G. Wellenreuther, and N. Reimers. Hard X-ray nanoprobe at beamline P06 at PETRA III. *Nucl. Instruments Methods Phys. Res. Sect. A Accel. Spectrometers, Detect. Assoc. Equip.*, 616:93–97, 2010.

[140] B. Lengeler, C. G. Schroer, J. Tümmler, B. Benner, M. Richwin, A. Snigirev, I. Snigireva, and M. Drakopoulos. Imaging by parabolic refractive lenses in the hard X-ray range. *J. Synchrotron Radiat.*, 6:1153–1167, 1999.

[141] C. G. Schroer, M. Kuhlmann, U. T. Hunger, T. F. Günzler, O. Kurapova, S. Feste, F. Frehse, B. Lengeler, M. Drakopoulos, A. Somogyi, A. S. Simionovici, A. Snigirev, I. Snigireva, C. Schug, and W. H. Schröder. Nanofocusing parabolic refractive x-ray lenses. *Appl. Phys. Lett.*, 82:1485, 2003.

[142] C. G. Schroer, O. Kurapova, J. Patommel, P. Boye, J. Feldkamp, B. Lengeler, M. Burghammer, C. Riekel, L. Vincze, A. van der Hart, and M. Küchler. Hard x-ray nanoprobe based on refractive x-ray lenses. *Appl. Phys. Lett.*, 87:124103, 2005.

[143] C. G. Schroer, H. Susanne, A. Goldschmidt, R. Hoppe, J. Patommel, D. Samberg, A. Schropp, F. Seiboth, S. Stephan, Schöder S., M. Burghammer, M. Denecke, G. Wellenreuther, and G. Falkenberg. Hard x-ray nano-beam characterization by ptychographic imaging. *Proc. SPIE*, 8141:814103–814110, 2011.

[144] I. Vartaniants and O. Yefanov. *Coherent X-ray Diffraction Imaging of Nanostructures*, pages 341–384. Pan Stanford, Singapore, 2015.

[145] S. Di Fonzo, W. Jark, S. Lagomarsino, C. Giannini, L. De Caro, A. Cedola, and M. Muller. Non-destructive determination of local strain with 100-nanometre spatial resolution. *Nature*, 403:638–640, 2000.

[146] M. Schmidbauer. *X-ray diffuse scattering from self-organized mesoscopic semiconductor structures*. Springer-Verlag Berlin Heidelberg New York, 2004.

[147] J. Miao, R. L. Sandberg, and C. Song. Coherent x-ray diffraction imaging. *IEEE J. Sel. Topics Quantum Electron.*, 18:399–410, 2012.

[148] R. Mokso, F. Marone, S. Irvine, M. Nyvlt, D. Schwyn, K. Mader, G. K. Taylor, H. G. Krapp, M. Skeren, and M. Stampanoni. Advantages of phase

retrieval for fast x-ray tomographic microscopy. *J. Phys. D. Appl. Phys.*, 46:494004, 2013.

[149] F. Zhang, B. Chen, G. R. Morrison, J. Vila-Comamala, M. Guizar-Sicairos, and I. Robinson. Phase retrieval by coherent modulation imaging. *Nat. Commun.*, 7:13367, 2016.

[150] F. C. Frank. On Miller–Bravais indices and four-dimensional vectors. *Acta Crystallogr.*, 18:862–866, 1965.

[151] T. Krause, M. Hanke, O. Brandt, and A. Trampert. Counterintuitive strain distribution in axial (In,Ga)N/GaN nanowires. *Appl. Phys. Lett.*, 108:32103, 2016.

[152] K. Shimada. First-Principles Determination of Piezoelectric Stress and Strain Constants of Wurtzite III-V Nitrides. *Jpn. J. Appl. Phys.*, 45:L358, 2006.

[153] O. Marquardt, L. Geelhaar, and O. Brandt. Electronic properties of axial $In_xGa_{1-x}N$ insertions in GaN nanowires. *J. Comp. Electron.*, 14:464–468, 2015.

[154] M. Wölz, S. Fernández-Garrido, C. Hauswald, O. Brandt, F. Limbach, L. Geelhaar, and H. Riechert. Indium incorporation in InGaN/GaN nanowire heterostructures investigated by line-of-sight quadrupole mass spectrometry. *Cryst. Growth Des.*, 12:5686–5692, 2012.

[155] G. Tourbot, C. Bougerol, F. Glas, L. F. Zagonel, Z. Mahfoud, S. Meuret, P. Gilet, M. Kociak, B. Gayral, and B. Daudin. Growth mechanism and properties of ingan insertions in gan nanowires. *Nanotechnology*, 23:135703, 2012.

[156] A. E. H. Love. *A Treatise on the Mathematical Theory of Elasticity*. Dover, New York, fourth edition, 1944.

[157] S. Timoshenko and J.N. Goodier. *Theory of Elasticity*. McGraw-Hill, New York, second edition, 1951.

[158] G. W. Housner and Jr. T. Vreeland. *The Analysis of Stress and Deformation*. McMillan, New York, 1966.

[159] J. G. Swadener and S. T. Picraux. Strain distributions and electronic property modifications in Si/Ge axial nanowire heterostructures. *J. Appl. Phys.*, 105:044310, 2009.

[160] C.-Y. Wen, M. C. Reuter, D. Su, E. A. Stach, and F. M. Ross. Strain and stability of ultrathin Ge layers in Si/Ge/Si axial heterojunction nanowires. *Nano Lett.*, 15:1654–9, 2015.

[161] C. M. Haapamaki and R. R. Lapierre. Mechanisms of molecular beam epitaxy growth in InAs/InP nanowire heterostructures. *Nanotechnology*, 22:335602, 2011.

[162] G. Zhang, K. Tateno, M. D. Birowosuto, M. Notomi, T. Sogawa, and H. Gotoh. Controlled 1.1-1.6 μm luminescence in gold-free multi-stacked InAs/InP heterostructure nanowires. *Nanotechnology*, 26:115704, 2015.

[163] P. Dłuzewski, E. Janik, S. Kret, W. Zaleszczyk, D. Tang, G. Karczewski, and T. Wojtowicz. TEM characterization of MBE grown CdTe/ZnTe axial nanowires. *J. Microsc.*, 237:337–340, 2010.

[164] O. Marquardt, T. Krause, V. Kaganer, J. Martín-Sánchez, M. Hanke, and O. Brandt. Influence of strain relaxation in axial $In_xGa_{1-x}N$/GaN nanowire heterostructures on their electronic properties. *Nanotechnology*, 28:215204, 2017.

[165] D. A. B. Miller, D. S. Chemla, T. C. Damen, A. C. Gossard, W. Wiegmann, T. H. Wood, and C. A. Burrus. Band-Edge Electroabsorption in Quantum Well Structures: The Quantum-Confined Stark Effect. *Phys. Rev. Lett.*, 53:2173–2176, 1984.

[166] R. Bardoux, A. Kaneta, M. Funato, Y. Kawakami, A. Kikuchi, and K. Kishino. Positive binding energy of a biexciton confined in a localization center formed in a single $In_xGa_{(1-x)}N$/GaN quantum disk. *Phys. Rev. B*, 79:155307, 2009.

[167] R. Armitage and K. Tsubaki. Multicolour luminescence from InGaN quantum wells grown over GaN nanowire arrays by molecular-beam epitaxy. *Nanotechnology*, 21:195202, 2010.

[168] H. P. T. Nguyen, S. Zhang, K. Cui, X. Han, S. Fathololoumi, M. Couillard, G. A. Botton, and Z. Mi. p-Type Modulation Doped InGaN/GaN Dot-in-a-Wire White-Light-Emitting Diodes Monolithically Grown on Si(111). *Nano Lett.*, 11:1919–1924, 2011.

[169] O. Marquardt, L. Geelhaar, and O. Brandt. Minimizing the impact of surface potentials in axial $In_xGa_{1-x}N$/GaN nanowire heterostructures by reducing their diameter. *J. Phys. D. Appl. Phys.*, 47:394007, 2014.

[170] Y.-T. Chen, W.-C. Tsai, W.-Y. Chen, C.-L. Hsiao, H.-C. Hsu, W.-H. Chang, T.-M. Hsu, K.-H. Chen, and L.-C. Chen. Growth of sparse arrays of narrow GaN nanorods hosting spectrally stable InGaN quantum disks. *Opt. Express*, 20:16166–16173, 2012.

[171] J. K. Zettler, P. Corfdir, C. Hauswald, E. Luna, U. Jahn, T. Flissikowski, E. Schmidt, C. Ronning, A. Trampert, L. Geelhaar, H. T. Grahn,

O. Brandt, and S. Fernández-Garrido. Observation of Dielectrically Confined Excitons in Ultrathin GaN Nanowires up to Room Temperature. *Nano Lett.*, 16:973–980, 2016.

[172] V. M. Kaganer, O. Marquardt, and O. Brandt. Piezoelectric potential in axial (In,Ga)N/GaN nanowire heterostructures. *Nanotechnology*, 27:165201, 2016.

[173] M. Winkelnkemper, A. Schliwa, and D. Bimberg. Interrelation of structural and electronic properties in $In_xGa_{1-x}N$/GaN quantum dots using an eight-band $k \cdot p$ model. *Phys. Rev. B*, 74:155322, 2006.

[174] S. Schulz, M. A. Caro, E. P. O'Reilly, and O. Marquardt. Symmetry-adapted calculations of strain and polarization fields in (111)-oriented zinc-blende quantum dots. *Phys. Rev. B*, 84:125312, 2011.

[175] O. Marquardt, C. Hauswald, M. Wölz, L. Geelhaar, and O. Brandt. Luminous Efficiency of Axial $In_xGa_{1-x}N$/GaN Nanowire Heterostructures: Interplay of Polarization and Surface Potentials. *Nano Lett.*, 13:3298–3304, 2013.

[176] C. Böcklin, R. G. Veprek, S. Steiger, and B. Witzigmann. Computational study of an InGaN/GaN nanocolumn light-emitting diode. *Phys. Rev. B*, 81:155306, 2010.

[177] M. Mandl, X. Wang, T. Schimpke, C. Kölper, M. Binder, J. Ledig, A. Waag, X. Kong, A. Trampert, F. Bertram, J. Christen, F. Barbagini, E. Calleja, and M. Strassburg. Group III nitride core–shell nano- and microrods for optoelectronic applications. *Phys. status solidi – Rapid Res. Lett.*, 7:800–814, 2013.

[178] X. Wang, U. Jahn, M. Mandl, T. Schimpke, J. Hartmann, J. Ledig, M. Straßburg, H.-H. Wehmann, and A. Waag. Growth and characterization of mixed polar GaN columns and core–shell LEDs. *Phys. Status Solidi*, 212:727–731, 2015.

[179] R. Koester, D. Sager, W.-A. Quitsch, O. Pfingsten, A. Poloczek, S. Blumenthal, G. Keller, W. Prost, G. Bacher, and F.-J. Tegude. High-Speed GaN/GaInN Nanowire Array Light-Emitting Diode on Silicon(111). *Nano Lett.*, 15:2318–2323, 2015.

[180] T. Krause, M. Hanke, Z. Cheng, M. Niehle, A. Trampert, M. Rosenthal, M. Burghammer, J. Ledig, J. Hartmann, H. Zhou, H.-H. Wehmann, and A. Waag. Nanofocus x-ray diffraction and cathodoluminescence investigations into individual core-shell (In,Ga)N/GaN rod light-emitting diodes. *Nanotechnology*, 27:325707, 2016.

[181] X. Wang, S. Li, M. S. Mohajerani, J. Ledig, H.-H. Wehmann, M. Mandl, M. Strassburg, U. Steegmüller, U. Jahn, J. Lähnemann, H. Riechert, I. Griffiths, D. Cherns, and A. Waag. Continuous-Flow MOVPE of Ga-Polar GaN Column Arrays and Core–Shell LED Structures. *Cryst. Growth Des.*, 13:3475–3480, 2013.

[182] M. Niehle and A. Trampert. Electron tomography on nanopores embedded in epitaxial GaSb thin films. *Micron*, 73:54–62, 2015.

[183] EIGER X detector series technical specifications. *https://www.dectris.com/EIGER_X_Specifications.html*, 2017-01-13.

[184] Q. Li and G. T. Wang. Spatial Distribution of Defect Luminescence in GaN Nanowires. *Nano Lett.*, 10:1554–1558, 2010.

[185] J. Kioseoglou, T. Pavloudis, T. Kehagias, P. Komninou, T. Karakostas, C. D. Latham, M. J. Rayson, P. R. Briddon, and M. Eickhoff. Structural and electronic properties of GaN nanowires with embedded $In_xGa_{1-x}N$ nanodisks. *J. Appl. Phys.*, 118:034301, 2015.

[186] T. Krause, M. Hanke, L. Nicolai, Z. Cheng, M. Niehle, A. Trampert, M. Kahnt, G. Falkenberg, C. G. Schroer, J. Hartmann, H. Zhou, H.-H. Wehmann, and A. Waag. Structure and Composition of Isolated Core-Shell (In,Ga)N/GaN Rods Based on Nanofocus X-Ray Diffraction and Scanning Transmission Electron Microscopy. *Phys. Rev. Applied*, 7:24033, 2017.

[187] C. Tessarek, M. Heilmann, E. Butzen, A. Haab, H. Hardtdegen, C. Dieker, E. Spiecker, and S. Christiansen. The Role of Si during the Growth of GaN Micro- and Nanorods. *Cryst. Growth Des.*, 14:1486–1492, 2014.

[188] J. Hartmann, X. Wang, H. Schuhmann, W. Dziony, L. Caccamo, J. Ledig, M. S. Mohajerani, T. Schimpke, M. Bähr, G. Lilienkamp, W. Daum, M. Seibt, M. Straßburg, H.-H. Wehmann, and A. Waag. Growth mechanisms of GaN microrods for 3D core–shell LEDs: The influence of silane flow. *Phys. Status Solidi*, 212:2830–2836, 2015.

[189] Pilatus 300K. *https://www.dectris.com/tl_files/root/news/20111122/ Pilatus_300K_20Hz_web_a4.pdf*, 2017-02-01.

[190] M. Hanke, M. Schmidbauer, and R. Köhler. Lateral correlation of SiGe Stranski-Krastanow islands on silicon as probed by high resolution x-ray diffraction. *J. Appl. Phys.*, 96:1959, 2004.

[191] J. Ledig, X. Wang, S. Fündling, H. Schuhmann, M. Seibt, U. Jahn, H.-H. Wehmann, and A. Waag. Characterization of the internal properties of InGaN/GaN core-shell LEDs. *Phys. Status Solidi*, 213:11–18, 2016.

[192] J. Hartmann, F. Steib, H. Zhou, J. Ledig, S. Fündling, F. Albrecht, T. Schimpke, A. Avramescu, T. Varghese, H.-H. Wehmann, M. Straßburg, H.-J. Lugauer, and A. Waag. High Aspect Ratio GaN Fin Microstructures with Nonpolar Sidewalls by Continuous Mode Metalorganic Vapor Phase Epitaxy. *Cryst. Growth Des.*, 16:1458–1462, 2016.

Eidesstattliche Erklärung

Ich erkläre hiermit an Eides statt, dass ich die Dissertation selbständig und nur unter Verwendung der von mir gemäß §7 Abs. 3 der Promotionsordnung der Mathematisch-Naturwissenschaftlichen Fakultät I, veröffentlicht im Amtlichen Mitteilungsblatt der Humboldt-Universität zu Berlin Nr. 126/2014 am 18.11.2014, angegebenen Hilfsmittel angefertigt habe.

Berlin,